Non-Invasive Quantitative Imaging Informs Early Assessment of Cancer Therapeutic Response

by

Benjamin A. Hoff

A dissertation submitted in partial fulfillment
of the requirements for the degree of
Doctor of Philosophy
(Biomedical Engineering)
in the University of Michigan
2013

Doctoral Committee:
Assistant Professor Craig J. Galbán, Chair
Professor Thomas L. Chenevert
Assistant Professor Kenneth M. Kozloff
Professor Douglas C. Noll
Professor Brian D. Ross

Acknowledgements

I would first like to thank Drs. Brian Ross and Craig Galbán for their financial support and general encouragement throughout my graduate career at the University of Michigan. Without this, I would likely not have progressed through the Ph.D. program. Working in this lab even as early as my freshman year under Drs. Brian Ross and Bradford Moffat solidified my interest in this field in addition to providing employment in their group which helped me pay my way through undergrad. I have been truly lucky to have access to the many imaging systems in Dr. Ross's lab, which is equipped beyond the means of most peer laboratories.

Since Dr. Galbán joined the lab, he has been a driving force in motivating me toward this goal. Without his energy and enthusiasm none of this would have been possible. His style of informal interactions to facilitate discussions helped to expedite my learning process, and was a great help in determining my research goals. Frequent discussions about the experimental process and background enhanced my understanding of the experimental strategy, and his proof-reading has greatly helped my writing skills.

Dr. Alnawaz Rehemtulla and those in his lab have been driving influences for learning the biology of cancer and strategies for bioluminescent molecular imaging. He has been of great help in understanding cell markers and drug targets as well as the use of advanced imaging techniques, such as bioluminescence (BLI), for understanding how cell signaling works.

I would also like to acknowledge Dr. Thomas Chenevert for his valuable discussions about MRI principles. He has been a very patient teacher and has helped me to understand much about image artifacts, physics, pulse sequencing, and trouble-shooting related to MRI. Also, through revisions of his programs, I was able to enhance my knowledge of programming and MRI reconstruction.

Also in my more recent projects, I have been able to delve more into fluorescence and x-ray CT imaging. Through discussions with Dr. Kenneth Kozloff, as well as review of his

publications, I have learned a lot about the analysis and experimental strategy of bone imaging. His help with my osteoporosis and bone metastasis projects proved invaluable. I would also like to thank Kathy Sweet for performing the surgical procedure for this project.

I have also had many discussions with Dr. Charles Meyer, who provided critical support for all image co-registrations, which is the linchpin of PRM analysis. His help in understanding the subtleties of spatial transformation and the balance between speed and accuracy in the result have greatly aided the progress of much of my work.

Although my interaction with Dr. Doug Noll has been relatively limited, I feel that much of my understanding of image formation from MRI, CT, and ultrasound can be attributed to him. Early in my graduate career I took his class on medical imaging, which greatly increased my understanding of the theory behind all of the imaging I had been doing up until then.

Beyond the science of my research, others within the CMI group have provided assistance during my graduate studies and I would like to thank them by name. Tania Cunningham, our administrative assistant, with her enthusiasm and bright character has provided invaluable assistance with administrative issues. Amanda Fair, the CMI Imaging Core Facility Manager, provided assistance with my animal protocols and procurement of supplies for my projects. Finally, Gary Laderach, CMI IT Specialist, for his technical support is greatly appreciated as his help in all things computers was always in high demand.

I must also thank my student helpers that I have worked with during my studies. It is my firm belief that the ability to convey an idea in an intelligible fashion is critically important for a doctoral candidate. The opportunity to train and work with undergraduate students within the CMI provided me this exposure, which also reinforces my own understanding of my research. Although it can take some time to teach what they need to know, it almost always is worth the effort.

Finally, I would like to thank my family for their continuing support. They have always pushed me to excel and to find something I truly love doing. Last, but definitely not least, I would like to thank my wife, Kaarin. Her unflinching support through these last few demanding years of graduate school have kept me going. Through our many discussions about my projects I have learned to be a better communicator of my research.

Ann Arbor

Aug 2013

Table of Contents

List of Tables

List of Figures

List of Acronyms

ADC – Apparent Diffusion Coefficient

AKT – Protein Kinase B

AUC – Area Under the Curve

BCNU – 1,3-bis(2-chloroethyl)-1-nitrosourea

BLI – Bioluminescent Imaging

BMC – Bone Mineral Content

BMD – Bone Mineral Density

BSA – Bovine Serum Albumin

BV – Bone Volume

CT – Computed Tomography (specifically x-ray)

DCE – Dynamic Contrast-Enhanced

DDC – Distributed Diffusion Coefficient (for Stretched Exponential diffusion model)

DMSO – Dimethyl Sulfoxide

DSC – Dynamic Susceptibility-Weighted

DTI – Diffusion Tensor Imaging

DWI – Diffusion-weighted Imaging

DXA – Dual-energy X-ray Absorptiometry

EES – Extracellular Extravascular Space

EGFR – Epidermal Growth Factor Receptor

ELISA – Enzyme-Linked Immunosorbent Assay

ETL – Echo Train Length (for fast spin-echo MRI)

Fc – Factor c

fDM – functional Diffusion Map

FEA – Finite Element Analysis

FLI – Fluorescence Imaging

FOV – Field of View

Gd-DTPA – Gadopentetic Acid

GoF – Goodness of Fit

H&E – Hematoxylin & Eosin

HRP – Anti-Horseradish Peroxidase

HU – Hounsfield Unit

IgG – Immunoglobulin-G

IHC – Immuno-Histo-Chemistry

MIP – Maximum Intensity Projection

MRI – Magnetic Resonance Imaging

NRMSD – Normalized Root Mean Squared Deviation

OVX – Ovariectomy

PBS – Phosphate-Buffered Saline

PRM – Parametric Response Map

PSA – Prostate-Specific Antigen

RANK(-L) – Receptor Activator of Nuclear factor Kappa-B (ligand)

ROI – Region of Interest

R_{TP} – Ratio of Two-Point diffusion coefficients

SC – Sensitivity Coefficient

SCID – Severe Combined Immunodeficient

SEM – Standard Error of the Mean

SMI – Structural Model Index

SNR – Signal-to-Noise Ratio

SRE – Skeletal-Related Event

SSM – Shutter-Speed model (DCE-MRI)

Tb.Sp – Trabecular Spacing

Tb.Th – Trabecular Thickness

TE – Echo Time (for MRI)

TGFβ – Transforming Growth Factor β

TK – Tofts-Kermode model (DCE-MRI)

TMB –Tetramethylbenzidine

TR – Repetition Time (for MRI)

TV – Total Volume

VEGF – Vascular Endothelial Growth Factor

VOI – Volume of Interest

vWf – von Willebrand Factor VIII (IHC stain for vascular endothelium)

ZA – Zoledronic Acid

List of Symbols

C_p – blood plasma concentration

C_t – tissue concentration

f_W – tissue water volume fraction (SSM)

k_{ep} – flux rate constant between the extravascular extracellular space and plasma

K^{Trans} – volume transfer coefficient (blood to EES) for DCE-MRI analysis

L – first-order transfer rate constant (= K^{Trans}) (SSM)

p_0 – extracellular volume fraction (= v_e/f_W) (SSM)

R_1 – spin-lattice relaxation rate constant ($1/T_1$)

r_1 – T_1 contrast agent relaxivity

T_1 – spin-lattice relaxation time constant

T_2 – spin-spin relaxation time constant

v_e – fractional volume of EES

v_p – blood plasma volume fraction

α – diffusion anomalous exponent (Stretched-exponential diffusion model)

τ_i – mean intracellular water molecule lifetime (SSM)

Abstract

EVALUATION OF NON-INVASIVE IMAGING METHODS FOR QUANTIFICATION OF TREATMENT RESPONSE

by

Benjamin A. Hoff

Chair: Craig J. Galbán

Therapeutic response assessment of cancer has long been facilitated by non-invasive imaging methods such as magnetic resonance imaging (MRI) and x-ray computed tomography (CT) in the clinic. Standards of patient care are designed around the most common cases, which may not always be efficacious. However, through evidence-based medicine there has begun a shift toward more individualized care. Standard clinical practice for cancer response assessment utilizes only volumetric change, measured prior and following the completion of therapy, providing no opportunity to adjust the treatment. In addition, novel targeted therapies, which may not result in a substantial decrease in tumor volume, are becoming more prevalent in the treatment of tumors. There is a clear need for non-invasive biomarkers that provide near real-time information on the anatomical and physiological makeup of the tumor post-treatment initiation. Tools for assessing early treatment response may allow physicians to dynamically optimize treatments individually, enhancing patient prognoses and avoiding unnecessary patient morbidity. In the following studies, I have evaluated various non-invasive imaging tools for early detection of treatment response in rodent models of disease. Tissue apparent diffusion coefficients (ADC) are known to correlate well with cellular status in cancer, and have shown promise in the detection of early tumor treatment response. Several different numerical models of higher-order diffusion signal attenuation were evaluated to determine their sensitivity to treatment response compared to the standard diffusion model. Dynamic contrast-enhanced (DCE-) MRI has shown sensitivity to vascular changes in cancer and was evaluated as an imaging biomarker of treatment response using a novel vascular-targeted therapy. Quantitative indices generated from DCE-MRI data were compared to diffusion (ADC) and volumetric MRI readouts for response assessment. The utility of imaging readouts from concurrent MRI, CT, bioluminescence, and fluorescence imaging was also evaluated in a model of bone metastasis. Further, a new voxel-based analytical technique, the parametric response map (PRM), was applied to CT images of metastatic bone disease and osteoporosis to evaluate bone response to treatment and hormone deprivation, respectively. Use of these tools may help improve the clinical effectiveness of cancer patient therapy as well as drug development and testing in preclinical models.

Chapter 0: **Introduction**

Diagnosis and assessment of therapeutic response in cancer has long been facilitated by non-invasive imaging methods such as magnetic resonance imaging (MRI), x-ray radiographs, positron emission tomography (PET), single photon emission computed tomography (SPECT) and x-ray computed tomography (CT) in the clinic and more recently optical imaging (fluorescence and bioluminescence) for pre-clinical models. On the subject of tumor biology there is still much that is not understood, for example some patients given a therapy may exhibit a positive outcome while others with the same therapy and clinical histopathological characteristics may not. Because of this, evaluation of the effectiveness of a therapy is valuable in determining a patient's treatment strategy and prognosis. Traditional evaluation of cancer treatment efficacy has relied heavily on volumetric monitoring of tumor burden, with decreases indicating a successful response. These changes, however, may not be detectable until well after the treatment regime has been completed, precluding adjustment of the treatment strategy based on its efficacy. Development of tools for assessing early treatment response may allow physicians to dynamically optimize treatments on an individual level, enhancing patient prognoses and avoiding unnecessary patient morbidity.

Diffusion-MRI is an MRI sequence capable of quantifying the molecular motion of protons primarily in water using bipolar motion-sensitive gradients. The magnitude of diffusion weighting is measured in b-values, which are a function of gradient strength, duration and spacing between gradients. Diffusion weighting can be applied directionally, allowing some assessment of the tissue structures as in diffusion tensor imaging (DTI), or isotropically, resulting in a general assessment of tissue water diffusion. In the simplest case only two diffusion-weighted images at a low and nominal b-value (~0 and ~1000 s/mm^2, respectively) are required to generate the quantitative metric, the apparent diffusion coefficient (ADC) map, assuming mono-exponential decay in the MRI signal with increasing b-value. ADC has been

shown to be indicative of cellular status in cancer treatment [1-12]. Increases in ADC have correlated well with tumor cell death caused by cytotoxic therapies and are well-documented for nominal diffusion weighting. Recent studies, however, have shown that at high diffusion weighting (b-value) the signal attenuation curve deviates from a true mono-exponential behavior [9, 13-21]. Although no single theory has yet been embraced, the most popular models either use the sum of two diffusion populations (proposed as intra- and extra-cellular water) or a spectrum of diffusion rates attributed to the continuum of water hydration shells surrounding biological structures. Changes in these non-mono-exponential metrics may prove sensitive for detecting treatment response.

Dynamic contrast-enhanced- (DCE-) MRI is a technique using small-molecule paramagnetic contrast-enhancing tracers injected intravenously to extract tissue vascular properties from time-course T_1-weighted MR images. Contrast enhancement of the T_1-weighted signal is proportional to the voxel concentration of contrast agent, allowing the extraction of pharmacokinetic tissue properties through modeling. Growing interest has been apparent in targeted cancer therapies, one focus of which is anti-vascular drugs such as Bevacizumab and Aflibercept. These targeted agents inhibit cellular signaling and resulting angiogenesis, the growth and recruitment of blood vessels, within the tumor. DCE-MRI has been shown to detect a reduction in vascular leakiness and blood volume within a treated tumor. In the following, both DCE- and DW-MRI were used to evaluate treatment response in a 9L rat gliosarcoma model treated with the new therapeutic agent, Aflibercept. A few different widely-used analytical models were also compared on the same data to assess variation of response sensitivity in these models.

For the development and evaluation of new cancer pharmaceuticals, non-invasive imaging biomarkers have proven very useful in reducing total necessary animal populations as well as expediting the measurement of a therapeutic response. Quantification of treatment response in bone metastases has proven to be an elusive task, with currently no clinically-accepted criteria. Recent studies have shown a critical link between metastatic cancer and its micro-environment, coined the “seed and soil” [22]. Through interaction with bone, certain cancer phenotypes are spurred to grow and proliferate, resulting in a vicious cycle of bone remodeling and tumor growth. With the wide variety of available imaging modalities, a great deal of physiological information can now be obtained from a single subject longitudinally over

the course of the study. With the combination of imaging modalities, researchers are now able to quantify multiple treatment responses at essentially the same time as well as longitudinally, in this case both bone and tumor response. In the following, an animal model of boney metastasis is presented, and treatment response is evaluated by DW-MRI, quantitative CT, bioluminescence (BLI), and fluorescence (FLI) imaging after treatment with the bisphosphonate, zoledronic acid, or the cytotoxic agent, docetaxel. These two therapies serve to highlight the two extreme treatment cases: anti-tumor-environment or anti-tumor, respectively, and are both clinically relevant therapies. Using multiple readouts, a more comprehensive perspective for new drug evaluation and efficacy screening can be achieved.

Traditionally, quantitative cancer imaging has been evaluated using whole-tumor statistics such as the mean or histogram-based analyses. A new voxel-wise approach to detecting treatment response, the function diffusion map (fDM), has successfully been applied to DW-MRI, resulting in increased sensitivity to localized diffusion changes over mean volume statistics [23-28]. This technique uses spatially aligned serial images to compare diffusion images both spatially and temporally. This same technique, now termed the parametric response map (PRM), has already been expanded to other images, including DCE- and dynamic susceptibility contrast (DSC-) MRI. In the following, this PRM analysis will be applied to bone CT images (in Hounsfield units, HU) to evaluate localized bone changes both in animal models and clinical metastatic cancer patients. Sensitivity of PRM_{HU} to bone changes was validated through a well-establish ovariectomy-induced osteoporosis model in rats, and further characterized in both osteolytic and osteoblastic models of bone metastasis in mice.

In conclusion, there exists a great variety of quantitative imaging options for the assessment of cancer treatment response, particularly in pre-clinical imaging where tissue depths are not enough to inhibit optical imaging modalities. Through early detection of treatment response clinical patient treatments may be individualized, allowing the option to adjust treatments virtually “on the fly”. In addition, through the use of a multimodal quantitative imaging approach, tailored to a focused treatment or effect, a more comprehensive and efficient evaluation of mixed treatment effects can be possible. Even for a single imaging modality, for example DCE-MRI, it is important to understand the accuracy and limitations of the model to be used in order to extract valid conclusions from the results. In the following chapters various analytical models for multi-exponential diffusion MRI and DCE-MRI are evaluated for both

sensitivity to physiological or model parameter change and sensitivity to noise in the images. The use of a multi-modality imaging strategy is also evaluated, using MRI, x-ray CT, bioluminescence, and fluorescence imaging, for a more comprehensive evaluation of tumor/stroma treatment response using a limited study population. Finally, a new method for evaluating spatially-localized changes in 3D images is evaluated on CT images of the bone. This method may see its greatest use for evaluation of bone metastases, which currently have no official criteria for assessing treatment response in the clinic. This manuscript provides an evaluation of several methods for quantifying physiological changes *in vivo*.

0.1: References

[1] Byun WM, Shin SO, Chang Y, Lee SJ, Finsterbusch J, Frahm J. Diffusion-weighted MR imaging of metastatic disease of the spine: assessment of response to therapy. AJNR Am J Neuroradiol 2002;23: 906-12.

[2] Chenevert TL, McKeever PE, Ross BD. Monitoring early response of experimental brain tumors to therapy using diffusion magnetic resonance imaging. Clin Cancer Res 1997;3: 1457-66.

[3] Chenevert TL, Meyer CR, Moffat BA, Rehemtulla A, Mukherji SK, Gebarski SS, Quint DJ, Robertson PL, Lawrence TS, Junck L, Taylor JM, Johnson TD, Dong Q, Muraszko KM, Brunberg JA, Ross BD. Diffusion MRI: a new strategy for assessment of cancer therapeutic efficacy. Mol Imaging 2002;1: 336-43.

[4] Chenevert TL, Stegman LD, Taylor JM, Robertson PL, Greenberg HS, Rehemtulla A, Ross BD. Diffusion magnetic resonance imaging: an early surrogate marker of therapeutic efficacy in brain tumors. J Natl Cancer Inst 2000;92: 2029-36.

[5] Chenevert TL, Sundgren PC, Ross BD. Diffusion imaging: insight to cell status and cytoarchitecture. Neuroimaging Clin N Am 2006;16: 619-32, viii-ix.

[6] Galbán CJ, Bhojani MS, Lee KC, Meyer CR, Van Dort ME, Kuszpit KK, Koeppe RA, Ranga R, Moffat BA, Johnson TD, Chenevert TL, Rehemtulla A, Ross BD. Evaluation of treatment-associated inflammatory response on diffusion-weighted magnetic resonance imaging and 2-[18F]-fluoro-2-deoxy-D-glucose-positron emission tomography imaging biomarkers. Clin Cancer Res 2010;16: 1542-52.

[7] Galbán S, Brisset JC, Rehemtulla A, Chenevert TL, Ross BD, Galbán CJ. Diffusion-weighted MRI for assessment of early cancer treatment response. Curr Pharm Biotechnol 2010;11: 701-8.

[8] Galons JP, Altbach MI, Paine-Murrieta GD, Taylor CW, Gillies RJ. Early increases in breast tumor xenograft water mobility in response to paclitaxel therapy detected by non-invasive diffusion magnetic resonance imaging. Neoplasia 1999;1: 113-7.

[9] Kwee TC, Galban CJ, Tsien C, Junck L, Sundgren PC, Ivancevic MK, Johnson TD, Meyer CR, Rehemtulla A, Ross BD, Chenevert TL. Comparison of apparent diffusion coefficients and distributed diffusion coefficients in high-grade gliomas. J Magn Reson Imaging 2010;31: 531-7.

[10] Kwee TC, Galban CJ, Tsien C, Junck L, Sundgren PC, Ivancevic MK, Johnson TD, Meyer CR, Rehemtulla A, Ross BD, Chenevert TL. Intravoxel water diffusion heterogeneity imaging of human high-grade gliomas. NMR Biomed 2010;23: 179-87.
[11] Ross BD, Moffat BA, Lawrence TS, Mukherji SK, Gebarski SS, Quint DJ, Johnson TD, Junck L, Robertson PL, Muraszko KM, Dong Q, Meyer CR, Bland PH, McConville P, Geng H, Rehemtulla A, Chenevert TL. Evaluation of cancer therapy using diffusion magnetic resonance imaging. Mol Cancer Ther 2003;2: 581-7.
[12] Ross BD, Zhao YJ, Neal ER, Stegman LD, Ercolani M, Ben-Yoseph O, Chenevert TL. Contributions of cell kill and posttreatment tumor growth rates to the repopulation of intracerebral 9L tumors after chemotherapy: an MRI study. Proc Natl Acad Sci U S A 1998;95: 7012-7.
[13] Bennett KM, Schmainda KM, Bennett RT, Rowe DB, Lu H, Hyde JS. Characterization of continuously distributed cortical water diffusion rates with a stretched-exponential model. Magn Reson Med 2003;50: 727-34.
[14] Clark CA, Le Bihan D. Water diffusion compartmentation and anisotropy at high b values in the human brain. Magn Reson Med 2000;44: 852-9.
[15] Cohen Y, Assaf Y. High b-value q-space analyzed diffusion-weighted MRS and MRI in neuronal tissues - a technical review. NMR Biomed 2002;15: 516-42.
[16] Hall MG, Barrick TR. From diffusion-weighted MRI to anomalous diffusion imaging. Magn Reson Med 2008;59: 447-55.
[17] Kiselev VG, Il'yasov KA. Is the "biexponential diffusion" biexponential? Magn Reson Med 2007;57: 464-9.
[18] Le Bihan D. The 'wet mind': water and functional neuroimaging. Phys Med Biol 2007;52: R57-90.
[19] Niendorf T, Dijkhuizen RM, Norris DG, van Lookeren Campagne M, Nicolay K. Biexponential diffusion attenuation in various states of brain tissue: implications for diffusion-weighted imaging. Magn Reson Med 1996;36: 847-57.
[20] Roth Y, Tichler T, Kostenich G, Ruiz-Cabello J, Maier SE, Cohen JS, Orenstein A, Mardor Y. High-b-value diffusion-weighted MR imaging for pretreatment prediction and early monitoring of tumor response to therapy in mice. Radiology 2004;232: 685-92.
[21] Schwarcz A, Bogner P, Meric P, Correze JL, Berente Z, Pal J, Gallyas F, Doczi T, Gillet B, Beloeil JC. The existence of biexponential signal decay in magnetic resonance diffusion-weighted imaging appears to be independent of compartmentalization. Magn Reson Med 2004;51: 278-85.
[22] Paget S. The distribution of secondary growths in cancer of the breast. 1889. Cancer Metastasis Rev 1989;8: 98-101.
[23] Galban CJ, Mukherji SK, Chenevert TL, Meyer CR, Hamstra DA, Bland PH, Johnson TD, Moffat BA, Rehemtulla A, Eisbruch A, Ross BD. A feasibility study of parametric response map analysis of diffusion-weighted magnetic resonance imaging scans of head and neck cancer patients for providing early detection of therapeutic efficacy. Transl Oncol 2009;2: 184-90.
[24] Lee KC, Bradley DA, Hussain M, Meyer CR, Chenevert TL, Jacobson JA, Johnson TD, Galban CJ, Rehemtulla A, Pienta KJ, Ross BD. A feasibility study evaluating the functional diffusion map as a predictive imaging biomarker for detection of treatment response in a patient with metastatic prostate cancer to the bone. Neoplasia 2007;9: 1003-11.

[25] Lee KC, Moffat BA, Schott AF, Layman R, Ellingworth S, Juliar R, Khan AP, Helvie M, Meyer CR, Chenevert TL, Rehemtulla A, Ross BD. Prospective early response imaging biomarker for neoadjuvant breast cancer chemotherapy. Clin Cancer Res 2007;13: 443-50.
[26] Lee KC, Sud S, Meyer CR, Moffat BA, Chenevert TL, Rehemtulla A, Pienta KJ, Ross BD. An imaging biomarker of early treatment response in prostate cancer that has metastasized to the bone. Cancer Res 2007;67: 3524-8.
[27] Moffat BA, Chenevert TL, Lawrence TS, Meyer CR, Johnson TD, Dong Q, Tsien C, Mukherji S, Quint DJ, Gebarski SS, Robertson PL, Junck LR, Rehemtulla A, Ross BD. Functional diffusion map: a noninvasive MRI biomarker for early stratification of clinical brain tumor response. Proc Natl Acad Sci U S A 2005;102: 5524-9.
[28] Moffat BA, Chenevert TL, Meyer CR, McKeever PE, Hall DE, Hoff BA, Johnson TD, Rehemtulla A, Ross BD. The functional diffusion map: an imaging biomarker for the early prediction of cancer treatment outcome. Neoplasia 2006;8: 259-67.

Chapter 1: **Non-Mono-exponential Diffusion**

1.1: Chemotherapeutic Treatment Response

Included with permission from John Wiley and Sons:

Hoff BA, Chenevert TL, Bhojani MS, Kwee TC, Rehemtulla A, Le Bihan D, Ross BD, Galbán CJ. Assessment of multiexponential diffusion features as MRI cancer therapy response metrics. Magn Reson Med. 2010 Nov;64(5):1499-509.

1.1.1: Introduction

Diffusion-weighted magnetic resonance imaging (DWI) shows promise as an imaging biomarker for treatment response in glioma patients [1-9] as well as in a variety of other clinical tumor types [10-16]. Routine in almost all preclinical and clinical scanners, diffusion maps can be generated from a minimum of two images acquired at low (b-value ~ 100 sec/mm^2) and high (b-value ~ 1000 sec/mm^2) diffusion weightings. Assuming mono-exponential signal attenuation with b-value, the apparent diffusion coefficient (ADC) can be calculated analytically. The application of diffusion MRI for the detection of early tumor treatment response was first reported using a rodent glioma model using diffusion weightings at nominal b-values (≤ 1000 sec/mm^2) [17]. This initial report has been verified and expanded by ensuing publications using different tumor models and therapeutic agents [1, 18, 19], supporting the use of diffusion MRI as a sensitive imaging biomarker capable of detecting early cellular changes in treated tumors which precede macroscopic volumetric response.

The efficacy of this technique lies in its sensitivity to the molecular motion of water, which is affected by cellular, subcellular, and macromolecular elements that impede otherwise free diffusion of water. Thus, therapeutic changes within the tumor at the cellular level can be monitored by serial diffusion measurements [20-23]. Through thermal random motion, water molecules sample the surrounding microarchitecture within tissues at length scales (few microns) much smaller than typical MRI voxel resolution (~millimeter). The theoretical basis for diffusion

analysis is that cell membranes and other structures hinder the diffusion of molecules [20, 24]. The magnitude of diffusion-driven displacement is altered by tortuosity and hindering effects and can therefore be used to infer their presence and density. Studies have revealed that in biological systems water proton signal attenuation due to diffusion weighting does not follow mono-exponential decay, and the deviation from mono-exponential behavior is best observed at relatively high b-values (≥ 3000 sec/mm^2). A more accurate description of signal attenuation with b-value over this wide b-value range requires more complex biophysical models [25-28].

An early interpretation of multiexponential diffusion patterns was that water moves within two or more compartments representing pools of "fast" (extracellular) and "slow" (intracellular) diffusion components in the signal. At low b-values the "fast" diffusion pool dominates signal attenuation, whereas at high b-values the "slow" diffusion pool dominates leading to a biexponential form for signal decay. Biexponential signal attenuation in DWI has been studied extensively in a variety of biological systems, and the physical mechanisms that govern nonmonoexponential decay continue to be an area of debate. An alternative formalism for the nonmonoexponential decay incorporates the underlying complexity in the diffusion medium as a continuous distribution of diffusion coefficients arising from a multiplicity of pools. Termed the "stretched-exponential" formalism, Bennett et al. [29] provided an analytical representation of the signal attenuation as a function of the probability density with a particular diffusion coefficient. Although this formalism can be used to infer the intravoxel diffusion heterogeneity within a biological system, it does not lend itself to straightforward association between biophysical compartments and signal decay. Although the "stretched-exponential" formalism has not been evaluated for its sensitivity to treatment response in tumors, this method has shown promise for characterizing tumors in brain cancer patients [30, 31].

Research investigating the sensitivity of high b-value DWI for treatment assessment has shown promising results [6, 32]. Mardor et al. have demonstrated in patients with malignant brain lesions that the ratio of the diffusion coefficient from the ''fast'' pool and the "slow" pool signal fraction is highly sensitive to radiation-induced changes in the tumor. This parameter not only demonstrated a significant change from baseline as early as 1 week post-treatment initiation but was capable of predicting clinical outcome in all of the studied patients [6]. In contrast, conventional mono-exponential ADC (in their study, low and high b-values were 120 and 1200

sec/mm^2, respectively) was found to be predictive of outcome in only half of the patient population studied. Sensitivity of high b-value DWI to treatment was also observed in a colon cancer mouse model [32]. These authors used the area under the normalized nonmonoexponential diffusion curve to quantify the diffusion characteristics of the tissue. This diffusion index was found to provide early prognostic information on animal responsiveness to treatment.

In this study, three nonmonoexponential diffusion formalisms applied over an extended range of b-values (120–4000 sec/mm^2) were tested against the conventional two-point ADC measurement to determine their sensitivity to therapy-induced changes of tissue using a rodent brain tumor model. Results showed similar time response curves for all diffusion indices following treatment. Although the highest fractional change following treatment was observed using the biexponential formalism, these results were not significantly different from those observed using the conventional two-point ADC calculation.

1.1.2: Methods

Animal Tumor Models

9L gliosarcoma cells were obtained from the Brain Tumor Research Center at the University of California in San Francisco. The cells were grown as monolayers in 10 cm^2 sterile plastic flasks in DMEM with 10% fetal bovine serum, 100 IU/mL penicillin, 100 mg/mL streptomycin, and 2 mM L-glutamine in an incubator held at 37°C and 95%/5% air/CO_2 atmosphere. Before implantation, cells were harvested by trypsinization, counted, and re-suspended in serum-free medium for injection.

Tumor implantation was performed on Male Fischer 344 rats (Harlan Sprague-Dawley, Indianapolis, IN), weighing ~125–150 g, as previously described [33]. Briefly, animals were anesthetized with a ketamine/xylazine mixture (87/13 mg/kg) administered intraperitoneal. A small incision was then made over the right hemisphere of the cranium. A 1 mm diameter burr hole was drilled through the skull using a high-speed surgical drill, and a 5 mL suspension containing 1 x 10^5 9L cells was injected through the burr hole to a depth of 3 mm. After injection of the cells, the burr hole was filled with bone wax to prevent extra-cranial extension of the tumor, and the surgical area was cleaned using 70% ethanol. Vetbond (3M, St. Paul, MN) was used to close the incision until healed.

Chemotherapy

Once the tumors reached 40–80 mm^3 as quantified using T_2-weighted MRI, pretreatment diffusion-weighted (DW) images (details below) were acquired for all animals. At the time of treatment, 1,3-bis(2-chloroethyl)-1-nitrosourea (BCNU) (LKT Laboratories, St. Paul, MN) was freshly prepared and formulated to a final concentration of 5 mg/mL BCNU in 10% ethanol. Subsequent to their pretreatment DWI scan, animals either received a single bolus intraperitoneal injection of BCNU (9.98 mg/kg; n = 13) or 10% ethanol as the control vehicle (n = 10). Typically, tumors increased in volume by 400% over the duration of the study (2 weeks post-treatment initiation), and euthanasia was accomplished by CO_2 overdose.

MRI Scans

During MRI examinations, animals were anesthetized with 1–2% isoflurane/air, and body temperature was maintained by blowing warm air through the bore of the magnet using an Air-Therm (World Precision Instruments, Sarasota, FL). MR scans were performed immediately before treatment and every 3 days thereafter using a 9.4 T, 16 cm horizontal bore Varian (Palo Alto, CA) Direct Drive system with a quadrature rat head coil (Doty Scientific, Inc., Columbia, SC). DW images were acquired using a spin-echo sequence, with a navigator echo and gradient waveforms sensitive to isotropic diffusion [34], with the following parameters: repetition time (TR)/echo time (TE) = 4000/41 ms, field of view (FOV) = 30 mm, matrix size = 64 x 64, slice thickness = 2 mm, number of slices = 8, sweep width = 50 kHz, gradient pulse width = 10.5 ms, gradient pulse separation = 25 ms, and b-values (x-gradient, y-gradient, and z-gradient amplitudes) of 120 (5.3, 4.8, and 4.2 G/cm), 1200 (16.6, 15.0, and 13.1 G/cm), 1600 (19.1, 17.3, and 15.6 G/cm), 2000 (21.3, 19.2, and 17.4 G/cm), 3000 (25.9, 23.4, and 21.3 G/cm), and 4000 sec/mm^2 (29.7, 26.9, and 24.6 G/cm) with averages of 1, 1, 1, 1, 4, and 16, respectively. DWI scans were constrained to a total scan time of 2 h based upon an institutionally approved animal protocol. In addition to the time constraint, only voxels in the tumor with a signal to noise (SNR) > 6 at high diffusion weighting (i.e., b = 4000 sec/mm^2) were evaluated. The first step in maintaining this constraint was to determine a voxel size that provides adequate SNR and resolution within a 2 h MR experiment. As observed in Chenevert et al. [3], 9L rodent brain tumors treated with 13.3 mg/kg BCNU can exhibit an ADC as high as 1.5 x 10^{-3} mm^2/sec. A sucrose phantom of 15% sucrose/water, with a measured ADC of 1.4 x 10^{-3} mm^2/sec over the b =

120–1200 sec/mm^2 range, was used to determine sequence parameters (i.e., FOV, slice thickness, and averages) that provide a SNR > 6 at b = 4000 sec/mm^2 [35].

Post-processing of Diffusion-Weighted Images

All MRI data were transferred to a PC, interpolated to a matrix size of 256 x 256, and analyzed using in-house software developed in MATLAB (The MathWorks, Inc., Natick, MA). Curve-fitting was performed using an un-weighted non-linear least-squares algorithm using an initial parameter guess based on literature values. Diffusion signal decay, found to follow a nonmonoexponential trend in healthy brain tissue and tumor from our animal model, was analyzed using three diffusion approaches.

Two-Point Analytical Formalism

The simplest of all three techniques investigated captures the nonmonoexponential trends observed in the DW images from a two-point subsampling of the signal decay curve using the following equation:

$$ADC_{1-2} = \frac{ln\left(S_1/S_2\right)}{(b_2-b_1)}, \qquad [1.1.1]$$

where S_1 and S_2 are the signal intensities at b-values b_1 and b_2, respectively, and $ADC_{1–2}$ is the diffusion coefficient obtained using b_1 and b_2. The conventional mono-exponential ADC was calculated using b-values of 120 and 1200 sec/mm^2 ($ADC_{120–1200}$), which captures the rapid diffusion decay in the nominal-b regime while avoiding perfusion effects observed at very low b-value (<100 sec/mm^2). Slow diffusion decay, observed in the high-b regime, was captured by determining the ADC using b-values of 2000 and 4000 sec/mm^2 ($ADC_{2000–4000}$). The ratio of $ADC_{2000–4000}/ADC_{120–1200}$, defined as R_{TP}, was used as an empiric index of nonmonoexponential behavior derived from the piece-wise two-point formalism. An R_{TP} close to one implies mono-exponential behavior, whereas a decreasing R_{TP} implies greater disparity in signal decay between low-b and high-b regimes, thus greater multiexponential behavior.

Stretched Exponential Formalism

This formalism defines the divergence of a diffusible particle from mono-exponential trends as anomalous diffusion (29,36). Referred to as the stretched exponential, this formalism portrays molecular diffusion in a locally nonhomogeneous environment, which is represented by the equation:

$$S(b) = S_0\left[e^{-(b*DDC)^{\alpha}}\right], \quad [1.1.2]$$

where S is the signal intensity at a given b-value, S_0 is the signal intensity with no diffusion weighting, DDC is the distributed diffusion coefficient, and α is the anomalous exponent bound between 0 and 1 [29, 36]. By inspection of Eq. 2, it should be clear that α = 1 is equivalent to monoexponential diffusion signal decay. Conversely, an α approaching 0 indicates a high degree of multiexponential signal decay, thus α will be used as the nonmonoexponential index derived from the stretched exponential formalism. This convention maintains consistency with Bennett et al.'s [29] definition of a as a diffusion heterogeneity index, although we remind the reader that a numerically high a value (~1) represents a low intravoxel diffusion heterogeneity approaching monoexponential decay, whereas a numerically low a value represents a high degree of diffusion heterogeneity exhibited as multiexponential decay. It is also worth emphasis that the term "heterogeneity" in this context refers to intravoxel heterogeneity of exponential decays, as opposed to intervoxel heterogeneity of diffusion coefficients as often is the case, particularly in tumor. Parameter maps of DDC and α were calculated by linearizing the stretched exponential equation and then fitting it to the DW images in a pixel-wise manner over all b-values using a linear least-squares technique.

Biexponential Model

Calculation of the biexponential diffusion components was performed by a pixel-wise fit to all DW images of the following equation:

$$S(b) = S_0(V_1 e^{-bD_1} + V_2 e^{-bD_2}), \quad [1.1.3]$$

where S and S_0 are signal intensities at a given b-value and no diffusion weighting, respectively, D_1 and D_2 are the fast and slow diffusion coefficients, respectively, and V_1 and V_2 are the fast and slow signal fraction contributions, respectively. The fractional signal components are related by the expression $V_2 = 1 - V_1$. The fit was performed using a nonlinear least-squares technique.

Image Analysis

Volumes of interest (VOI) over the tumors were manually contoured on the low b-value DWI, which exhibits T_2-weighted contrast and serves for quantification of tumor volume. Low SNR voxels were excluded before calculation of mean parameter values within the VOI from each diffusion formalism. To accomplish this, voxels having SNR ≤ 6 on the b = 4000 sec/mm^2 DWI were identified by software in a binary 3D mask. The mask was then applied to all DW

images guaranteeing that only those voxels with a SNR > 6 were evaluated. Regions of necrosis or blood pools, typically observed as hypo-intense on T_2-weighted images, were manually omitted from the VOIs. Parameter change with respect to treatment was assessed using the percent change of the mean of each parameter (100x [PostTherapy – PreTherapy] / PreTherapy).

Histology

An additional six animals were used for obtaining histology of the tumors for control (n = 3) and treated animals (n = 3) 6 days post-treatment. 9L tumors from these animals were placed in buffered formalin overnight, dehydrated in 70% ethanol, and subsequently embedded in paraffin. Tissue sections were prepared for histological processing by routine techniques. Briefly, paraffin sections (5 mm thick) were cut on a microtome and heated for 20 min at 65°C. Slides were deparaffinized in xylene with three changes for 5 min each and then rehydrated through an alcohol gradient for 2 min each (100% alcohol, 95% alcohol, and 70% alcohol). Sections were first stained using a Gill's 2x hematoxylin solution and then subsequently stained with eosin.

Statistics

A paired Student's t-test was used to assess significance between the percent changes in each parameter post-treatment initiation from pretreatment values and between the percent change in similar parameters for each formalism at individual time points in the treated group. Group comparisons were assessed for each parameter at individual time points using an independent sample Student's t-test. Treatment efficacy on overall survival was assessed by log-rank test and displayed using a Kaplan-Meier survival curves. All statistical computations were performed with a statistical software package (SPSS Software Products, Chicago, IL). Statistical significance was assessed at $P < 0.05$.

1.1.3: Results

Representative DW images, acquired at b-values of 120, 1200, 3000, and 4000 sec/mm^2, are demonstrated in Figure 1.1.1. Using low b-value images, delineation of tumor extent allowed for tumor volumes to be measured over time. Although the tumor volume in treated animals did appear to have a slower rate of growth than controls, this did not result in statistical differences in tumor volume between groups at individual time points (Figure 1.1.2a). Nevertheless, as presented in Figure 1.1.2b, the median survival of treated animals (9 days with a 95% confidence interval of 8.2–9.8 days) was found to be significantly longer than control animals (5 days with a

95% confidence interval of 3.8–6.2 days; P = 0.001). Increased longevity in treated animals was consequent to tumor cell death, which was verified by histology. Histological sections of representative control and treated animals at day 6 post-treatment initiation are presented in Figure 1.1.3. Following BCNU treatment, fewer nuclei were observed in the treated tumor than control, suggesting massive cell kill in the tumor volume of treated animals. An increase in pleomorphism and giant cells was also evident in the treated tumors. Tumor growth rate kinetics and histology were consistent with previous findings using the 9L gliosarcoma rat brain tumor model [6].

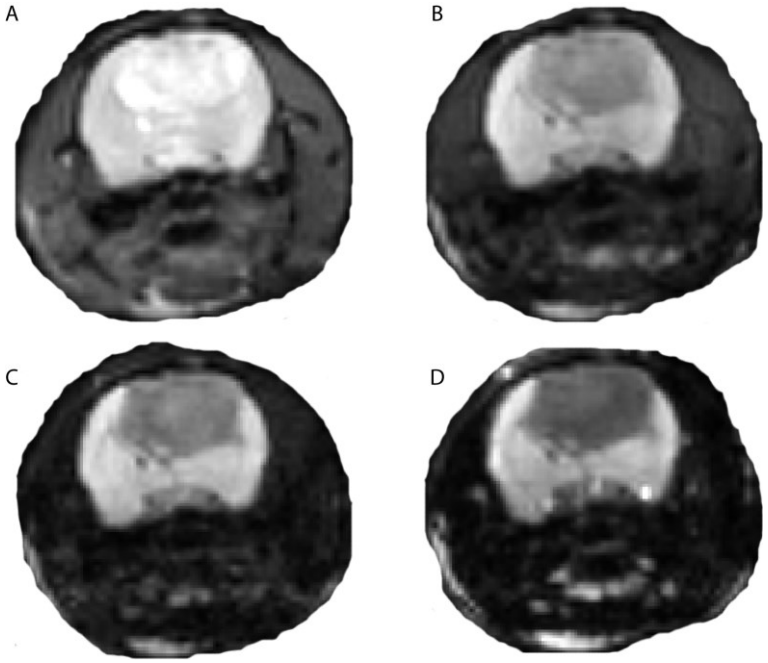

Figure 1.1.1 Representative diffusion-weighted images of a rat brain harboring a 9L gliosarcoma acquired at b-values of (a) 120, (b) 1200, (c) 2000, and (d) 4000 sec/mm^2. Images were independently scaled for better visualization at higher b-values.

Presented in Table 1.1 is a summary of the parametric indices generated from the three formalisms for control and treated tumor groups acquired at baseline. Significant differences in indices with similar diffusion properties were observed between all formalisms. In contrast, group comparisons did not result in statistical differences for any given parameter. To verify the accuracy of our biexponential fit to the data, pretreatment values were calculated in healthy rat striatum. Biexponential results of D_1 and V_1 (0.88 x 10^{-3} mm^2/sec and 0.79) were found to be comparable with previous values in brain tissue [28]. In contrast, D_2 (0.42 x 10^{-3} mm^2/sec) was

2.5x that of Niendorf et al.'s measurement [28] of 0.165 x 10^{-3} mm^2/sec, which could be a result of higher diffusion weighting, up to 10^4 s/mm^2 as opposed to the 4000 s/mm^2 used here.

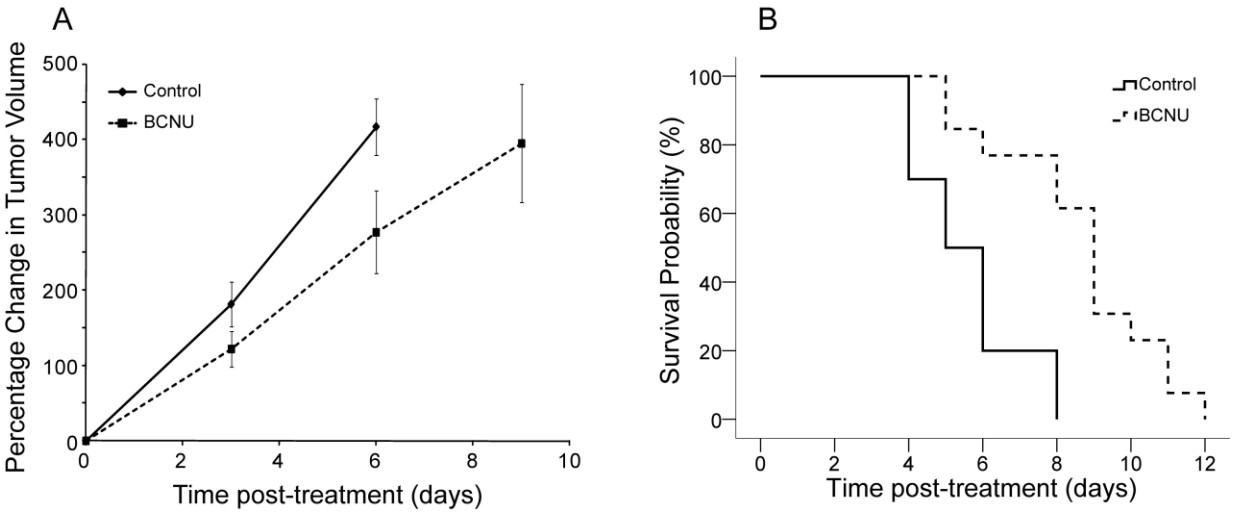

Figure 1.1.2: (a): Plot over time of the mean tumor volume. Data presented as mean ± SEM. Significant difference in mean tumor volume between groups was assessed using an unpaired Student's t-test. P values are provided at individual time points. (b): Kaplan-Meier survival plot for overall survival is presented for control and treated animals. Controls are shown as solid line with diamond markers and treated are shown as dashed lines with square markers. Significant differences in overall survival were observed between groups as assessed using a log-rank test (P = 0.001).

Table 1.1: Mean Parameter Values at Baseline. Pre-treatment data are presented for controls (n=10; top) and treated animals (n=13; bottom) as means (SEM).

Two-Point	Stretched Exponential	Biexponential
$ADC_{120\text{-}1200}$ [x10^{-3} mm^2/s]	DDC [x10^{-3} mm^2/s]	D_1 [x10^{-3} mm^2/s]
1.02 (0.02)	0.97 (0.02)	1.39 (0.05)
0.99 (0.03)	0.95 (0.02)	1.38 (0.05)
$ADC_{2000\text{-}4000}$ [x10^{-3} mm^2/s]		D_2 [x10^{-3} mm^2/s]
0.71 (0.02)		0.68 (0.03)
0.69 (0.01)		0.62 (0.02)
R_{TP}	α	V_2
0.71 (0.02)	0.83 (0.01)	0.39 (0.01)*
0.71 (0.02)	0.87 (0.01)	0.35 (0.01)
$ADC_{120\text{-}1200}/R_{TP}$	DDC/α	D_1/V_2
1.46 (0.07)	1.10 (0.04)	3.99 (0.18)
1.48 (0.05)	1.09 (0.03)	3.74 (0.19)

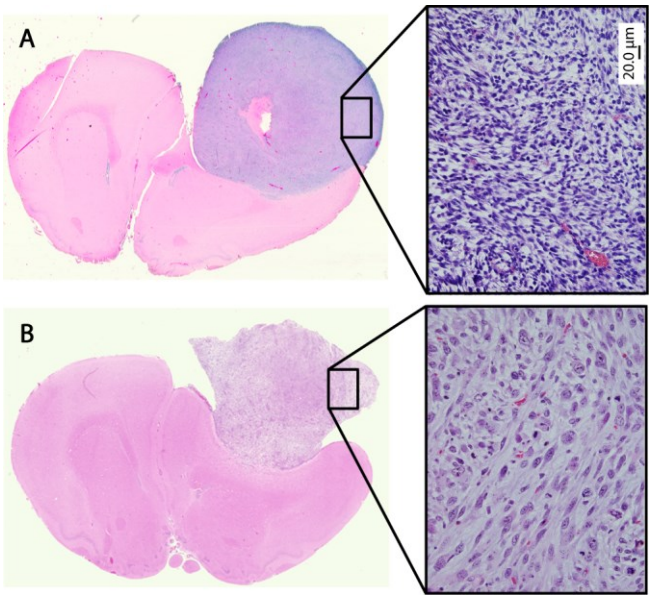

Figure 1.1.3: Hematoxylin–eosin-stained sections of intracerebral 9L tumors for representative (a) control and (b) BCNU-treated animals on day 6 post-treatment.

As shown in Figure 1.1.4, maps of parameters more sensitive to "fast diffusion" properties pretreatment (left column) and 6 days following BCNU treatment (right column) were generated over the tumor volume and superimposed on T_2-weighted images. Top-row images (Figure 1.1.4a,d) represent $ADC_{120–1200}$, middle-row images (Figure 1.1.4b,e) are DDC, and bottom-row images (Figure 1.1.4c,f) are D_1. In addition, the full time course of $ADC_{120–1200}$, DDC, and D_1 expressed as percent change from pretreatment values are illustrated in Figure 1.1.4g–i, respectively. D_1 was found to be significantly larger than $ADC_{120–1200}$ and DDC at baseline (Table 1.1) and at day 6 post-treatment initiation as well as having, in absolute terms, a larger dynamic range (~1.5–3.0 x 10^{-3} mm^2/sec) within the tumor volume allowing easier visualization of tumor features (Figure 1.1.4c,f). As for the responsiveness of these indices to treatment, the percent change from baseline peaked at day 6 post-treatment initiation, followed by a descent toward baseline at day 9 (Figure 1.1.4g–i). Near identical trends were observed for $ADC_{120–1200}$ and DDC with significant group and baseline value differences observed on days 3 and 6. Similar results were observed for D_1 except for the negligible group differences at day 3 post-treatment-initiation, which is attributed to the slower rate of ascent from baseline (Figure 1.1.4i). Although change in D_1 was found to be most responsive to treatment with a ~25% increase at day 6 from baseline, it was not found to be significantly larger at this time point or

any other time point from what was observed for change in $ADC_{120–1200}$ and DDC (P = 0.204 and P = 0.711, respectively, for day 6).

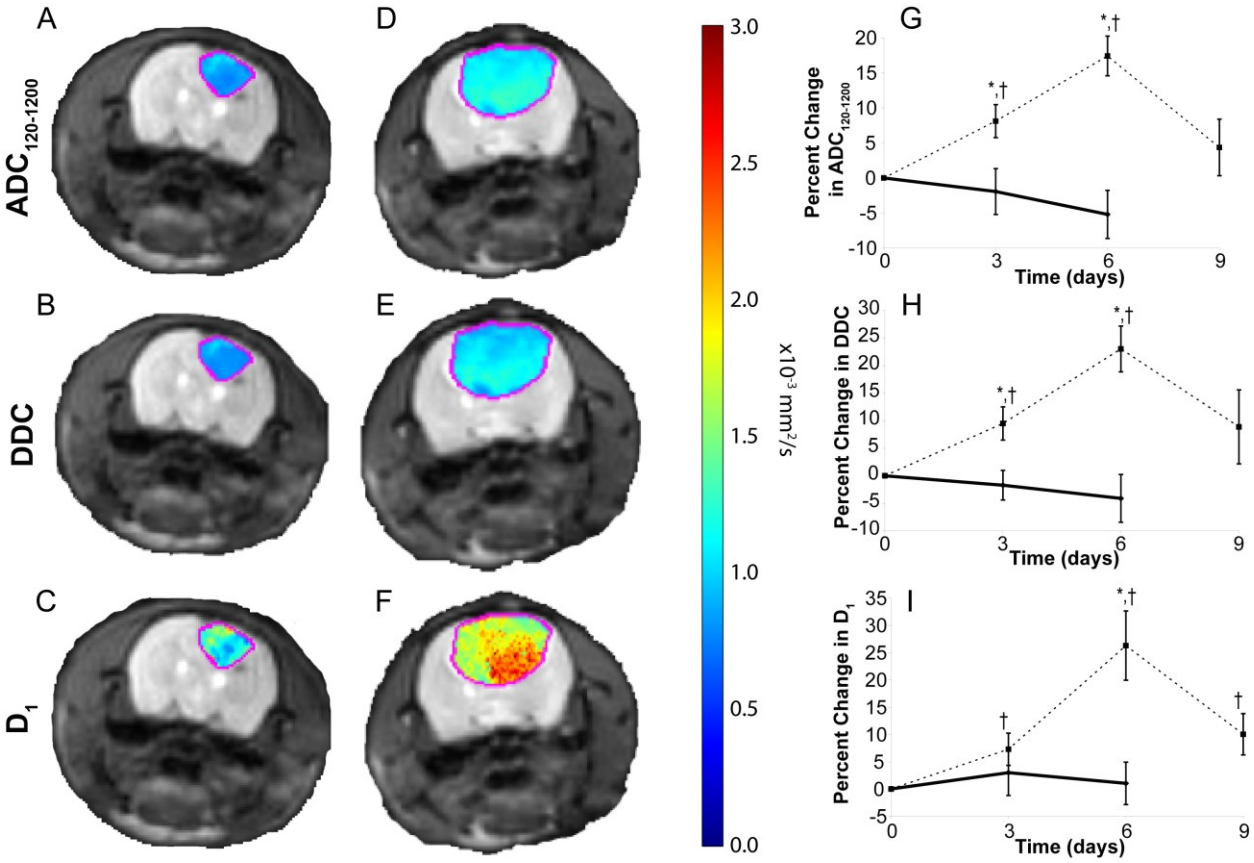

Figure 1.1.4: Representative maps and line plots of percent change in parameters sensitive to ‘‘fast diffusion’’ generated using (a, d, g) twopoint, (b, e, h) stretched-exponential, and (c, f, i) biexponential formalisms are provided. Diffusion maps, overlaid on T2-weighted images of a rat brain, were acquired at days 0 (a, b, c) and 6 (d, e, f) post-treatment initiation. Line plots (g, h, i) consist of mean values and standard errors from control and treated groups over the entire experiment. Data are presented as the mean ± the standard error of the mean. The symbols † and * designate significant differences from baseline and between groups, respectively. Statistical significance was assessed at $P < 0.05$.

Analogous parametric maps and line plots to Figure 1.1.4 are illustrated in Figure 1.1.5 for quantities sensitive to the “slow diffusion” component of the decay curve, namely $ADC_{2000–4000}$ (Figure 1.1.5a,c,e) and D_2 (Figure 1.1.5b,d,f). In general, $ADC_{2000–4000}$ and D_2 showed little change in day 6 values from baseline (Figure 1.1.5a–d). Percent change in the mean values over time corroborates observations found in the maps from the representative animal (Figure 1.1.5a–

d) with $ADC_{2000–4000}$ and D_2 peaking at less than 10% of baseline. Group differences were only observed at day 3 for D_2, partly attributed to a drop in control D_2. Interestingly, both $ADC_{2000–4000}$ and D2 resulted in ~7% decrease from baseline on day 9 post-treatment initiation (Figure 1.1.5h,i), which correlated with the descent back to pretreatment values observed in diffusion coefficients sensitive to "fast diffusion" (Figure 1.1.4).

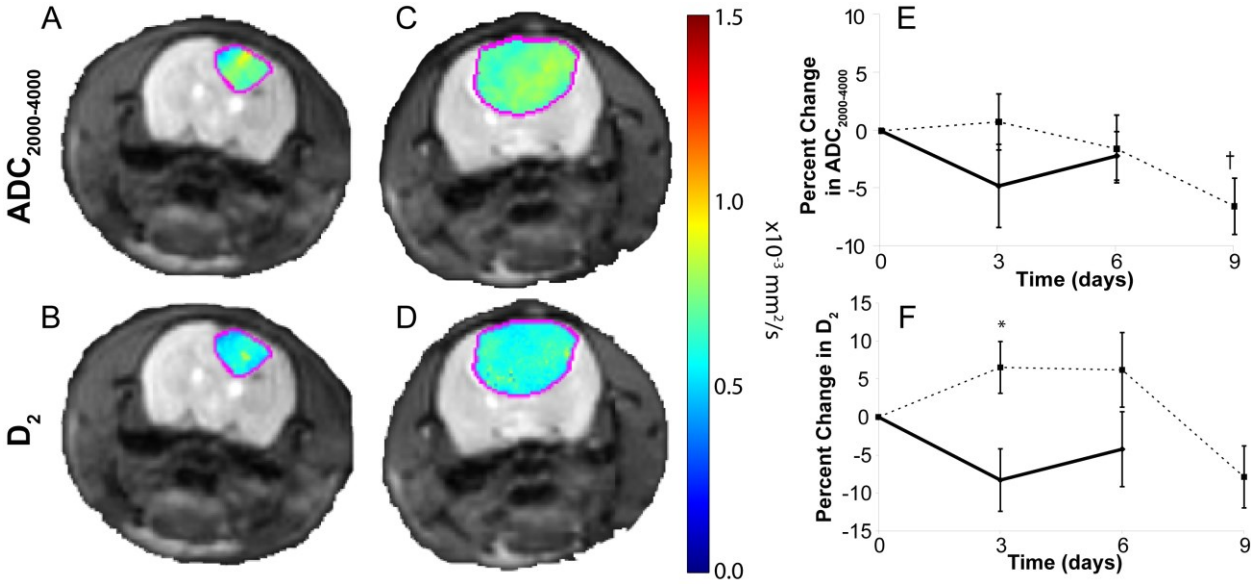

Figure 1.1.5: Representative maps of the ''slow diffusion'' coefficients and line plots of percentage change in parameters generated using (a, c, e) two-point and (b, d, f) biexponential formalisms are provided. Diffusion maps, overlaid on T2-weighted images of a rat brain, were acquired at days 0 (a, b) and 6 (c, d) post-treatment initiation. Line plots (e, f) consist of mean values and standard errors from control and treated groups over the entire experiment. Data are presented as the mean ± the standard error of the mean. The symbols † and * designate significant differences from baseline and between groups, respectively. Statistical significance was assessed at $P < 0.05$.

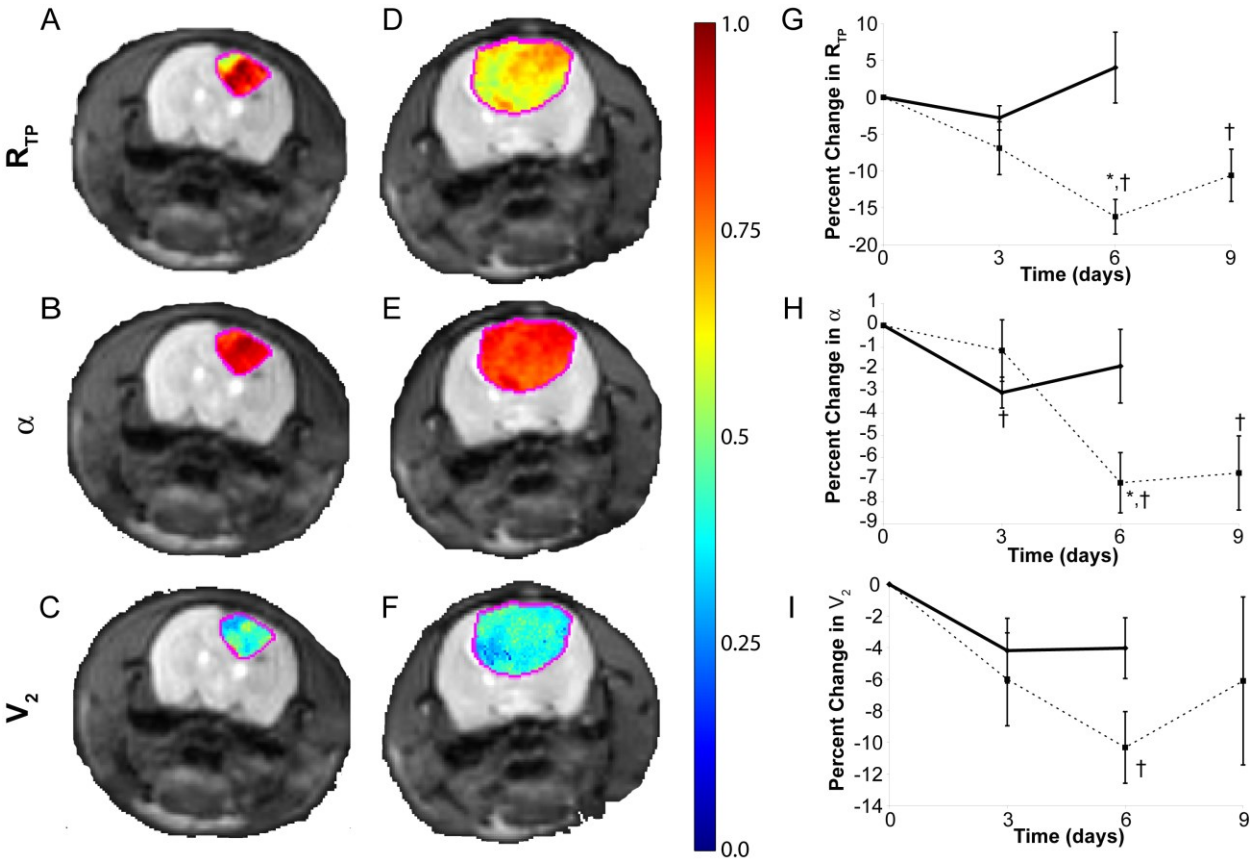

Figure 1.1.6: Representative nonmonoexponential metric maps and line plots of percentage change in parameters generated using (a, d, g) two-point, (b, e, h) stretched-exponential, and (c, f, i) biexponential formalisms are provided. Metric maps, overlaid on T2-weighted images of a rat brain, were acquired at days 0 (a, b, c) and 6 (d, e, f) post-treatment initiation. Line plots (g, h, i) consist of mean values and standard errors from control and treated groups over the entire experiment. Data are presented as the mean ± the standard error of the mean. The symbols † and * designate significant differences from baseline and between groups, respectively. Statistical significance was assessed at $P < 0.05$.

As discussed previously, a comparison of the absolute numerical value of nonmonoexponential metrics is not meaningful because of differences in how these parameters are defined. Qualitatively, R_{TP} was most sensitive to treatment exhibiting the largest percent drop from baseline values (Figure 1.1.6). The remaining parameters showed similar qualitative trends from baseline to day 6 post-treatment-initiation. A significant drop from pretreatment values was observed at day 6 for R_{TP} (−11%), α (−7%), and V_2 (−6%). R_{TP} and α continued to have significantly lower values to baseline at day 9, which was not established by V_2 because of scatter in the data. Group differences were only found at day 6 for R_{TP} and α. The ratio of D_2 and

D_1, as obtained from the biexponential formalism, provided analogous results to R_{TP} (data not shown). Although the mean value of D_2/D_1 decreased by more than 15%, these results were not found to be statistically different from the controls.

1.1.4: Discussion

DW MRI has shown potential as a surrogate biomarker for treatment response in cancer patients [37-40]. Acquisition of diffusion maps is typically performed at relatively moderate diffusion weighting, i.e., b-values that typically span the 0–1000 sec/mm^2 range. It is speculated that water diffusion measurements at higher b-values may provide increased sensitivity to relevant drug-induced changes in tumor composition by virtue of possible therapeutic alteration of cellular constituents responsible for the "slow diffusion" components of signal decay observed at relatively high b-values. This study sought to determine the sensitivity of diffusion parameters derived from various mathematical formalisms of nonmonoexponential water diffusion to treatment-induced tissue alteration following treatment of the 9L glioma model.

Previous work by our group using the 9L brain tumor model has shown that ADC calculated using moderate b-values can increase by up to 60% within a week following a single dose (13.3 mg/kg) of BCNU (3). As measured in this study, parameters sensitive to "fast diffusion" showed similar trends following a single bolus (9.98 mg/kg) of BCNU, all peaking by day 6 post-treatment-initiation. The maximum percent change in parameter value from baseline was observed in D_1. This is expected because D_1 is a more specific measurement of "fast diffusion" than DDC and $ADC_{120–1200}$, which are not completely devoid of the "slow diffusion" properties in the signal decay curve. A positive therapeutic effect was confirmed by an increased overall survival (Figure 1.1.2) as well as direct evidence from histological tumor sections comparing treated versus untreated tumors (Figure 1.1.3). Another characteristic trend of ADC following treatment, which has been observed here and by others, is the temporally evolving descent to baseline values. This has been found to correlate with tumor cell repopulation, which has been reported in the literature [28]. In contrast, those indices specifically sensitive to "slow diffusion" exhibited a negligible change post-treatment initiation until day 9 where a drop had occurred in both parameter values when compared with baseline. The lack of response following treatment and the sudden drop in $ADC_{2000–4000}$ and D_2 during cell repopulation, which is reflected in the diffusion coefficients sensitive to "fast diffusion" descent to baseline, is quite perplexing,

suggesting independent mechanisms affecting the "fast" and "slow" diffusion properties of the tissue. Additional mechanisms, such as macrophage infiltration and clearance of macromolecules, may also contribute to our observations. Despite subtle variations in the trends of the parameters with either "fast" or "slow" diffusion properties, there was no significant difference in the percent change from baseline between diffusion parameters with like properties.

As opposed to the diffusion coefficients, the nonmonoexponential metrics, R_{TP}, α, and V_2, are defined differently and thus cannot have the same interpretation, even though they have similar trends. Consequent to the negligible change in $ADC_{2000–4000}$, R_{TP} is driven almost exclusively by $ADC_{120–1200}$ for most of the study. Not until day 9, did we see a divergence from this dependence, which is partly attributed to the mirrored descent observed in $ADC_{2000–4000}$ to $ADC_{120–1200}$ resulting in a negligible change in R_{TP} from day 6 to day 9 post-treatment initiation. Analogous but not significant results were observed for D_2/D_1. Large variability in the measurements of D_1 and D_2 (Figs. 4 and 5) from the nonlinear fit most likely contributed to the non-statistical difference in D_2/D_1 between groups. In contrast, the slow diffusion signal fraction, V_2, defines the proportion of water signal in the slow compartment independent of water diffusivity. The drop in V_2 suggests shrinkage of the slow compartment volume fraction, conversely an expansion of the fast compartment volume fraction, following treatment initiation. The anomalous exponent α represents the deviation of signal attenuation from mono-exponential behavior ($\alpha = 1$). This perturbation is assumed to be attributed to increased heterogeneity within the tissue. The decrease in α seen in Figure 1.1.6h suggests an increase in tumor intravoxel heterogeneity that maximizes at day 6 and continues to day 9. Following treatment of the tumor with BCNU, a loss in tumor cellularity (Figure 1.1.3) pushed the attenuation curve further from monoexponential behavior than what was observed from control and baseline values (Table 1.1). Because of similar trends in the nonmonoexponential metrics and the lack of response to treatment of the "slow diffusion" indices, one may speculate that the "fast diffusion" properties within the tumor dominate what we observe for R_{TP}, α, and V_2 following treatment. Various theories have been proposed to provide a physical account of the deviation in diffusion-sensitive signal attenuation from monoexponential behavior in biological tissue [20, 21, 41]. Use of these theories to determine the exact physical properties that govern nonmonoexponential water diffusion warrants further investigation but is beyond the scope of this study.

Irrespective of the mechanisms driving nonmonoexponential behavior in diffusion-sensitive signal attenuation, high b-value DWI provides additional advantages over conventional mono-exponential ADC measurements that may provide a more sensitive biomarker for tumor treatment response and characterization. The conventional approach for measuring ADC, b-values around 1000 sec/mm^2, is hindered by the presence of highly diffuse tissue, such as cysts and necrotic areas, which may reside within or around the tumor volume adding increasing difficulty in localizing viable tumor. At higher b-values, these rapidly diffusing regions within tumors are essentially filtered out leaving only densely packed tumor that has lower ADC values. Recent research investigating the sensitivity of high b-value DWI for treatment assessment has shown promising results. Mardor et al. have demonstrated in patients with malignant brain lesions that the ratio of D_1 and V_2 [defined as R in Eq. 1 [6]] is highly sensitive to radiation-induced changes in the tumor. This parameter not only demonstrated a significant change from baseline as early as 1 week post-treatment initiation but was capable of predicting clinical outcome in all of the studied patients. In contrast, conventional mono-exponential ADC (comparable to $ADC_{120–1200}$ in this study) was only capable of predicting response in about half of their patient population. It is not clear whether R, as presented by Mardor et al., is driven by D_1 or V_2, or if D_1 or V_2 alone would provide ample sensitivity to predict tumor response to treatment as this analysis was not provided in their study. We further evaluated the approach proposed by Mardor et al. [6] (D_1/V_2) using our data. The percentage change in D_1/V_2 from baseline was ~42% in the treated group at day 6 post-treatment, which was significantly different from controls [–2% ($P = 0.002$)]. Although, D_1/V_2 demonstrated a percentage change 1.6x greater than that generated by D_1, this increase was not statistically different ($P = 0.15$). The probable cause for the lack of significance was the additional scatter in the data as a result of the nonlinear fit. Unlike DWI at moderate b-values, acquisition of diffusion-sensitized signal at b-values of >2000 sec/mm^2 is not trivial. This is attributed to the exponential loss of signal due to increased attenuation at high b-values. As signal approaches the noise floor, artificial nonmonoexponential trends in the signal profile are observed, adversely affecting the slow diffusion measurements. To accommodate these losses, images must be acquired with sufficient SNR resulting in longer scan times, which may not result in patient compliance. Additional computational time is also required when fitting the biexponential formalism to the DWI data. In

this study, ~30 min per dataset was required for the voxel-wise nonlinear fit. The stretched-exponential formalism does not suffer from this deficiency because it can be linearized and solved using an algebraic solution of the linear least squares. Numerically fitting two parameters for the stretched exponential model can also be more stable relative to fitting three parameters required by the biexponential model.

There are several limitations to our experimental approach that must be discussed. Scan time was limited to no more than 2 h. This in turn limited the signal averaging, i.e., SNR, and range and number of b-values used per scanning session. As discussed, large slice thicknesses and small matrix sizes were used to maintain our self-imposed constraint of SNR > 6. This likely resulted in unavoidable partial volume averaging in the tumor, which would be less with thinner slices. Another area of concern was the lack of sufficiently high b-values, which are most sensitive to "slow diffusion" rates. This could have possibly led to an overestimation of the D_2 in the biexponential fit. Using the mean D_1 and D_2 determined at day 6 post-treatment initiation, we found in treated tumor tissue (1.7×10^{-3} mm^2/sec and 0.6×10^{-3} mm^2/sec), less than 4% ($\exp(-2000*0.0017) \sim 3.3\%$) of the fast diffusion signal was still present at a b-value of 2000 sec/mm^2, whereas 29.9% of the slow diffusion component signal was still available. Finally, the biexponential diffusion coefficients, D_1 and D_2, acquired here for healthy striatum varied by only a factor of 2, contrary to the factor of 5–10 typically observed in the literature. Based on the observations of biexponential diffusion in rodent models, D_1 as measured in this study is in accordance with literature results (0.88 here, compared to 0.82 and 0.77×10^{-3} mm^2/sec in the literature), whereas D_2 appears to be overestimated by a factor of 2 (0.43 here, compared to 0.17 and 0.18×10^{-3} mm^2/sec in the literature) [28, 41]. The discrepancy in D_2 is most probably due to the lack of sufficiently high b-values used in this study. Finally, the filtering of low SNR voxels from our whole-tumor analysis may have inadvertently removed necrotic regions in the tumor. Signal intensity within regions of high diffusivity or short T_2 due to blood products is prone to have low signal at high b-value. As discussed earlier, the contribution of noise in our data was reduced by filtering voxels whose SNR < 6 on the highest weighted DWI (4000 sec/mm^2). This maintained voxels having high SNR at high b-values but removed regions of high diffusivity or low SNR (i.e., necrosis, cystic, and blood products) from the whole-tumor analysis. To avoid excessive loss of tumor volume while maintaining SNR ≥ 6, image matrix size and slice

thickness were set to maintain adequate SNR at a cost of resolution. The volume fraction of tumor analyzed at days 6 and 9 post-treatment initiation in treated animals was 93.5% ± 11.3% and 94.5% ± 9.9% (means 6 SD), respectively. Based on these values, filtering tumor regions that contribute to low SNR in DWI at high b-value did not result in excessive loss of tumor volume for our analysis in this study.

We have demonstrated the sensitivity of various nonmonoexponential diffusion formalisms for monitoring early response to chemotherapeutic treatment for brain tumors in an animal model. The extent of the response varied, with the fast diffusion component of the biexponential formalism exhibiting the largest percent change from baseline than other diffusion coefficient; slightly more than was observed in the conventional monoexponential ADC and DDC measurements. However, for this 9L glioma model treated with a single dose of BCNU, the more complicated formalisms provided no additional sensitivity to treatment response over what was observed using conventional mono-exponential ADC measured over the standard modest b-value range.

1.2: Diffusion Model Sensitivity Analysis

1.2.1: Introduction

As was discussed in the previous section, true water diffusion in living tissues is very complex, relying on various structural and chemical properties intrinsic to the tissue. In finding useful quantitative readouts from the limited information obtained from diffusion-weighted imaging, it is necessary to distill the assumed phenomenon down to a simpler, more manageable model. In measuring tissue response, the model readouts must be related to real physical properties in order to derive meaning from the data.

Due to the unavoidable noise associated with quantitative image values, it is important to characterize the error associated with parameter readouts when fitting the model to data. In performing a sensitivity analysis of the model, we can determine which model parameters most affect the output as well as which will show the greatest sensitivity to a small change in the acquired data. A greater magnitude change in the sensitivity coefficient is indicative of a greater ability of the model to detect a change in the image data curve, which would be a useful property for an imaging biomarker. Also, by assessing the sensitivity of the fit parameters to noise we

may determine the expected accuracy of a measurement based on the image noise associated with data acquisition.

In this section I will perform two types of analyses to characterize model sensitivity and robustness: sensitivity analysis and noise analysis. Local sensitivity analysis is a tool that can be used to quantify the reaction of the model relative to a change in an individual input parameter, one parameter at a time. This local sensitivity coefficient will be evaluated near the input space of a known reference point as optimized from real data from the previous section. Parameters that show relatively low sensitivity may have higher error in their optimization readout due to the smaller effect they have on the model. It is also important to determine the sensitivity of optimized parameters to noise in the data. For this analysis multiple optimizations were performed, each time fitting the model to simulated noisy data. It is expected that greater noise in the data will produce greater error in the modeled parameters. By comparing the parameter and noise sensitivities between models, a measure of model robustness and stability may be determined. Both methods were used on the previously-mentioned diffusion models and results are presented below.

Table 1.2: Baseline diffusion model parameters for sensitivity analysis.

Mono-Exponential	Bi-Exponential	Stretched-Exponential
$ADC\ (mm^2/s)$	$D_f\ (mm^2/s)$	$DDC\ (mm^2/s)$
0.95×10^{-3}	1.1×10^{-3}	1.1×10^{-3}
	$D_s\ (mm^2/s)$	
	0.35×10^{-3}	
	f_f	α
	0.9	0.88

1.2.2: Methods

For each model (mono-exponential, bi-exponential, and stretched exponential), an initial fit was performed on a representative data set to obtain a set of model parameters to base sensitivity metrics upon. The fit was obtained using a manually-delineated volume-averaged signal intensity encompassing an untreated intra-cranial 9L tumor in a rat brain, approximating general tumor characteristics [42]. Baseline parameters for each model are shown in Table 1.2.

Model Sensitivity to Parameter Changes

A parameter local normalized model sensitivity coefficient, SC, was quantified as the partial derivative of the signal intensity model, $S(x_1, \cdots, x_n)$, with respect to the parameter of interest, x_i, at the reference parameter point, $[x_{1,0}, \cdots, x_{n,0}]$, both normalized by their reference values [43] (Appendix A):

$$SC = \frac{\delta S(x_{1,0}, \cdots, x_{n,0})}{\delta x_i} \cdot \frac{x_i}{S(x_{1,0}, \cdots, x_{n,0})}. \quad [1.2.1]$$

The values of SC were evaluated over the study's range of b-values.

Model Fitting Sensitivity to Noise

Noise, in the case of MRI magnitude images used in this experiment, was modeled as a Rician distribution [44], which for high SNR can be approximated as Gaussian:

$$p(x) = \frac{x}{\sigma^2} exp\left(-\frac{x^2+A^2}{2\sigma^2}\right) I_0\left(\frac{xA}{\sigma^2}\right), \quad [1.2.2]$$

where A is the true image intensity, σ is the standard deviation of the Gaussian noise, and I_0 is the modified zeroth-order Bessel function of the first kind. This noise model can be combined with the assumed noise-less image intensity curve using the following equation:

$$S_i' = \sqrt{\left(S + N_i(\sigma)\right)^2 + \left(N_i(\sigma)\right)^2}, \quad [1.2.3]$$

where the subscript i represents the ith b-value, S_i' is the noisy signal, S is the noise-less signal, $N_i(\sigma)$ is a random number from the Normal distribution with standard deviation σ. Noise was tested at values of σ set from 1 to 20% of the baseline voxel intensity values for each b-value. Since acquisitions using the diffusion sequence in the previous section were optimized for each diffusion-weighting separately, SNR was modeled as being equal for each b-value in the model. Noise simulation and subsequent fits were performed 500 times for each noise level. Curve-fitting was performed in Matlab (The MathWorks, Inc., Natick, MA), using an un-weighted non-linear least-squares algorithm and an initial guess based on findings in the previous section. Mean parameter error was determined by the following equation:

$$\varepsilon(\sigma) = \frac{\sum_{i=1}^{n}(p_0 - p_i)}{n * p_0} * 100, \quad [1.2.4]$$

where p_0 is the true parameter value and p_i is the fitted parameter value from the ith fit with noise standard deviation σ.

1.2.3: Results

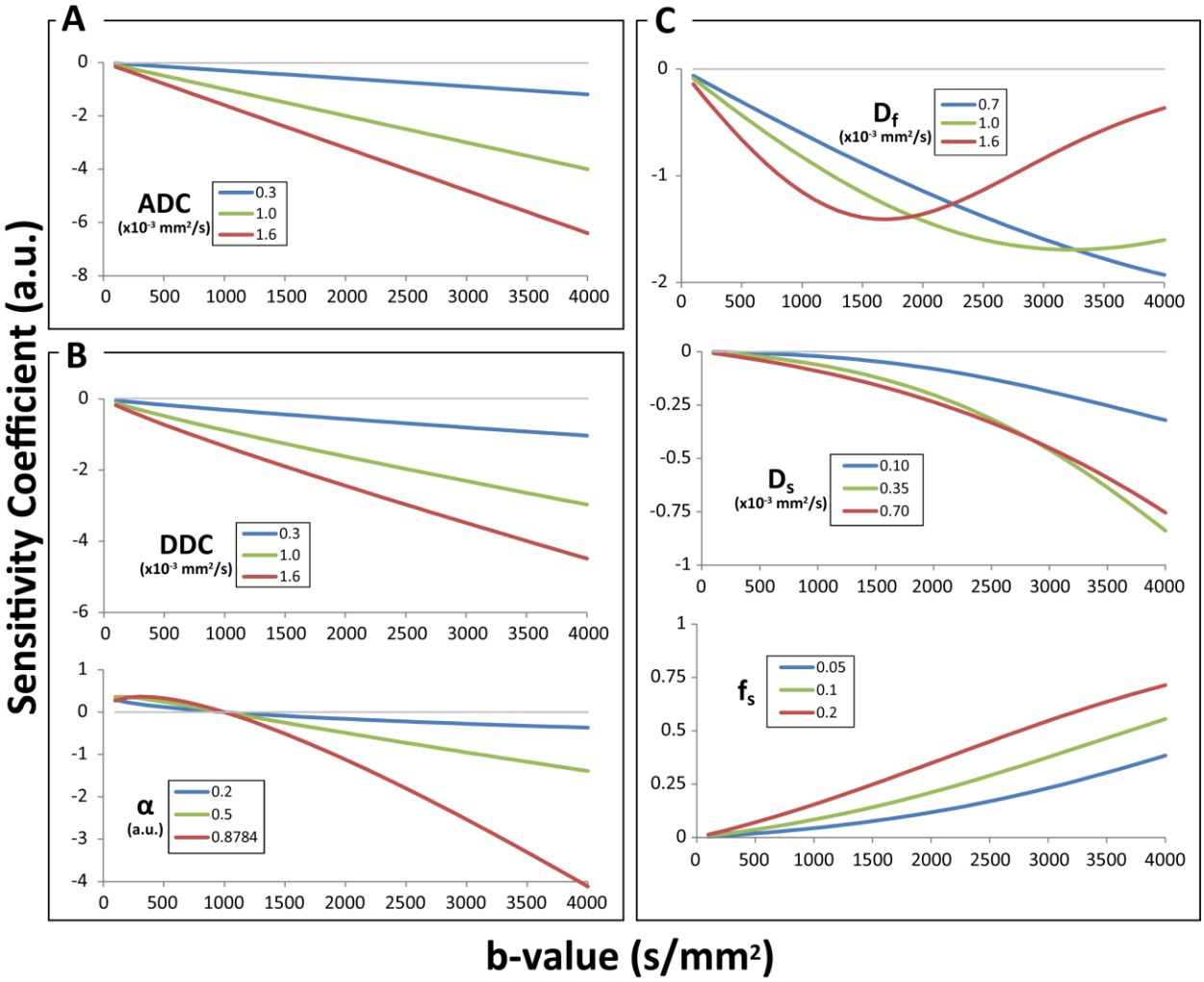

Figure 1.2.1: Plots of parameter sensitivity analysis for each diffusion model, sensitivity coefficient vs. b-value, for: (A) mono-exponential, (B) stretched-exponential, and (C) bi-exponential. Each plot shows three curves using varying reference values for the parameter of interest (blue = low, green = middle, and red = high).

Model Sensitivity to Parameters

Plots of the sensitivity coefficients over the range of b-values used in the previous section are shown in Figure 1.2.1A-C, with the zero-sensitivity threshold plotted as a gray horizontal line. Each plot shows the model sensitivity to the indicated parameter at three different levels of that value. All input parameters for all models have minimal sensitivity at low b-values, with general increases in sensitivity with b-value, and lower sensitivity over the range of b-values for lower values of the parameter. The mono-exponential ADC sensitivity coefficient (Figure 1.2.1A) decreases linearly with b-value, resulting in high negative sensitivity at higher b-values.

This indicates that a small increase in ADC will have a drastic effect on high b-value diffusion image signal intensity. Sensitivity plots of ADC and DDC (Figure 1.2.1B) look very similar, but when SC_{DDC} is analyzed at lower values of α_0 (higher diffusion coefficient heterogeneity) the shape shifts from negative linear to exponential with diminishing slope magnitude at higher b-values (not shown). The stretched-exponential parameter, α, also has very low sensitivity and actually has zero sensitivity around b = 1000 s/mm^2 in this case. Looking back at the model, this occurs where $b \cdot DDC = 1$ and $ln(1) = 0$ (Appendix A). In the case of the bi-exponential model (Figure 1.2.1C), however, D_f reaches a maximum sensitivity at high values of $D_{f,0}$ and starts to decrease with b-value after it reaches that peak. That peak is never reached in the lowest $D_{f,0}$ value ($7x10^{-4}$ mm^2/s) within the selected range of b-values. The diminishing magnitude of sensitivity to D_f is balanced by the increasing sensitivity magnitude of D_s and f_s. In general for these models, the sensitivity coefficient also has a trend of decreasing the individual parameter sensitivity with an increasing number of input parameters to the model.

Model Fitting Sensitivity to Noise

Plots in Figure 1.2.2 show results from model fits to simulated noisy data, presented as the mean absolute parameter measurement error plotted against the signal-to-noise ratio (SNR) and separated by model. As would be expected, lower SNR resulted in exponentially greater error in parameter estimation. The mono-exponential model (Figure 1.2.2A) showed the least sensitivity to noise, with ~6% measurement error at an SNR of 10. The bi-exponential model (Figure 1.2.2B) on the other hand had the greatest sensitivity to noise overall, with average errors at SNR=10 of 57%, 104%, and 392% in D_f, D_s, and f_s, respectively. At SNR=100 errors in ADC, DDC, and α were less than 2%, but bi-exponential parameter errors were still fairly significant with means of 7%, 41%, and 79% for D_f, D_s, and f_s, respectively. Figure 1.2.2d shows an increasing trend of diffusion coefficient optimization error with the number of model inputs, with 0.7% deviation in ADC (one input parameter) compared to almost 7% deviation in D_f (three inputs).

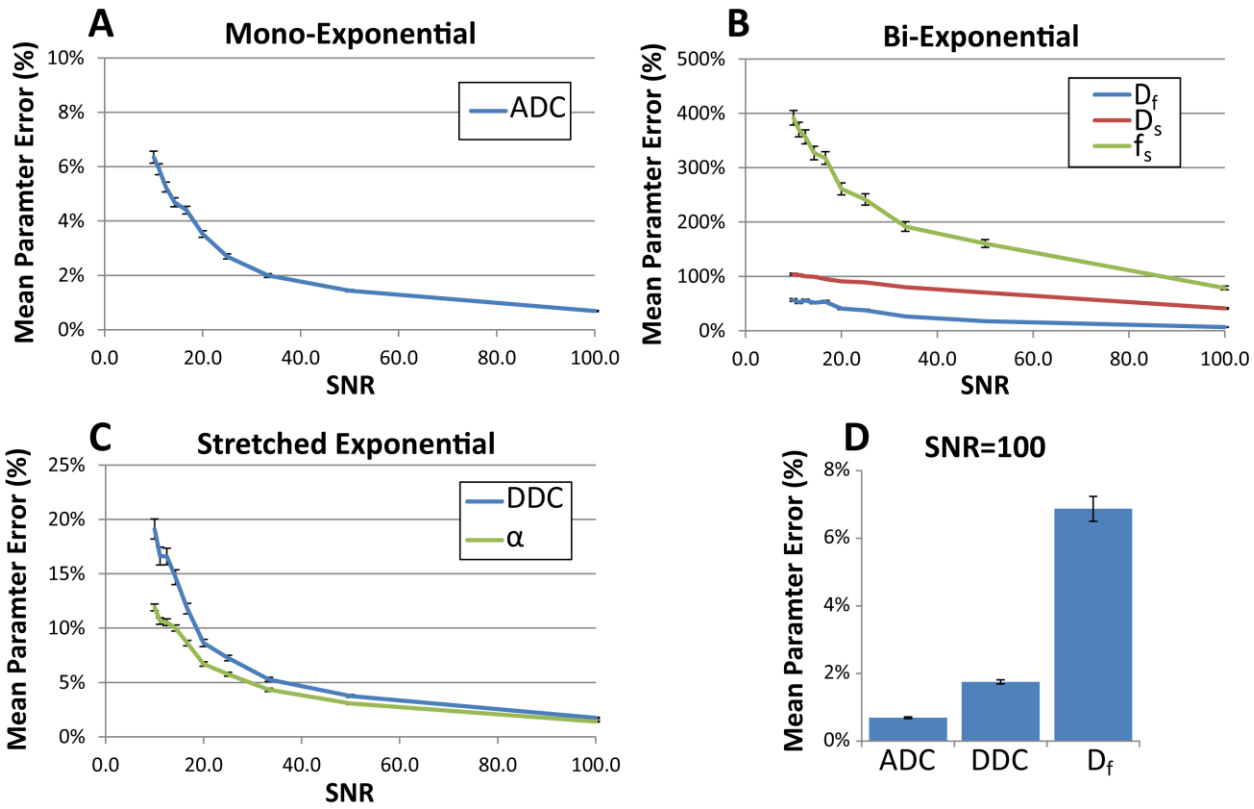

Figure 1.2.2: Plots of noise analysis results, with (A-C) mean absolute percent change plotted against baseline SNR and (D) comparison between diffusion coefficients of the three models at SNR=100. Errors are shown as ± SEM (too small to see on the mono-exponential plot).

1.2.4: Discussion

Diffusion MRI has been shown to be useful in detecting tumor response to therapy using various pre-clinical tumor models as well as clinical studies. Recent findings of non-mono-exponential diffusion behavior in living tissue spurred increased interest in determining a more suitable diffusion model for quantification of these images [21]. For the purpose of this manuscript, two established models (stretched-exponential [29] and bi-exponential [21]) were evaluated against the traditional mono-exponential formalism in order to determine their stability and sensitivity in detecting changes in tumors due to therapy.

Noise in magnitude MRI has been well-characterized [44], and its effect is critical to diffusion MRI in which signal is expected to significantly drop at high b-values. In order to maintain high SNR in high b-value images, multiple averages are often used on an image-by-image basis, allowing SNR not to vary over the course of diffusion weighting. However, this limits the practical range of b-values by time limitations of image acquisition. Deviation from

mono-exponential diffusion behavior has been shown to occur only at high b-values (> 2000 mm^2/s), which can be seen in the sensitivity plots as an increasing SC with b-value when evaluating α in the stretched-exponential model and D_s and f_s in the bi-exponential model (Figure 1.2.2). Due to the limited range of diffusion weighting, the high end of the diffusion curve is often under-sampled, as seen in the higher overall sensitivity of ADC, DDC, and D_f compared to other parameters in this range, and leading to elevated measurement error in those model parameters. This can be seen in Figure 1.2.2 with very high error in f_s and D_s compared to the stability of ADC, which even at SNR of 10 provides measurements with only 6% error. In fact, the bi-exponential model was found to be highly un-stable, with varying results depending on the initial parameter guess in the fitting algorithm. Introduction of a weighting factor based on SNR or higher b-values may help to stabilize bi-exponential results, but was not performed in this study. It is also generally found that an increase in the number of input parameters to a model increases the likelihood of non-negligible interactions among the parameters [43], which can be seen by the increasing measurement error of the "fast" diffusion coefficient with increasing number of input parameters at SNR of 100 (Figure 1.2.2D).

In conclusion, more complex models of the underlying diffusion mechanism may provide useful insight into the biological response to treatment. However, increasing model complexity may also be expected to result in an increase in the uncertainty of the optimization which introduces greater error into the measured parameters. For the purpose of detecting diffusion changes in living tissue, the traditional mono-exponential model appears to be the most stable while still providing the necessary sensitivity to detect small changes. Within this range of b-values, the bi-exponential model has insufficient data to be able to accurately measure the slow diffusion coefficient, and consequently has trouble separating D_s from D_f, resulting in very high error in f_s. Therefore, within the currently feasible range of diffusion weighting (i.e. b-values), the standard mono-exponential model provides the most robust readout as an imaging biomarker for therapeutic response assessment in tumors.

1.3: References

[1] Chenevert TL, McKeever PE, Ross BD. Monitoring early response of experimental brain tumors to therapy using diffusion magnetic resonance imaging. Clin Cancer Res 1997;3: 1457-66.

[2] Chenevert TL, Meyer CR, Moffat BA, Rehemtulla A, Mukherji SK, Gebarski SS, Quint DJ, Robertson PL, Lawrence TS, Junck L, Taylor JM, Johnson TD, Dong Q, Muraszko KM, Brunberg JA, Ross BD. Diffusion MRI: a new strategy for assessment of cancer therapeutic efficacy. Mol Imaging 2002;1: 336-43.
[3] Chenevert TL, Stegman LD, Taylor JM, Robertson PL, Greenberg HS, Rehemtulla A, Ross BD. Diffusion magnetic resonance imaging: an early surrogate marker of therapeutic efficacy in brain tumors. J Natl Cancer Inst 2000;92: 2029-36.
[4] Hall DE, Moffat BA, Stojanovska J, Johnson TD, Li Z, Hamstra DA, Rehemtulla A, Chenevert TL, Carter J, Pietronigro D, Ross BD. Therapeutic efficacy of DTI-015 using diffusion magnetic resonance imaging as an early surrogate marker. Clin Cancer Res 2004;10: 7852-9.
[5] Hamstra DA, Galban CJ, Meyer CR, Johnson TD, Sundgren PC, Tsien C, Lawrence TS, Junck L, Ross DJ, Rehemtulla A, Ross BD, Chenevert TL. Functional diffusion map as an early imaging biomarker for high-grade glioma: correlation with conventional radiologic response and overall survival. J Clin Oncol 2008;26: 3387-94.
[6] Mardor Y, Pfeffer R, Spiegelmann R, Roth Y, Maier SE, Nissim O, Berger R, Glicksman A, Baram J, Orenstein A, Cohen JS, Tichler T. Early detection of response to radiation therapy in patients with brain malignancies using conventional and high b-value diffusion-weighted magnetic resonance imaging. J Clin Oncol 2003;21: 1094-100.
[7] Moffat BA, Chenevert TL, Lawrence TS, Meyer CR, Johnson TD, Dong Q, Tsien C, Mukherji S, Quint DJ, Gebarski SS, Robertson PL, Junck LR, Rehemtulla A, Ross BD. Functional diffusion map: a noninvasive MRI biomarker for early stratification of clinical brain tumor response. Proc Natl Acad Sci U S A 2005;102: 5524-9.
[8] Ross BD, Moffat BA, Lawrence TS, Mukherji SK, Gebarski SS, Quint DJ, Johnson TD, Junck L, Robertson PL, Muraszko KM, Dong Q, Meyer CR, Bland PH, McConville P, Geng H, Rehemtulla A, Chenevert TL. Evaluation of cancer therapy using diffusion magnetic resonance imaging. Mol Cancer Ther 2003;2: 581-7.
[9] Moffat BA, Chen M, Kariaapper MS, Hamstra DA, Hall DE, Stojanovska J, Johnson TD, Blaivas M, Kumar M, Chenevert TL, Rehemtulla A, Ross BD. Inhibition of vascular endothelial growth factor (VEGF)-A causes a paradoxical increase in tumor blood flow and up-regulation of VEGF-D. Clin Cancer Res 2006;12: 1525-32.
[10] Byun WM, Shin SO, Chang Y, Lee SJ, Finsterbusch J, Frahm J. Diffusion-weighted MR imaging of metastatic disease of the spine: assessment of response to therapy. AJNR Am J Neuroradiol 2002;23: 906-12.
[11] Cui Y, Zhang XP, Sun YS, Tang L, Shen L. Apparent diffusion coefficient: potential imaging biomarker for prediction and early detection of response to chemotherapy in hepatic metastases. Radiology 2008;248: 894-900.
[12] Dudeck O, Zeile M, Pink D, Pech M, Tunn PU, Reichardt P, Ludwig WD, Hamm B. Diffusion-weighted magnetic resonance imaging allows monitoring of anticancer treatment effects in patients with soft-tissue sarcomas. J Magn Reson Imaging 2008;27: 1109-13.
[13] Harry VN, Semple SI, Gilbert FJ, Parkin DE. Diffusion-weighted magnetic resonance imaging in the early detection of response to chemoradiation in cervical cancer. Gynecol Oncol 2008;111: 213-20.
[14] Jacobs MA, Herskovits EH, Kim HS. Uterine fibroids: diffusion-weighted MR imaging for monitoring therapy with focused ultrasound surgery--preliminary study. Radiology 2005;236: 196-203.

[15] Pickles MD, Gibbs P, Lowry M, Turnbull LW. Diffusion changes precede size reduction in neoadjuvant treatment of breast cancer. Magn Reson Imaging 2006;24: 843-7.
[16] Seierstad T, Folkvord S, Roe K, Flatmark K, Skretting A, Olsen DR. Early changes in apparent diffusion coefficient predict the quantitative antitumoral activity of capecitabine, oxaliplatin, and irradiation in HT29 xenografts in athymic nude mice. Neoplasia 2007;9: 392-400.
[17] Ross BD CT, Kim B, Ben-Joseph O. Magnetic resonance imaging and spectroscopy: application to experimental neuro-oncology. Q Magn Reson Biol Med 1994;1: 89-106.
[18] Galons JP, Altbach MI, Paine-Murrieta GD, Taylor CW, Gillies RJ. Early increases in breast tumor xenograft water mobility in response to paclitaxel therapy detected by non-invasive diffusion magnetic resonance imaging. Neoplasia 1999;1: 113-7.
[19] Zhao M, Pipe JG, Bonnett J, Evelhoch JL. Early detection of treatment response by diffusion-weighted 1H-NMR spectroscopy in a murine tumour in vivo. Br J Cancer 1996;73: 61-4.
[20] Le Bihan D. Molecular diffusion, tissue microdynamics and microstructure. NMR Biomed 1995;8: 375-86.
[21] Le Bihan D. The 'wet mind': water and functional neuroimaging. Phys Med Biol 2007;52: R57-90.
[22] Lee KC, Moffat BA, Schott AF, Layman R, Ellingworth S, Juliar R, Khan AP, Helvie M, Meyer CR, Chenevert TL, Rehemtulla A, Ross BD. Prospective early response imaging biomarker for neoadjuvant breast cancer chemotherapy. Clin Cancer Res 2007;13: 443-50.
[23] Torigian DA, Huang SS, Houseni M, Alavi A. Functional imaging of cancer with emphasis on molecular techniques. CA Cancer J Clin 2007;57: 206-24.
[24] Le Bihan D, Turner R, Douek P. Is water diffusion restricted in human brain white matter? An echo-planar NMR imaging study. Neuroreport 1993;4: 887-90.
[25] Clark CA, Le Bihan D. Water diffusion compartmentation and anisotropy at high b values in the human brain. Magn Reson Med 2000;44: 852-9.
[26] Cohen Y, Assaf Y. High b-value q-space analyzed diffusion-weighted MRS and MRI in neuronal tissues - a technical review. NMR Biomed 2002;15: 516-42.
[27] Kiselev VG, Il'yasov KA. Is the "biexponential diffusion" biexponential? Magn Reson Med 2007;57: 464-9.
[28] Niendorf T, Dijkhuizen RM, Norris DG, van Lookeren Campagne M, Nicolay K. Biexponential diffusion attenuation in various states of brain tissue: implications for diffusion-weighted imaging. Magn Reson Med 1996;36: 847-57.
[29] Bennett KM, Schmainda KM, Bennett RT, Rowe DB, Lu H, Hyde JS. Characterization of continuously distributed cortical water diffusion rates with a stretched-exponential model. Magn Reson Med 2003;50: 727-34.
[30] Kwee TC, Galban CJ, Tsien C, Junck L, Sundgren PC, Ivancevic MK, Johnson TD, Meyer CR, Rehemtulla A, Ross BD, Chenevert TL. Comparison of apparent diffusion coefficients and distributed diffusion coefficients in high-grade gliomas. J Magn Reson Imaging 2010;31: 531-7.
[31] Kwee TC, Galban CJ, Tsien C, Junck L, Sundgren PC, Ivancevic MK, Johnson TD, Meyer CR, Rehemtulla A, Ross BD, Chenevert TL. Intravoxel water diffusion heterogeneity imaging of human high-grade gliomas. NMR Biomed 2010;23: 179-87.

[32] Roth Y, Tichler T, Kostenich G, Ruiz-Cabello J, Maier SE, Cohen JS, Orenstein A, Mardor Y. High-b-value diffusion-weighted MR imaging for pretreatment prediction and early monitoring of tumor response to therapy in mice. Radiology 2004;232: 685-92.
[33] Ross BD, Zhao YJ, Neal ER, Stegman LD, Ercolani M, Ben-Yoseph O, Chenevert TL. Contributions of cell kill and posttreatment tumor growth rates to the repopulation of intracerebral 9L tumors after chemotherapy: an MRI study. Proc Natl Acad Sci U S A 1998;95: 7012-7.
[34] Moffat BA, Hall DE, Stojanovska J, McConville PJ, Moody JB, Chenevert TL, Rehemtulla A, Ross BD. Diffusion imaging for evaluation of tumor therapies in preclinical animal models. MAGMA 2004;17: 249-59.
[35] Laubach HJ, Jakob PM, Loevblad KO, Baird AE, Bovo MP, Edelman RR, Warach S. A phantom for diffusion-weighted imaging of acute stroke. J Magn Reson Imaging 1998;8: 1349-54.
[36] Hall MG, Barrick TR. From diffusion-weighted MRI to anomalous diffusion imaging. Magn Reson Med 2008;59: 447-55.
[37] Chenevert TL, Sundgren PC, Ross BD. Diffusion imaging: insight to cell status and cytoarchitecture. Neuroimaging Clin N Am 2006;16: 619-32, viii-ix.
[38] Hamstra DA, Rehemtulla A, Ross BD. Diffusion magnetic resonance imaging: a biomarker for treatment response in oncology. J Clin Oncol 2007;25: 4104-9.
[39] Lee KC, Bradley DA, Hussain M, Meyer CR, Chenevert TL, Jacobson JA, Johnson TD, Galban CJ, Rehemtulla A, Pienta KJ, Ross BD. A feasibility study evaluating the functional diffusion map as a predictive imaging biomarker for detection of treatment response in a patient with metastatic prostate cancer to the bone. Neoplasia 2007;9: 1003-11.
[40] Padhani AR, Liu G, Koh DM, Chenevert TL, Thoeny HC, Takahara T, Dzik-Jurasz A, Ross BD, Van Cauteren M, Collins D, Hammoud DA, Rustin GJ, Taouli B, Choyke PL. Diffusion-weighted magnetic resonance imaging as a cancer biomarker: consensus and recommendations. Neoplasia 2009;11: 102-25.
[41] Schwarcz A, Bogner P, Meric P, Correze JL, Berente Z, Pal J, Gallyas F, Doczi T, Gillet B, Beloeil JC. The existence of biexponential signal decay in magnetic resonance diffusion-weighted imaging appears to be independent of compartmentalization. Magn Reson Med 2004;51: 278-85.
[42] Hoff BA, Chenevert TL, Bhojani MS, Kwee TC, Rehemtulla A, Le Bihan D, Ross BD, Galban CJ. Assessment of multiexponential diffusion features as MRI cancer therapy response metrics. Magn Reson Med 2010;64: 1499-509.
[43] Saltelli A, Chan K, Scott EM. Sensitivity analysis. Chichester ; New York: Wiley; 2000.
[44] Gudbjartsson H, Patz S. The Rician distribution of noisy MRI data. Magn Reson Med 1995;34: 910-4.

Chapter 2: **Permeability (DCE)-MRI**

2.1: Permeability-MRI Treatment Response to VEGF Blockade

Hoff BA, Bhojani MS, Rudge J, Chenevert TL, Meyer CR, Galbán S, Johnson TD, Leopold JS, Rehemtulla A, Ross BD, Galbán CJ. DCE and DW-MRI monitoring of vascular disruption following VEGF-Trap treatment of a rat glioma model. NMR Biomed. 2012 Jul;25(7):935-42.

2.1.1: Introduction

In Phase III clinical testing, Stupp and colleagues demonstrated the efficacy of concurrent temozolomide and radiation for treating newly diagnosed glioblastoma [1]. With an improvement of median survival from 12 months to 14 months, this treatment regimen has become the standard of care. Although radiotherapy plus concomitant temozolomide provides a clinically meaningful and significant survival benefit, the prognosis remains poor for most patients with malignant gliomas. A number of molecularly targeted therapies are being investigated for their potential to significantly improve the outcome for these patients [2, 3].

Anti-angiogenic and antivascular therapies are at the forefront of development as viable treatment options for solid tumors [4, 5]. Recent clinical trials have shown that such agents, e.g. Bevacizumab, provide improved efficacy for the treatment of recurrent brain tumors [6]. The requirement of malignant gliomas for a continual supply of nutrients and oxygen provided by a vast network of newly forming intratumoral vessels provides a sound scientific rationale for targeting tumor angiogenesis. Vascular Endothelial Growth Factor (VEGF) is one of the principal driving forces for tumors to maintain their highly proliferative potential. Elevated stimulation of angiogenesis through the production of VEGF occurs predominantly in high-grade tumors [7]. Recent studies have also shown a significant reduction in both vascular permeability and neovascular formation in tumors treated with VEGF inhibitors [8-14] and have shown tumor regression in some cases [15]. VEGF-Trap (Regeneron Pharmaceuticals, Inc., Tarrytown, NY),

currently in clinical trials, is a decoy receptor protein effective in inhibiting VEGF signaling by binding with a high affinity to all isoforms of VEGF-A and placental growth factor [9-11, 15-20]. Preclinical studies have shown that this agent, when combined with standard treatments encompassing chemotherapy as well as radiotherapy, results in improved efficacy [21-23]. Ultimately, these treatments are aimed at indirectly inhibiting tumor growth and possibly inducing cell death by limiting the availability of vital nutrients, which may improve the effectiveness of conventional therapies [21, 22].

Efforts are being made to evaluate imaging modalities to provide biomarkers of therapeutic-induced alterations in the tumor vasculature. Monitoring of volumetric changes prior to and following treatment initiation is the current standard of practice for assessing treatment effects. Although effective in predicting clinical outcome to therapy, prognosis may take 2–3 months following the start of treatment. Functional imaging complements traditional anatomical imaging for improved diagnosis and response assessment. Hemodynamic imaging techniques including dynamic contrast enhanced (DCE) and dynamic susceptibility contrast (DSC) MRI provide insights into tumor blood flow, blood volume and vessel permeability, which have shown promise as sensitive biomarkers of treatment-induced response [23]. Most notably, DCE-MRI uses low contrast agent concentrations to produce signal enhancement, which can be tracked and fit to a pharmacokinetic model to extract such values as volume transfer constant (K^{trans}), the flux rate constant between the extravascular extracellular space and plasma (k_{ep}), and blood plasma volume fraction (v_p) [24-26]. DCE-MRI has been used successfully to show decreased K^{trans} in tumors very early after anti-VEGF treatments [8, 12, 13]. A decrease in K^{trans} has been correlated with decreased growth rates and decreased levels of free VEGF, indicating effective drug targeting. The apparent diffusion coefficient (ADC), a quantitative measure of water mobility calculated from diffusion weighted (DW) MRI, has shown promise as a sensitive and reliable biomarker for cytotoxic therapies [27-30] that elicits a treatment-induced reduction in tumor cellularity [31]. Increased cell death has been correlated with an increase in ADC. In this study, DCE- and DW-MRI were used to evaluate cellular and hemodynamic response of 9L rat brain tumors to a VEGF-Trap antibody regimen.

2.1.2: Methods

Animal tumor models

9L glioma cells were obtained from the Brain Tumor Research Center at the University of California at San Francisco. The cells were grown as monolayers in 10 cm^2 sterile plastic flasks in Dulbecco's Modified Eagle Medium with 10% fetal bovine serum, 100 IU/mL penicillin and 100 mg/mL streptomycin, and 2 mM L-glutamine in a 37°C incubator. Prior to implantation, cells were harvested by trypsinization, counted, and re-suspended in serum-free medium for injection.

Tumor implantation was performed in 17 male Fischer-344 rats, 7 to 9 weeks old (Harlan Sprague–Dawley, Indianapolis, IN) weighing between 125 and 150 g. Briefly, animals were anesthetized with a ketamine/xylazine mixture (87/13 mg/kg) administered intraperitoneally. A small incision was made over the right hemisphere of the cranium. A 1-mm diameter burr hole was drilled through the skull using a high-speed surgical drill, and a 5-mL suspension containing $2x10^5$ 9L cells was slowly injected at a depth of 3 mm. The burr hole was filled with bone wax, and the surgical area was cleaned using 70% ethanol. Vetbond® (3 M, St. Paul, MN) was used to close the incision until healed.

Anti-angiogenic therapy

Once tumor volumes reached 20–60 mm^3 as determined using MRI, pre-treatment DCE and DW-MR images were acquired for all animals. Animals were then separated into two groups and were treated with either 25 mg/kg VEGF-Trap (n = 10) or 12.5 mg/kg human Fc (vehicle protein) (n = 7). Treatments were administered subcutaneously twice weekly for two weeks (Figure 2.1.1A).

MRI scans

MRI scans were performed on a 9.4 T, 16 cm horizontal bore Varian (Palo Alto, CA) DirectDrive system with a quadrature rat head coil (Doty Scientific, Inc., Columbia, SC). During all MRI procedures, animals were anesthetized with a 1–2% isofluorane/air mixture and body temperature was maintained using a heated air system (Air-Therm, World Precision Instruments, Sarasota, FL). MR images were acquired 24 h prior to treatment initiation and 24 h after each treatment (Figure 2.1.1A). Each MR experiment consisted of a fast spin-echo-based T_1-mapping

sequence and DCE- and DW-MRI sequences with a total overall acquisition time for each imaging session of approximately 45 min.

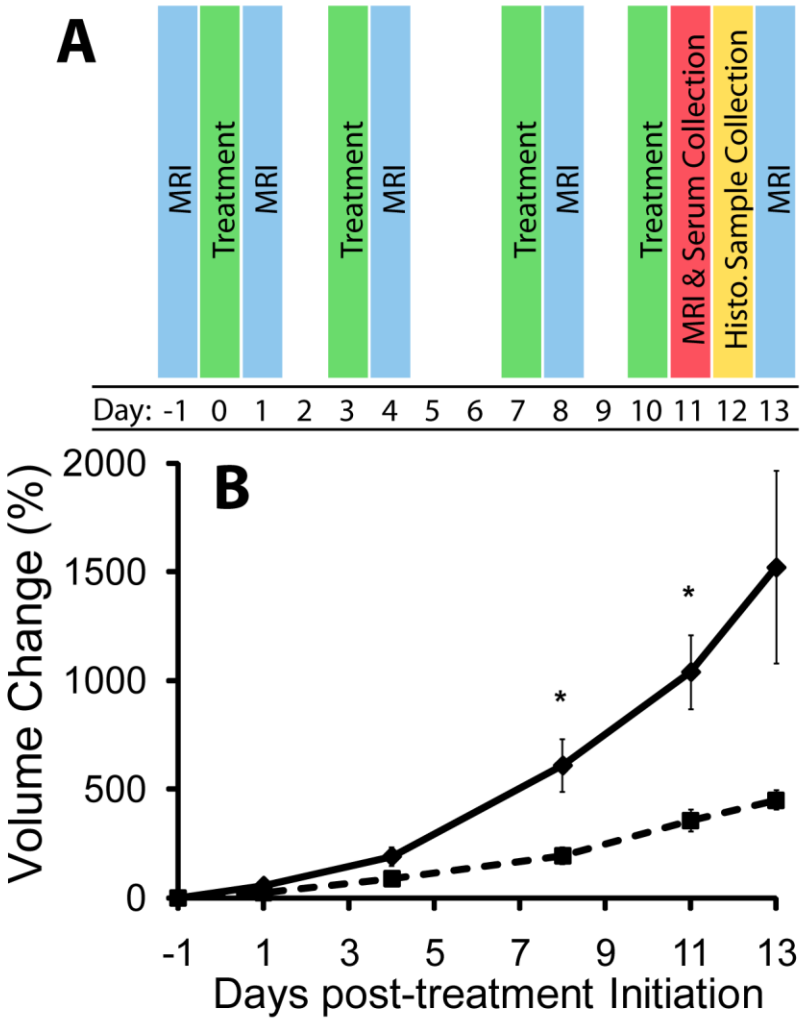

Figure 2.1.1: Diagrammatic presentation of study time points (A). Treatments are highlighted in green, MRI (both DCE and DWI) are highlighted blue, MRI and blood serum collection were performed on Day 11 (red), and histological samples were taken at approximately Day 12 (yellow). Plot showing relative change in tumor volume in control (diamond, solid line) and treated (square, dotted line) groups over the study time period (B). Treated animals generally showed a significant slowing of tumor growth compared to controls. Doubling times in the control and treated groups were 3.76 (± 0.325) and 5.32 (± 0.319) days, respectively ($p = 0.004$). Significance in relative change in volume between groups occurred at days 8 and 11 post-therapy. Data are presented as means ± SEM. Significance was assessed at $p<0.05$ and indicated by *.

DW-MRI was performed using a spin-echo sequence with a navigator echo for motion correction and gradient waveforms sensitive to isotropic diffusion [32]. Images were acquired using the following parameters: repetition time/echo time (TR/TE) = 4000/47 ms, field of view (FOV) = 30 mm, matrix size = 128 x 64, slice thickness = 1 mm, slice number = 13, and b-values (diffusion weighting) of 120 and 1200 s/mm^2.

DCE-MRI was performed using a T_1-weighted gradient-echo sequence with the following parameters: TR/TE = 85/3.2 ms, flip angle = 20°, FOV = 30 mm, matrix size = 128 x 64, slice thickness = 1 mm, slice number = 13 and averages = 2. Image datasets were acquired over a 15-min period with a time resolution of 10.9 s. Following 1 min of scanning (~6 images), a bolus dose of gadolinium-DTPA (Magnevist, Bayer Healthcare Pharmaceuticals; 0.15 mmol/kg, diluted 1:8.3 from 0.5 mmol/mL in 0.9% saline solution to 0.06 mmol/ml) was administered via tail-vein catheter at a rate of 4 mL/min.

Image reconstruction and analysis

Tumors were manually contoured on the low-b images from the DW-MRI sequence (b = 120 s/mm^2). These volumes of interest (VOI) were used to determine tumor volume and whole-tumor mean values generated from quantification of DW-MRI and DCE-MRI data. Tumor doubling times were calculated for each animal from exponential fits in Excel (Microsoft, Redmond, WA) to each individual growth time course [33].

Apparent diffusion coefficients were calculated from the two diffusion weightings (b-values) using the following equation:

$$ADC_{1-2} = {ln\left(\frac{S_1}{S_2}\right)}/{(b_2 - b_1)}, \qquad [2.1.1]$$

where S_1 and S_2 are the signal intensities at b-values b_1 = 120 s/mm^2 and b_2 = 1200 s/mm^2, respectively, and ADC_{1-2} is the apparent diffusion coefficient obtained using b_1 and b_2.

Tumor kinetic parameters were determined by a voxel-wise three-parameter fit on the acquired time-resolved T_1-weighted images using a tri-exponential arterial input function (AIF) for blood plasma concentration (C_p) (12):

$$C_p(t) = A_1 e^{(-\alpha_1 t)} + A_2 e^{(-\alpha_2 t)} + A_3 e^{(-\alpha_3 t)}, \qquad [2.1.2]$$

with A_1 = 0.8259, A_2 = 0.2230, A_3 = 0.1565 mM, α_1 = 1.220, α_2 = 0.156, and α_3 = 0.017 min^{-1}. In this study, we followed the referenced contrast injection procedure used for this AIF and

assumed negligible differences in AIF over time as well as between animals. This AIF was incorporated into a generalized kinetic model, equivalent to the efflux-corrected Patlak model [34, 35]:

$$C_t(t) = K^{trans} \int_0^t C_p(t) e^{\left(-k_{ep}(t-\tau)\right)} d\tau + v_p C_p(t), \quad [2.1.3]$$

where K^{trans} is the volume transfer constant, k_{ep} is the flux rate constant between extravascular extracellular space (EES) and plasma, and v_p is the blood plasma volume fraction. Fits were performed using an un-weighted non-linear least-squares algorithm with an initial parameter guess based on literature values, and goodness-of-fit (GoF) was monitored to confirm reliable results; GoF was defined as the normalized root mean square error. Baseline signal intensity was calculated as a mean from the first ~6 images before contrast injection excluding the first image due to non-steady-state signal. Tissue concentrations of contrast agent were determined using the following equation: $1/T_1 = R*[\text{Gd-DTPA}]+ 1/T_{10}$. The relaxivity (R) was determined to be 5.5 ml/(mmol·s) by acquiring T_1 maps of 1 cm^3 syringes filled with saline (0.5 M) and 13 Gd-DTPA concentrations ranging from 0 to 10 mM. The relaxation constant was assumed constant between animals and time points. T_{10} is the T_1 of the tumor tissue prior to injection of contrast agent. T_{10} was set to 2.5 s which was the average of T_1 measurements obtained in each animal pre-therapy using a fast spin-echo sequence with the following parameters: five TR values of 5, 1.5, 1, 0.8 and 0.6 s, with 1, 1, 1, 2, and 4 averages, respectively; effective echo time (TE)= 39.68 ms, echo train length (ETL) = 4, 2 dummy scans, matrix size= 128 x 256, FOV = 3 cm, slice thickness = 1mm. Parameter maps of K^{trans}, k_{ep}, v_p, and GoF were saved for the tumor VOI. Non-enhancing tumor tissue within the VOI was excluded from the analysis due to the model's inability to accurately describe the tissue's kinetic properties. Therefore, voxels with lower than 0.35 GoF or 0.002 v_p were excluded in mean tumor measurements. All reconstruction and analyses were performed using in-house programs written in MATLAB (The Mathworks, Natick, MA, USA). Parameter maps shown in Figure 2.1.2 were interpolated to 256 x 256 matrix size for display only.

Histology

Three representative animals were randomly selected from each group for tumor histology at approximately 12 days post-treatment initiation (Figure 2.1.1A). 9L tumors from control and treated animals were placed in buffered formalin overnight, dehydrated in 70%

ethanol, and subsequently embedded in paraffin. Tissue sections were prepared for histological processing by routine techniques. Briefly, paraffin sections (5 mm thick) were cut on a microtome and heated for 20 min at 65°C. Slides were de-paraffinized in xylene with three changes for 5min each, then rehydrated through an alcohol gradient for 2min each (100%alcohol, 95%alcohol, 70% alcohol). Some sections were first stained using a Gill's 2X hematoxylin solution followed by eosin, while others were stained using the rabbit polyclonal antibody to Von Willebrand Factor III (vWf) to highlight tissue vasculature, and counterstained for the nuclei. For counting tumor vasculature, representative fields were obtained from the vWf-stained slides at random on each of three controls and three treated tumor slices. Brown-stained areas greater than about 10 mm in diameter were considered positive stains for the purpose of counting. Positive stains were counted using ImageJ software (NIH) and used to quantify the difference between groups. On additional sections, ApopTag or Ki-67 stains were performed using standard techniques to highlight apoptotic or proliferating cells in the tumor, respectively.

Assessment of free and bound VEGF

Blood serum samples were collected through a tail-vein catheter 24 h after the final dose of VEGF-Trap (n = 7) or vehicle (n = 3) (Figure 2.1.1A). Samples were stored short-term in a 3°C refrigerator until being shipped on ice to Regeneron Pharmaceuticals for analysis.

Free VEGF trap was measured using a sandwich ELISA method in which hVEGF165 (Regeneron Pharmaceuticals, Inc.) diluted in 0.05 M carbonate-bicarbonate buffer was used as the capture protein at a concentration of 2 μg/mL. The antigen was VEGF-Trap (Regeneron Pharmaceuticals, Inc.) prepared in 1% BSA (KP Labs). Samples and standard were incubated for 2 h at room temperature and the excess was removed in subsequent washes. The bound material was then reported with a mouse monoclonal antibody (P10 G1F6, Regeneron Pharmaceuticals, Inc.) then a secondary antibody was used. Anti-mouse HRP (Jackson Laboratories) TMB substrate (Sigma, T8665) was used in the color development, the plates were read at 450–570 nm and results analyzed using the SoftMax Pro 5.3 (Molecular Devices).

Bound endogenous rat VEGF was determined by an ELISA developed using the antibody to Rat VEGF164 affinity purified polyclonal antibody (R&D Systems, Cat#AF564) as the capture antibody. The antigen was prepared fresh with rVEGF bound to two molar quantities of the VEGF-Trap and allowed to incubate at room temperature for 1 h. This complex was used to

generate a standard curve. Samples were bound to the plate, and after washing away the unbound rVEGF the unknown and controls were reported with an anti-human Fc IgG (Sigma, A-0170). The captured protein used in this assay was recombinant rat VEGF at 2 mg/mL in 0.05 M carbonate-bicarbonate buffer. The antigen used was the mouse monoclonal antibody P10 (Regeneron Pharmaceuticals, Inc.), which was reported using a goat anti-mouse antibody (Jackson Laboratories) and the samples were reported with an anti-rat antibody (Promega). The samples were diluted 1:1000 to dilute out the serum effects of this assay.

Statistics

A paired Student's t-test was used to compare the percent change of parameter values between pre- and post-therapy time points for each animal. An unpaired Student's t-test was used to perform group comparisons in percent change of parameter values at each time point and tumor doubling times. Results were declared statistically significant at the two-sided 5% comparison-wise significance level ($p<0.05$). Values are given as means ± SEM.

2.1.3: Results

Therapeutic intervention was initiated at tumor volumes of 35.8 ± 5.0 mm^3 and 36.4 ± 8.6 mm^3 for VEGF-Trap therapy and vehicle-treated control animals, respectively. Based on ELISA analyses, VEGF-Trap proved effective at binding to virtually all endogenous VEGF with no detectable VEGF and excess VEGF-Trap within the blood samples tested (Table 2.1). Data for the control group were not presented due to the absence of VEGF-Trap and VEGF levels being below quantification. Low levels of endogenous VEGF in non-VEGF-Trap treated animals have been reported in previous studies [20, 36]. As shown in Figure 2.1.1B, inhibition of VEGF signaling within the tumor resulted in significantly larger percentage changes in control tumor volumes at 8 and 11 days post-treatment initiation than those observed for VEGF-Trap treated tumors ($p<0.05$). Tumor volume doubling times were also affected as evidenced by values of 3.76 (± 0.325) and 5.32 (± 0.319) days for vehicle and VEGF-Trap groups, respectively ($p = 0.004$).

Table 2.1: ELISA analysis of endogenous VEGF.

	Free VEGF-Trap	Bound VEGF	Free Rat VEGF
VEGF-Trap	98660 ± 11529	1540.45 ± 149.30	0.00 ± 0.00
BLQ	359	309	783

Note: ELISA analysis was performed to assess the effectiveness of VEGF-Trap in attenuating the signalling of free rat VEGF. Blood serum levels were measured on day 11, after the last treatment. Free VEGF-Trap refers to unbound VEGF-Trap, Bound VEGF refers to VEGF/VEGF-Trap complex, Free Rat VEGF refers to unbound endogenous VEGF, and BLQ indicates Below Level of Quantification. Quantities are shown as group mean ± standard error (n=7). All units are ng/mL. VEGF levels for control animals were unmeasureable and are not shown.

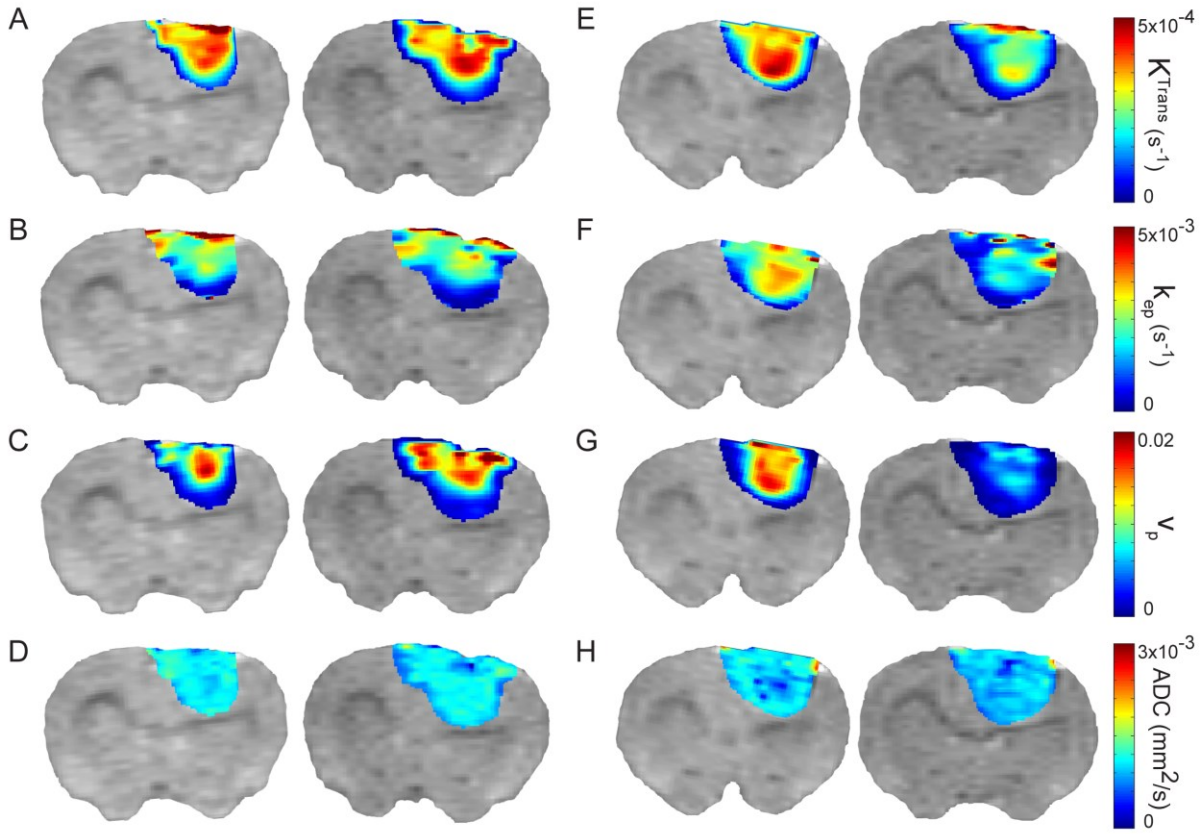

Figure 2.1.2: T2-weighted images with color overlays of parametric maps are shown for a representative animal in the control group (A–D) and the VEGF-Trap-treated group (E–H) prior-to (Day -1, left image) and following (Day 1, right image) the initial treatment. The initial drop for the VEGF-Trap-treated group in K^{trans} (-27%), k_{ep} (-12%), and v_p (-64%) can clearly be seen here (E–G). ADC shows a small, but significant drop (-7%) by the first day post-therapy (H). Tumor heterogeneity was observed at individual time points. Nevertheless response to VEGF-Trap did not vary spatially throughout the tumor.

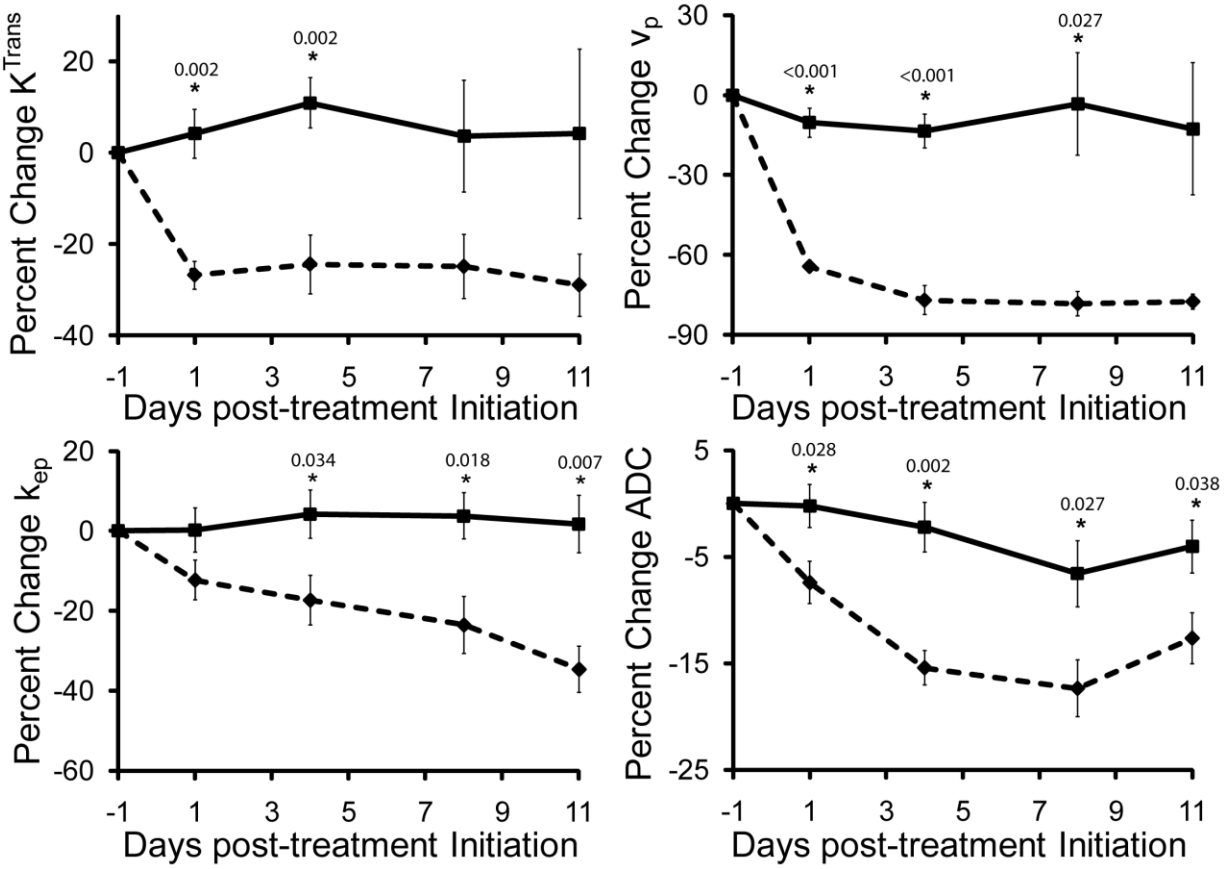

Figure 2.1.3: Plots of relative change in kinetic and diffusion parameters for the treated group (diamond, dotted line) shown together with the control (square, solid line). A significant decrease in K^{trans} and v_p occurred on the first day post-therapy and persisted throughout the study. Tumor ADC steadily decreased in VEGF-Trap treated tumors up to 15% from the initial value. In contrast, k_{ep} continued to decrease throughout the study. Data are presented as means ± SEM. Significance was assessed at $p<0.05$ and indicated by * under their respective p-values. Baseline parameter values for vehicle and VEGF-Trap treated animals are: for K^{trans}, 2.4±0.1 ($x10^{-4}$) /s and 2.3±0.1 ($x10^{-4}$) /s (p=0.7), respectively; v_p, 7.6±1.3 ($x10^{-3}$) and 8.1±0.5 ($x10^{-3}$) (p=0.7), respectively; k_{ep}, 1.9±0.1 ($x10^{-3}$) and 1.9±0.1 ($x10^{-3}$) (p=0.8), respectively; and ADC, 1.1±0.02 ($x10^{-3}$) mm^2/s and 1.0±0.02 ($x10^{-3}$) mm^2/s (p = 0.1), respectively.

Representative vascular kinetic and diffusion parameter maps are shown as color overlays in Figure 2.1.2. Partial-volume effects are apparent in Figure 2.1.2, evidenced by reduced kinetic measurements on the periphery of the color overlays. In vehicle-treated animals, negligible changes in parameter values were observed one day post-treatment initiation compared to the pre-treatment baseline (Figure 2.1.2A–D). In striking contrast, a single treatment with VEGF-Trap resulted in a substantial decrease in all kinetic parameters (Figure 2.1.2E–H) consistent with successful drug targeting. In general, all kinetic parameters showed spatial

variability within the 9L tumors at any given time point. Nevertheless, a spatially uniform response to VEGF-Trap was observed throughout the tumor for all kinetic metrics.

The two kinetic transfer constants, K^{trans} and k_{ep}, and blood volume fraction (v_p) were found to be dependent on VEGF-Trap treatment, again consistent with strong effectiveness in target modulation by the drug (Figure 2.1.3). The reduction in K^{trans} was observed following the first day of treatment, with a significant difference in K^{trans} (27 ± 3.1%, p = 0.002) when compared to vehicle-treated animals. Similar trends were observed for v_p with a change of 63 ± 2.3% ($p<0.001$). Subsequent to the initial decrease, parameter values plateaued and remained stable throughout the rest of the treatment cycle. A gradual reduction in k_{ep} resulted in significant differences between the two treatment groups by Day 3 post-treatment initiation (Figure 2.1.3). The maximum change in k_{ep} (34.6 ± 5.8%, p = 0.007) was observed at Day 11.

In line with the kinetic parameters, ADC values declined following VEGF-Trap treatment (Figure 2.1.3). Although not as pronounced as the changes in kinetic metrics, a significant reduction in the change in ADC values was observed in VEGF-Trap treated tumors when compared to controls for all time points after treatment. ADC values did not reach a minimum value until Day 8 with a percentage decrease of 17.8 ± 3.2% (p = 0.027). Although ADC values for VEGF-Trap animals increased slightly from Day 8 to 11, this change was not significant.

Histological sections of representative animals from control (n = 3) and treated (n = 3) groups taken 24 hours after the last treatment (11 days post-initial-treatment) were subjected to H&E, Ki-67, Von Willebrand / Factor VIII (vWF) and ApopTag staining. As observed in Figure 2.1.4, a 14% reduction in Ki-67 staining was observed for VEGF-Trap treated tumors. This difference, although consistent with reduced proliferative potential, was not significant (p = 0.25). In contrast, vWF stained sections revealed that vessel numbers were significantly lower in VEGF-Trap-treated versus vehicle-treated animals (p = 0.011; Figure 2.1.5). Interestingly, ApopTag staining revealed that apoptosis appeared to be localized within the endothelial cells of the vasculature, as shown by heavily stained regions in Figure 2.1.6. In contrast, tumor tissue did not show significant staining, and was therefore not quantified and compared between groups. The results observed in Figure 2.1.6 are consistent with the loss in vessel number (Figure 2.1.5) as well the reduction in MRI-determined kinetic measures (Figure 2.1.3). However, loss of vasculature due to VEGF inhibition did not result in a reduction in tumor cellularity as depicted

by visual inspection of tumor nuclear staining as well as lack of significant ApopTag staining in the tumor (Figure 2.1.6).

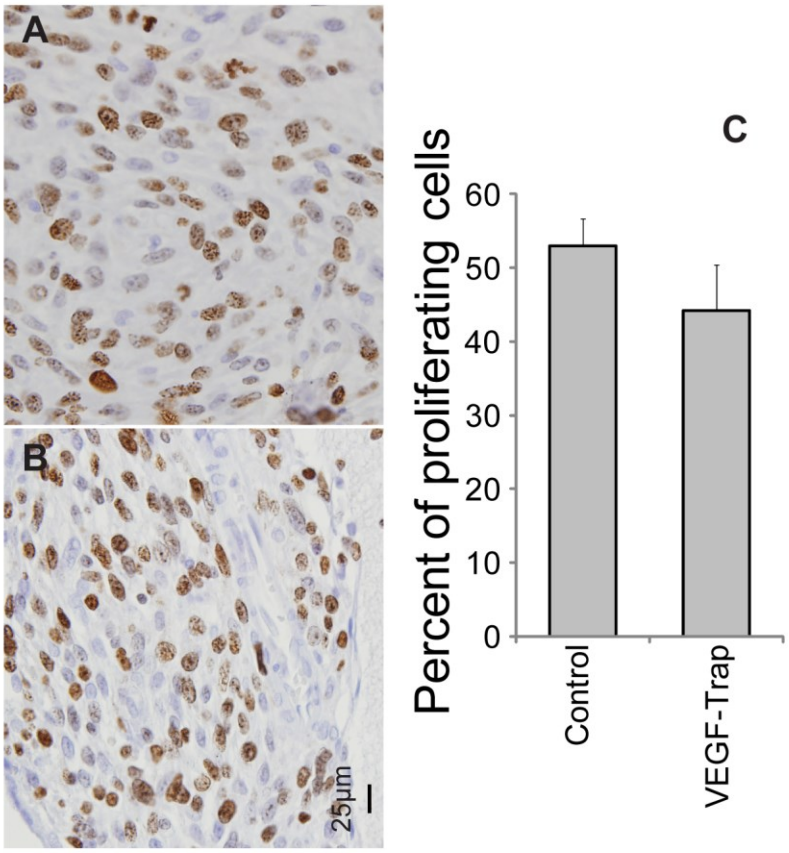

Figure 2.1.4: The proliferative potential of tumors following treatment with vehicle (A) or VEGF-Trap (B) was determined by Ki-67 staining of samples taken on Day 12. Positively identified nuclei were counted in randomly selected fields. Representative micrographs for each group are shown. The quantification of the nuclei for each treatment group in 3–6 randomly selected fields per subject (C). Insignificant differences in Ki-67 positive nuclei were observed between treatment groups ($p = 0.25$). Bar plots are presented as the mean number of nuclei and SEM. Images were acquired at 40x magnification.

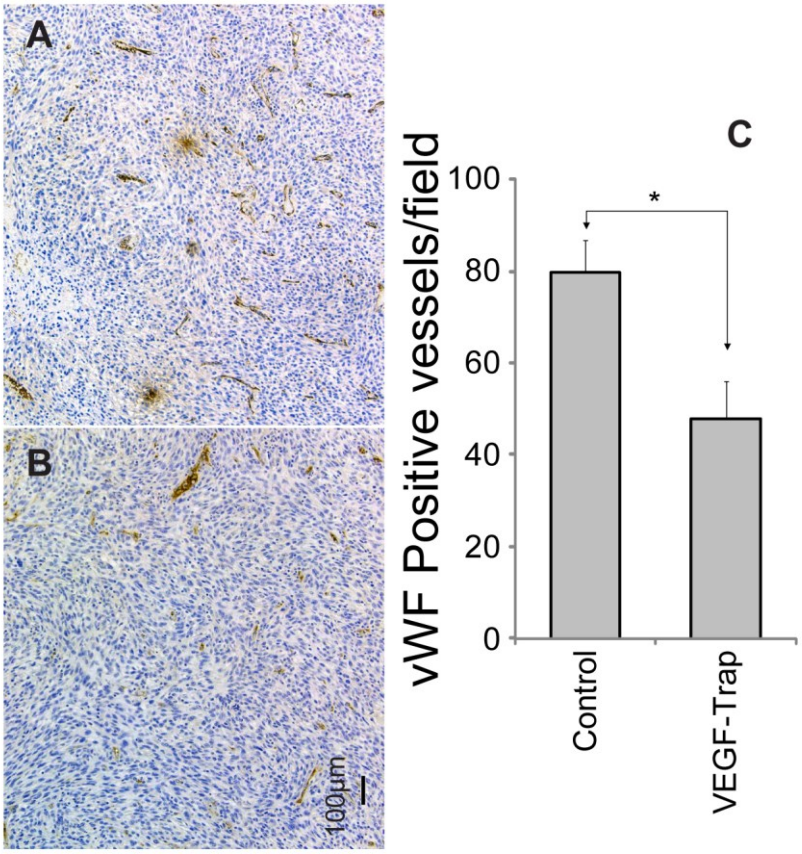

Figure 2.1.5: Tumor vasculature following treatment with vehicle (A) or VEGF-Trap (B) was determined by Von Willebrand factor staining of samples taken on Day 12. Positively stained vessels were counted in randomly selected fields. Representative micrographs for each group are shown. The quantification of the vessels for each treatment group in 2–3 randomly selected fields per subject (C). A significant decrease in the number of vessels occurred in VEGF-Trap treated animals ($p = 0.011$). Bar plots are presented as the mean number of nuclei and SEM. Images were acquired at 10x magnification.

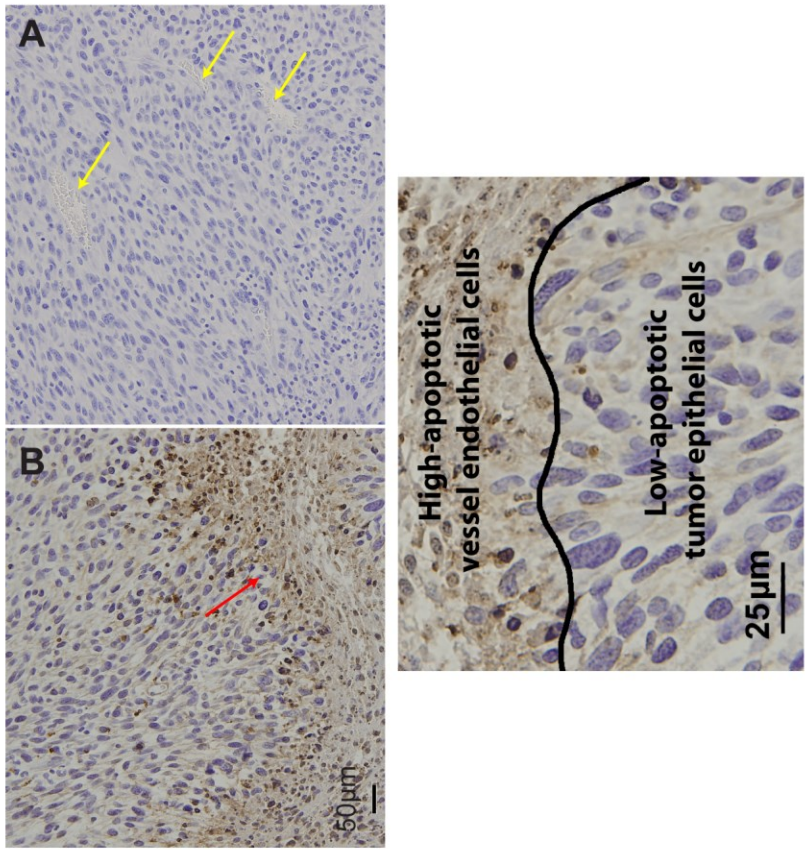

Figure 2.1.6: Apoptosis and tumor cellularity following treatment with vehicle (A) or VEGF-Trap (B) was determined by ApopTag staining of samples taken on Day 12, superimposed on H&E. Extent of apoptosis and tumor cellularity were assessed by visual inspection. Representative micrographs for each group are shown. Treatment by VEGF-Trap resulted in massive apoptotic events in the tumor vasculature but negligible change in tumor cellularity when compared to vehicle-treated tumors. Healthy and apoptotic vessels are indicated by yellow and red arrows, respectively. A closer representative VEGF-Trap treated sample is shown in C, highlighting the border between tumor epithelial and vessel endothelial cells. Images were acquired at 20x (A&B) or 40x (C) magnification.

2.1.4: Discussion

The development of molecular targeted cancer therapies represents an area of intense investigation. Consequently, a number of clinical trials are underway encompassing a diverse array of targets and agents. However, the primary endpoint used for assessing therapeutic response continues to be gross tumor volumetric change. This endpoint may not be the best choice for measuring the effectiveness of those molecularly targeted agents that do not uniformly elicit a significant reduction in tumor volume [37-39]. Therefore, there is an impetus to explore

non-invasive quantitative imaging modalities, such as MRI and positron emission tomography (PET), for their potential to provide non-invasive biomarkers of treatment response. In fact, DCE-MRI and DW-MRI metrics have shown significant promise as biomarkers of early cancer therapeutic response [40, 41]. The goal of this study was to evaluate DCE-MRI and DW-MRI for their ability to detect and quantify the therapeutic response of glioma-bearing animals treated with VEGF-Trap.

VEGF-Trap is extremely effective in binding VEGF and PGF [15, 18]. The extent of VEGF-Trap binding to endogenous VEGF was virtually complete following two weeks of treatment (Table 2.1). This strong binding affinity to endogenous VEGF was clearly evident early in our MRI measurements. Vascular kinetic rates and blood plasma volume fraction as measured by DCE-MRI were highly sensitive to VEGF-Trap treatment. Subsequent to the first treatment, both K^{trans} and v_p diminished by approximately 30% and 60%, respectively, suggesting an extremely rapid response of tumor vasculature to VEGF-Trap. These vascular changes are reflected in our vWF and ApopTag histological stains (Figs 5 and 6), which show a lower number of vWF-positive-stained blood vessels and greater ApopTag staining of vessel endothelial cells in treated animals. These trends agree with those observed in both preclinical and clinical investigations of tumor response to anti-angiogenic and antivascular agents as measured by DCE-MRI [8, 41].

An increase in tumor water mobility as determined by ADC measurements has been associated with a reduction of tumor cellularity as a consequence of massive cell kill [27]. Treatment by VEGF-Trap elicited no such response in ADC values, suggesting no substantial decrease in tumor cellularity due to cell death. Staining by H&E and ApopTag corroborated what was observed by ADC. In fact, ADC values decreased significantly following VEGF-Trap treatment with a significant drop observed as early as one day post-treatment. Reiger and colleagues monitored changes in DSC-MRI and DW-MRI quantitative metrics during Bevacizumab treatment in glioma patients, observing a similar trend in ADC [41]. In their clinical study, a drop in tumor blood volume as well as water mobility within the tumor was reported by 8 weeks post-treatment initiation. The reduction of ADC was attributed to pathological changes in the tumor, which may result in a decrease in extracellular water content and narrowing of extracellular space due to treatment-induced hypoxia. This would result in an increase in tumor cellularity per unit volume, which is inversely related to ADC values.

Numerous models for assessing pharmacokinetic qualities *in vivo* with varying assumptions have been proposed. In this study we used an established model that assumes the fast exchange limit to analyze our DCE-MRI data. This technique has been well-documented but recent studies have provided more robust models including the shutter-speed approach developed by Yankeelov and colleagues in 2003 [35]. This model has shown greater accuracy in quantifying permeability kinetics but has only recently seen more extensive application. Although more accurate, the sensitivity of the newer models to therapeutic response have yet to be tested against established pharmacokinetic models. Such an analysis is beyond the scope of this study.

The impairment of VEGF signaling activity in the 9L glioma model resulted in apoptosis of the vascular endothelial cell population, which likely contributed to the overall reduction in tumor vessel numbers. The observed decrease in tumor vessel density is also in agreement with previously reported results of the use of antivascular agents on gliomas [42-45]. However, in these previous studies, apoptosis of endothelial cells was not reported following VEGF-Trap treatment. Erber and colleagues showed that targeting VEGFR-2 and PDGFR-b signaling using the tyrosine kinase inhibitor SU6668 in a C6 rat tumor model resulted in endothelial cell apoptosis and reduced tumor growth rate [46]. This is in agreement with our results, which show a similar reduced growth rate as reflected in our volume measurements as well as Ki-67 staining (Figure 2.1.1B and Figure 2.1.4) that show a slightly diminished fraction of proliferating cells.

In conclusion, this study supports the utility of DCE- and DW-MRI in monitoring the effectiveness of angiogenesis-targeted cancer therapy, in this case response to VEGF-Trap. The ability to track therapeutic effectiveness with non-invasive imaging biomarkers is especially important for gliomas because biopsies during the course of treatment are not an option (unlike most other histotypes that are amenable to pharmacodynamic biomarkers). The use of these MRI modalities is especially compelling as angiogenesis targets are prominently being tested in the glioma population. Besides Aflibercept (VEGF-Trap), there are a number of other targeted agents in current clinical trials for treating glioma patients, e.g. Zactima (vandetanib, ClinicalTrials. gov ID: NCT00272350), cediranib (AZD2171) [34], ramucirumab (ClinicalTrials.gov ID: NCT00895180), BIBF1120 (ClinicalTrials.gov ID: NCT01380782), as well as numerous bevacizumab (Avastin; ClinicalTrials.gov ID: NCT00782756) [47-49] combination trials. Studies are underway to extend this proof-of-principle to the study of the

broader angiogenesis portfolio to build a compelling case for clinical trial incorporation. Overall, MRI biomarkers have significant potential for not only monitoring treatment effects but also for optimization of drug dose and schedules.

2.1.5: Acknowledgements

This work was supported by the National Institutes of Health Research Grants P01CA85878 and P50CA93990. VEGF-Trap was kindly provided by Regeneron, Inc.

2.2: Comparison of DCE-MRI Models

2.2.1: Introduction

Paramagnetic gadolinium chelates have been extensively used as contrast agents (CA) for both qualitative and quantitative MRI. Signal enhancement in contrast-enhanced MRI is due to an interaction between the injected paramagnetic contrast agent, usually Gd chelates, and the protons on water molecules commonly detected in MRI due to the high abundance of water and high gyromagnetic ratio of protons. These agents shorten the T_1 relaxation time proportional to their concentrations, within a certain range, resulting in increased T_1-weighted signal intensity. The injected CA, typically an intravascular agent, travels through the blood to a tissue of interest and in the case of aggressive tumors were vessels are compromised is able to leak into the extracellular extravascular space (EES).

In order to quantify tissue vascular properties, the signal enhancement kinetics seen in the images resulting from a bolus injection of CA are fit to a pharmacokinetic model, most often a two compartment transfer model between blood and the EES [26]. Physical tissue properties such as a vessel permeability constant (K^{Trans}) and the fractional volume of EES (v_e) are typical model parameters that are quantified in DCE-MRI. Although these models work very well in fitting to dynamic data and produce reasonable measurements of the desired tissue properties, the physics of MRI signal enhancement are much less direct than these purely pharmacokinetic models would imply.

A more recently developed model for use in DCE-MRI takes into account the mechanism of contrast enhancement in MRI as well as two-site water exchange between intra- and extra-cellular water pools, named the shutter-speed model (SSM) [35]. Contrast agents are not able to enter the intra-cellular space, but water molecules are mostly found within the cell and are able to penetrate the cell membrane. Due to the non-instantaneous measurement of the water signal,

there will inevitably be some exchange of water between the intra- and extra-cellular spaces, resulting in a modulation in the detected signal intensity. This shutter-speed effect has been shown to result in significant underestimation of parameters values, as much as 50% [35]. The shutter-speed model takes this water exchange into account when determining the contrast enhancement, and provides an extra parametric readout of the mean intra-cellular water molecule lifetime.

In the following, three popular DCE models are compared for the detection of parameter changes after VEGF blockade, using the same animal tumor model as was presented in the previous section. Similar parameters between the models are compared over the time course of anti-VEGF therapy and highlight differences in sensitivity for detecting tumor treatment response.

2.2.2: Methods

The data extracted from the animal experiments discussed in section 2.1 was used to explore several popular models of DCE-MRI signal enhancement due to contrast agent distribution in tissues [26, 35].

Models:

Tofts-Kermode (TK)

$$C_t(t) = K^{trans} \int_0^t C_p(t) e^{\left(-k_{ep}(t-\tau)\right)} d\tau \qquad [2.2.1]$$

This model considers tissue concentration change as the exchange of contrast agent (CA) between two compartments, blood plasma and extra-vascular extra-cellular space (EES). Here, C_p is the blood plasma concentration of CA, and the two optimized parameters are K^{Trans}, the CA transfer rate constant between blood and EES, and v_e, the tissue volume fraction of EES.

Efflux-Corrected (Patlak)

$$C_t(t) = K^{trans} \int_0^t C_p(t) e^{\left(-k_{ep}(t-\tau)\right)} d\tau + v_p C_p(t) \qquad [2.2.2]$$

This model is similar to the TK formalism, but takes into account a blood plasma tissue volume fraction term, v_p, to account for signal gain directly due to the arterial input function.

$$R_1(t) = \frac{2R_{1i} + r_{1o}[CR_o](t) + \frac{R_{1o} - R_{1i} + {}^1/_{\tau_i}}{p_o} - \sqrt{\left(\frac{2}{\tau_i} - r_{1o}[CR_o](t) - \frac{R_{1o} - R_{1i} + {}^1/_{\tau_i}}{p_o}\right)^2 + \frac{4(1-p_o)}{\tau_i^2 p_o}}}{2} \quad [2.2.3]$$

$$[CR_0] = L \int_0^t C_p(t) e^{(-L(t-\tau))} d\tau \quad [2.2.4]$$

This model combines two-site-exchange processes (between intra- and extra-cellular water) with the pharmacokinetic model of CA dynamics, resulting in an additional time constant term, τ_i, which describes the mean intracellular lifetime of a water molecule in the voxel. In this formalism, the parameters L and p_0 may be translated to K^{Trans} and v_e (for comparison to the other two models) by the following relations, where f_w is the tissue water volume fraction (assumed to be 0.8 [35]):

$$v_e = f_w \cdot p_0 \quad [2.2.5]$$

$$K^{Trans} = v_e \cdot L = f_w \cdot p_0 \cdot L \quad [2.2.6]$$

Area Under the Curve (AUC)

The AUC was determined as the integral of the signal enhancement curve over the time course of the experiment. This measurement gives a general sense of the mean signal enhancement over the entire time course, with leakier tumors having higher values and normal tissue with low values.

Statistics

In fitting the model to data, a goodness of fit (GoF) was also calculated as the normalized root mean squared deviation (NRMSD, between model and data) on a voxel-wise basis and averaged over the tumor volume. All significant differences between like parameters were evaluated at individual time points using a Student's two-tailed paired t-test and significance was assessed at values below p=0.05. Data in the plots are presented as the mean with error bars representing the standard error of the mean.

2.2.3: Results

For the purpose of model comparison, SSM model parameters, p_0 and L, were converted to values of v_e and K^{Trans} using the above equations 2.2.4-5, respectively. Figure 2.2.1 shows plots over the course of treatment of the percent change in average tumor (A-C) model parameters and (D) area under the curve (AUC) as well as (E) a measure of the average modeled

goodness of fit to the DCE data. A significant decrease in K^{Trans} is present one day after treatment initiation, and was maintained throughout the study period, for all models. Significant differences were also seen at almost all time points and between all models, with the exception of day 4 post-treatment between the TK and SSM models (p=0.06). Values for v_e only significantly changed from baseline levels on day 4 as determined by Patlak and SSM, but not TK. Also on day 4, the SSM model detected a significantly greater decrease in v_e than the Patlak and TK models, and the percent change was also significantly lower than the TK model on day 11. Both v_p and τ_i, in the Patlak and SSM models, respectively, dropped significantly by day 1 and remained low until the end of the study. AUC also dropped significantly after treatment, indicating an overall decrease in signal enhancement within the tumor.

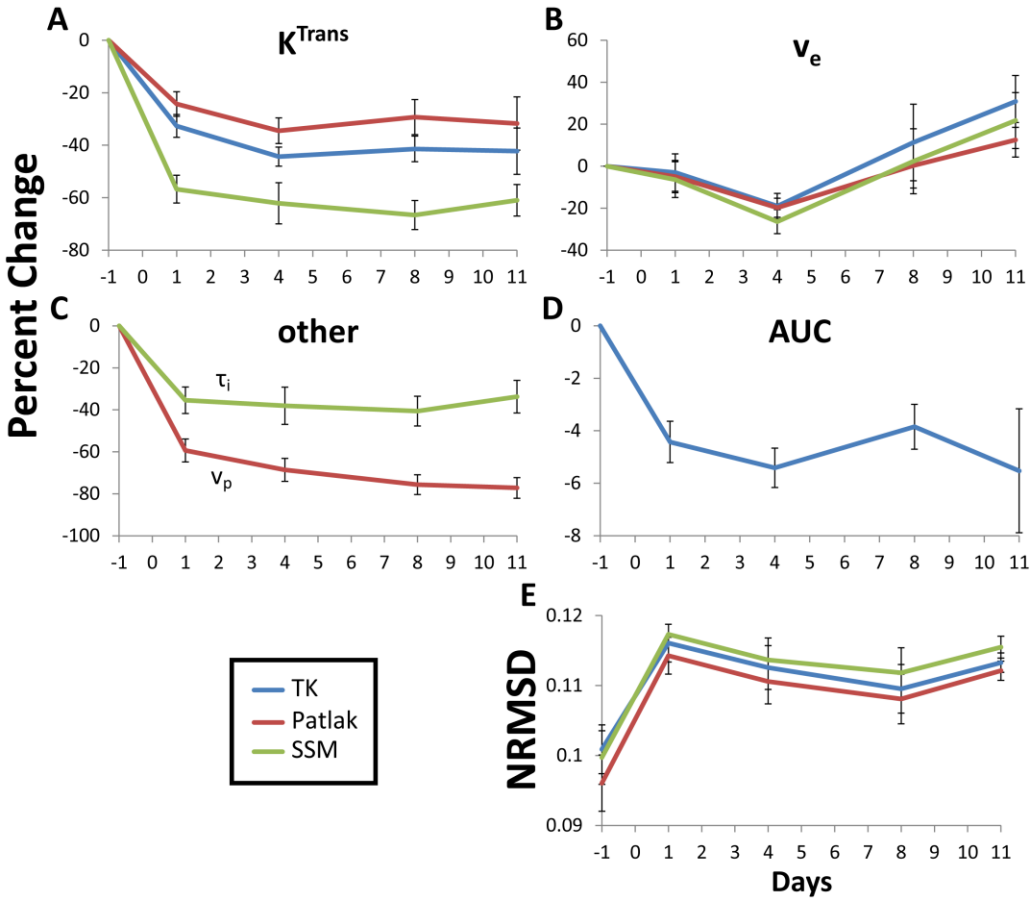

Figure 2.2.1: Plots over time show differences between models in comparable parameters means of (A) K^{Trans}, (B) v_e, and (C) tertiary parameters (τ_i from SSM and v_p from the Patlak model). Plots over time of the (D) mean tumor area under the signal intensity curve (AUC) and (E) goodness of fit. Errors are presented as standard error of the mean (SEM).

As seen in Figure 2.2.1E, the Patlak model generally had the best fit to the data, but no significant difference in GoF was found between any of the models at any time point. For all models, the NRMSD increased after treatment and remained elevated throughout the study (significantly higher on days 1 and 4).

2.2.4: Discussion

VEGF, which is often over-expressed in cancer cell lines, is known to stimulate the formation of blood vessels critical for the continual growth of the lesion. Neovasculature has been shown to have more irregular spacing and results in greater leakiness than established vessels. From the perspective of DCE modeling, this results in a high transfer rate, K^{Trans}, from the blood to the EES, as well as a high fractional blood volume in the tumor. VEGF inhibition would therefore be expected to decrease both K^{Trans} and v_p, which was observed in this study.

In searching for an imaging biomarker, the observed readout should be related to a specific physiological response as well as providing the greatest contrast between pre- and post-therapy states. Overall, the SSM model parameters appear to be the most sensitive to anti-VEGF treatment, with substantial drops in both K^{Trans} (-57%) and τ_i (-35%) within one day of the first treatment, even though the model seemed to result in the poorest fit to the data. Values of K^{Trans} determined by the TK (1.6 ± 0.1 [$x10^{-4}$] /s) and Patlak (1.3 ± 0.1 [$x10^{-4}$] /s) models on day -1 were approximately 28% or 40% lower than those found using the SSM model (2.7 ± 0.5 [$x10^{-4}$] /s), respectively, similar to findings reported by Yankeelov et al. [35]. This underestimation of K^{Trans}, however, did not persist after treatment, which agrees with the significant drop in the SSM parameter, τ_i, and indicates a faster water exchange between intra- and extra-cellular water. The Patlak model's v_p parameter was also very sensitive, with a 60% drop within the first day, but it had the least sensitive K^{Trans} (-24%) readout compared to both other models. For all models, v_e was found to be an insensitive biomarker for this type of therapy. The increase in NRMSD for all models after treatment corresponds well with the decrease in AUC, indicating an intuitively increased error due to lower signal.

In conclusion, all models were sensitive to vascular changes induced by this VEGF inhibition therapy. Although the Patlak model fit the data significantly better than the SSM, both

models' parameters (K^{Trans}, v_p, and τ_i) were significantly more sensitive than the TK (K^{Trans}), indicating that they would be better-suited as an imaging biomarker in this case.

2.3: DCE Model Sensitivity Analysis

2.3.1: Introduction

As was previously mentioned (Section Diffusion Model Sensitivity Analysis), when determining a model's usefulness in providing sensitive biomarkers for indication of treatment response it is important to understand the reliability of its readout.

2.3.2: Methods

Analytical methods of testing local parameter sensitivity and model sensitivity to noise are described previously (p. 25). The base model is in the form of either tissue gadolinium concentration, C_t (TK, Patlak), or R_1 (SSM), which can be translated to signal-based models, and thus the sensitivity coefficient (SC), using the chain rule (Appendix A). Sensitivity coefficients were evaluated over the time course of the experiment. Baseline parameters for each model are shown in Table 2.2.

Table 2.2: Baseline DCE model parameter values.

Tofts-Kermode	Efflux-corrected Patlak	Shutter-Speed
K^{Trans} (s^{-1})	K^{Trans} (s^{-1})	L (s^{-1})
1.7×10^{-4}	1.7×10^{-4}	4×10^{-3}
v_e	v_e	p_0
0.05	0.05	0.05
	v_p	τ_i
	0.005	1.2

2.3.3: Results

Model Sensitivity to Parameter Changes

Figure 2.3.1 shows plots over the imaging time course of SC for each model: (A) TK, (B) Patlak, and (C) SSM. For the SSM, sensitivity for the parameters L and p_0 are shown, but their sensitivity coefficients are equal to those of their converted counterparts, K^{Trans} and v_e, respectively.

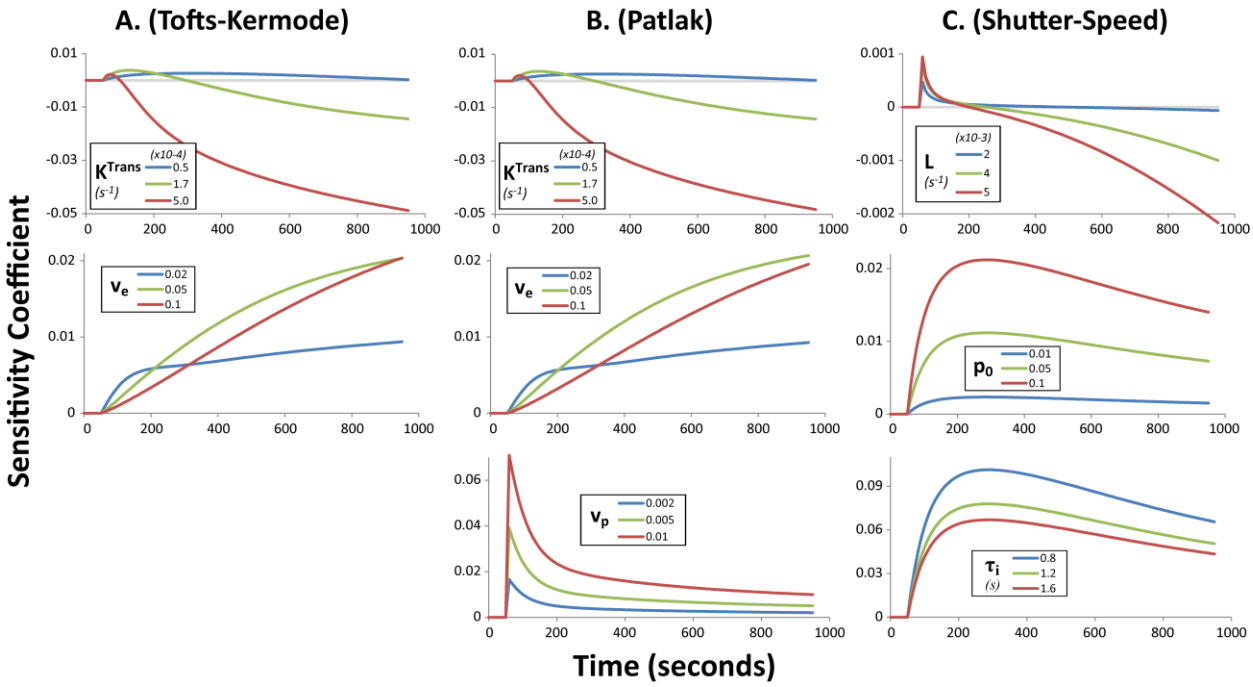

Figure 2.3.1: Plots over the time course of DCE model sensitivity coefficient for (A) Tofts-Kermode, (B) efflux-corrected Patlak, and (C) shutter speed (SSM) models. For the purpose of comparison of SSM parameters to the others, SC(L) is equivalent to SC(K^{Trans}) and SC(p_0) is equivalent to SC(v_e). Each plot shows dS/dp_i, where p_i is the parameter of interest, for three reference values of p_i (blue = low, green = mid, and red = high).

All parameters show zero sensitivity at the beginning due to the delay between the start of imaging and the arrival of the CA bolus to the tissue. K^{Trans} and v_e sensitivities are almost identical between the TK and Patlak models, as the only difference between the two is the additive v_p term in the Patlak model. All models' K^{Trans} values show similar trends, with an early increase to peak, then fall past 0 to greater negative magnitudes toward the end. L, in the SSM model, however is about 1/10 the SC(K^{Trans}) in the other two models and has a very sharp peak, coinciding with the bolus of CA and indicative that it is highly influenced by C_p. This is similar to v_p sensitivity from the Patlak model, which is more directly affected by C_p, but v_p has a high sensitivity compared to v_e and K^{Trans}. A greater difference in SC shape can be seen between the parameters v_e and p_0, where SC(p_0) reaches a peak around 290 seconds while SC(v_e) does not peak within the time of the experiment.

A general trend within almost all parameters is that higher reference parameter values result in higher overall sensitivity coefficients. The exception is τ_i, which has lower sensitivity with higher reference value.

Model Fitting Sensitivity to Noise

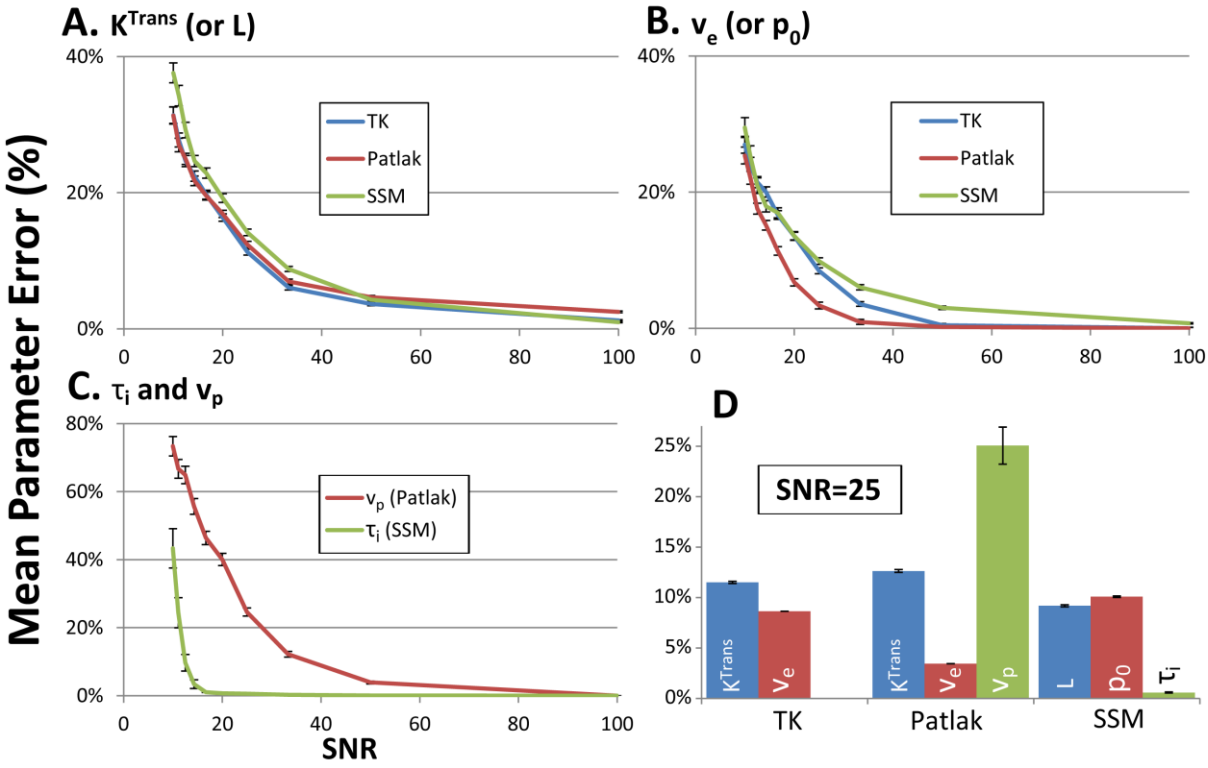

Figure 2.3.2: Resulting mean absolute error plotted against SNR for Tofts-Kermode (blue), Patlak (red), and Shutter-Speed (green) models. K^{Trans} and L parameter errors (A) are very similar between models, as are v_e and p_0 parameter errors (B), with v_e from the Patlak model substantially lower than the other two above SNR=15. Additional DCE parameter errors, for v_p (Patlak) and τ_i (SSM), are shown in (C). Parameter errors were also plotted against each other for a SNR of 25 (D), which is typical for DCE-MRI images. Error bars are standard error of the mean.

Figure 2.3.2 shows plots of parameter errors over a range of SNR, from 10 to 100, for (A) K^{Trans} (and L), (B) v_e (and p_0), and (C) v_p and τ_i. In all models, K^{Trans} (L for the SSM model, Figure 2.3.2A) has very similar sensitivity to noise, with slightly higher error in the SSM model. Measurement errors of v_e (p_0 for the SSM model, Figure 2.3.2B) were also very similar between models, with the Patlak model's error lower than the other two. Tertiary parameter errors for the

Patlak and SSM models, v_p and τ_i (Figure 2.3.2C), respectively, show a very low error in τ_i above SNR=15 and a very high error in v_p under SNR=50. Figure 2.3.2D compares these parameters for SNR=25, which is typical for pre-clinical DCE-MRI acquisitions. Of all models, the parameter with the highest sensitivity to noise was v_p, with 40% error at SNR=20, and the lowest sensitivity to noise was τ_i, with 1% error at SNR=16.7.

2.3.4: Discussion

The sensitivity analysis presented here demonstrates how similar parameters from different models can have drastically varying behaviors. Although the TK and Patlak models behave very similarly due to the minimal difference between them, the SSM model exhibits less sensitivity to the transfer rate constant (L) than the other two (K^{Trans}) by an order of magnitude. Despite this difference, K^{Trans} and v_e parameters exhibit very similar noise error behavior. The Patlak model's v_p parameter had the highest SC overall, but was also very sensitive to noise, making it an unreliable readout at low SNR. On the other hand, the τ_i parameter in the SSM model also had high SC, but was the least sensitive to noise, making it a very good candidate for an imaging response biomarker.

DCE-MRI images are acquired using a T_1-weighted gradient echo sequence that typically has SNR on the order of 25, which, according to the above simulations, may result in possible 9-12% errors in K^{Trans} or L readouts and 3-10% errors in v_e or p_0 readouts. Based on this sensitivity analysis, the SSM model appears to be the best choice for accurately detecting treatment response in this model as long as τ_i is expected to change. The high model sensitivity to τ_i and low sensitivity to noise coupled with the drop in both K^{Trans} and τ_i seen in section 2.2 make this model stand above the TK and Patlak models.

2.4: References

[1] Stupp R, Mason WP, van den Bent MJ, Weller M, Fisher B, Taphoorn MJ, Belanger K, Brandes AA, Marosi C, Bogdahn U, Curschmann J, Janzer RC, Ludwin SK, Gorlia T, Allgeier A, Lacombe D, Cairncross JG, Eisenhauer E, Mirimanoff RO. Radiotherapy plus concomitant and adjuvant temozolomide for glioblastoma. N Engl J Med 2005;352: 987-96.

[2] Thaker NG, Pollack IF. Molecularly targeted therapies for malignant glioma: rationale for combinatorial strategies. Expert Rev Neurother 2009;9: 1815-36.

[3] Yamanaka R, Saya H. Molecularly targeted therapies for glioma. Ann Neurol 2009;66: 717-29.

[4] Ferrara N, Kerbel RS. Angiogenesis as a therapeutic target. Nature 2005;438: 967-74.

[5] Gasparini G, Longo R, Toi M, Ferrara N. Angiogenic inhibitors: a new therapeutic strategy in oncology. Nat Clin Pract Oncol 2005;2: 562-77.
[6] Raizer JJ, Grimm S, Chamberlain MC, Nicholas MK, Chandler JP, Muro K, Dubner S, Rademaker AW, Renfrow J, Bredel M. A phase 2 trial of single-agent bevacizumab given in an every-3-week schedule for patients with recurrent high-grade gliomas. Cancer 2010;116: 5297-305.
[7] Schmidt NO, Westphal M, Hagel C, Ergun S, Stavrou D, Rosen EM, Lamszus K. Levels of vascular endothelial growth factor, hepatocyte growth factor/scatter factor and basic fibroblast growth factor in human gliomas and their relation to angiogenesis. Int J Cancer 1999;84: 10-8.
[8] Bauerle T, Bartling S, Berger M, Schmitt-Graff A, Hilbig H, Kauczor HU, Delorme S, Kiessling F. Imaging anti-angiogenic treatment response with DCE-VCT, DCE-MRI and DWI in an animal model of breast cancer bone metastasis. Eur J Radiol 2010;73: 280-7.
[9] Byrne AT, Ross L, Holash J, Nakanishi M, Hu L, Hofmann JI, Yancopoulos GD, Jaffe RB. Vascular endothelial growth factor-trap decreases tumor burden, inhibits ascites, and causes dramatic vascular remodeling in an ovarian cancer model. Clin Cancer Res 2003;9: 5721-8.
[10] Inai T, Mancuso M, Hashizume H, Baffert F, Haskell A, Baluk P, Hu-Lowe DD, Shalinsky DR, Thurston G, Yancopoulos GD, McDonald DM. Inhibition of vascular endothelial growth factor (VEGF) signaling in cancer causes loss of endothelial fenestrations, regression of tumor vessels, and appearance of basement membrane ghosts. Am J Pathol 2004;165: 35-52.
[11] Kadenhe-Chiweshe A, Papa J, McCrudden KW, Frischer J, Bae JO, Huang J, Fisher J, Lefkowitch JH, Feirt N, Rudge J, Holash J, Yancopoulos GD, Kandel JJ, Yamashiro DJ. Sustained VEGF blockade results in microenvironmental sequestration of VEGF by tumors and persistent VEGF receptor-2 activation. Mol Cancer Res 2008;6: 1-9.
[12] Maxwell RJ, Wilson J, Prise VE, Vojnovic B, Rustin GJ, Lodge MA, Tozer GM. Evaluation of the anti-vascular effects of combretastatin in rodent tumours by dynamic contrast enhanced MRI. NMR Biomed 2002;15: 89-98.
[13] Raatschen HJ, Simon GH, Fu Y, Sennino B, Shames DM, Wendland MF, McDonald DM, Brasch RC. Vascular permeability during antiangiogenesis treatment: MR imaging assay results as biomarker for subsequent tumor growth in rats. Radiology 2008;247: 391-9.
[14] Riely GJ, Miller VA. Vascular endothelial growth factor trap in non small cell lung cancer. Clin Cancer Res 2007;13: s4623-7.
[15] Huang J, Frischer JS, Serur A, Kadenhe A, Yokoi A, McCrudden KW, New T, O'Toole K, Zabski S, Rudge JS, Holash J, Yancopoulos GD, Yamashiro DJ, Kandel JJ. Regression of established tumors and metastases by potent vascular endothelial growth factor blockade. Proc Natl Acad Sci U S A 2003;100: 7785-90.
[16] Baffert F, Le T, Sennino B, Thurston G, Kuo CJ, Hu-Lowe D, McDonald DM. Cellular changes in normal blood capillaries undergoing regression after inhibition of VEGF signaling. Am J Physiol Heart Circ Physiol 2006;290: H547-59.
[17] Fricke I, Mirza N, Dupont J, Lockhart C, Jackson A, Lee JH, Sosman JA, Gabrilovich DI. Vascular endothelial growth factor-trap overcomes defects in dendritic cell differentiation but does not improve antigen-specific immune responses. Clin Cancer Res 2007;13: 4840-8.

[18] Holash J, Davis S, Papadopoulos N, Croll SD, Ho L, Russell M, Boland P, Leidich R, Hylton D, Burova E, Ioffe E, Huang T, Radziejewski C, Bailey K, Fandl JP, Daly T, Wiegand SJ, Yancopoulos GD, Rudge JS. VEGF-Trap: a VEGF blocker with potent antitumor effects. Proc Natl Acad Sci U S A 2002;99: 11393-8.
[19] Kim ES, Serur A, Huang J, Manley CA, McCrudden KW, Frischer JS, Soffer SZ, Ring L, New T, Zabski S, Rudge JS, Holash J, Yancopoulos GD, Kandel JJ, Yamashiro DJ. Potent VEGF blockade causes regression of coopted vessels in a model of neuroblastoma. Proc Natl Acad Sci U S A 2002;99: 11399-404.
[20] Rudge JS, Holash J, Hylton D, Russell M, Jiang S, Leidich R, Papadopoulos N, Pyles EA, Torri A, Wiegand SJ, Thurston G, Stahl N, Yancopoulos GD. VEGF Trap complex formation measures production rates of VEGF, providing a biomarker for predicting efficacious angiogenic blockade. Proc Natl Acad Sci U S A 2007;104: 18363-70.
[21] Bergers G, Benjamin LE. Tumorigenesis and the angiogenic switch. Nat Rev Cancer 2003;3: 401-10.
[22] Hanahan D, Weinberg RA. The hallmarks of cancer. Cell 2000;100: 57-70.
[23] Yankeelov TE, Gore JC. Dynamic Contrast Enhanced Magnetic Resonance Imaging in Oncology: Theory, Data Acquisition, Analysis, and Examples. Curr Med Imaging Rev 2009;3: 91-107.
[24] Kety SS. The theory and applications of the exchange of inert gas at the lungs and tissues. Pharmacol Rev 1951;3: 1-41.
[25] Kovar DA, Lewis M, Karczmar GS. A new method for imaging perfusion and contrast extraction fraction: input functions derived from reference tissues. J Magn Reson Imaging 1998;8: 1126-34.
[26] Tofts PS. Modeling tracer kinetics in dynamic Gd-DTPA MR imaging. J Magn Reson Imaging 1997;7: 91-101.
[27] Chenevert TL, Stegman LD, Taylor JM, Robertson PL, Greenberg HS, Rehemtulla A, Ross BD. Diffusion magnetic resonance imaging: an early surrogate marker of therapeutic efficacy in brain tumors. J Natl Cancer Inst 2000;92: 2029-36.
[28] Chenevert TL, Sundgren PC, Ross BD. Diffusion imaging: insight to cell status and cytoarchitecture. Neuroimaging Clin N Am 2006;16: 619-32, viii-ix.
[29] Galbán S, Brisset JC, Rehemtulla A, Chenevert TL, Ross BD, Galbán CJ. Diffusion-weighted MRI for assessment of early cancer treatment response. Curr Pharm Biotechnol 2010;11: 701-8.
[30] Hamstra DA, Rehemtulla A, Ross BD. Diffusion magnetic resonance imaging: a biomarker for treatment response in oncology. J Clin Oncol 2007;25: 4104-9.
[31] Ellingson BM, Malkin MG, Rand SD, Connelly JM, Quinsey C, LaViolette PS, Bedekar DP, Schmainda KM. Validation of functional diffusion maps (fDMs) as a biomarker for human glioma cellularity. J Magn Reson Imaging 2010;31: 538-48.
[32] Moffat BA, Hall DE, Stojanovska J, McConville PJ, Moody JB, Chenevert TL, Rehemtulla A, Ross BD. Diffusion imaging for evaluation of tumor therapies in preclinical animal models. MAGMA 2004;17: 249-59.
[33] Ross BD, Zhao YJ, Neal ER, Stegman LD, Ercolani M, Ben-Yoseph O, Chenevert TL. Contributions of cell kill and posttreatment tumor growth rates to the repopulation of intracerebral 9L tumors after chemotherapy: an MRI study. Proc Natl Acad Sci U S A 1998;95: 7012-7.

[34] Batchelor TT, Sorensen AG, di Tomaso E, Zhang WT, Duda DG, Cohen KS, Kozak KR, Cahill DP, Chen PJ, Zhu M, Ancukiewicz M, Mrugala MM, Plotkin S, Drappatz J, Louis DN, Ivy P, Scadden DT, Benner T, Loeffler JS, Wen PY, Jain RK. AZD2171, a pan-VEGF receptor tyrosine kinase inhibitor, normalizes tumor vasculature and alleviates edema in glioblastoma patients. Cancer Cell 2007;11: 83-95.
[35] Yankeelov TE, Rooney WD, Li X, Springer CS, Jr. Variation of the relaxographic "shutter-speed" for transcytolemmal water exchange affects the CR bolus-tracking curve shape. Magn Reson Med 2003;50: 1151-69.
[36] Bocci G, Man S, Green SK, Francia G, Ebos JM, du Manoir JM, Weinerman A, Emmenegger U, Ma L, Thorpe P, Davidoff A, Huber J, Hicklin DJ, Kerbel RS. Increased plasma vascular endothelial growth factor (VEGF) as a surrogate marker for optimal therapeutic dosing of VEGF receptor-2 monoclonal antibodies. Cancer Res 2004;64: 6616-25.
[37] Choi H, Charnsangavej C, de Castro Faria S, Tamm EP, Benjamin RS, Johnson MM, Macapinlac HA, Podoloff DA. CT evaluation of the response of gastrointestinal stromal tumors after imatinib mesylate treatment: a quantitative analysis correlated with FDG PET findings. AJR Am J Roentgenol 2004;183: 1619-28.
[38] Jaffe CC. Measures of response: RECIST, WHO, and new alternatives. J Clin Oncol 2006;24: 3245-51.
[39] Strumberg D, Richly H, Hilger RA, Schleucher N, Korfee S, Tewes M, Faghih M, Brendel E, Voliotis D, Haase CG, Schwartz B, Awada A, Voigtmann R, Scheulen ME, Seeber S. Phase I clinical and pharmacokinetic study of the Novel Raf kinase and vascular endothelial growth factor receptor inhibitor BAY 43-9006 in patients with advanced refractory solid tumors. J Clin Oncol 2005;23: 965-72.
[40] Hamstra DA, Galban CJ, Meyer CR, Johnson TD, Sundgren PC, Tsien C, Lawrence TS, Junck L, Ross DJ, Rehemtulla A, Ross BD, Chenevert TL. Functional diffusion map as an early imaging biomarker for high-grade glioma: correlation with conventional radiologic response and overall survival. J Clin Oncol 2008;26: 3387-94.
[41] Sorensen AG, Batchelor TT, Zhang WT, Chen PJ, Yeo P, Wang M, Jennings D, Wen PY, Lahdenranta J, Ancukiewicz M, di Tomaso E, Duda DG, Jain RK. A "vascular normalization index" as potential mechanistic biomarker to predict survival after a single dose of cediranib in recurrent glioblastoma patients. Cancer Res 2009;69: 5296-300.
[42] Gomez-Manzano C, Holash J, Fueyo J, Xu J, Conrad CA, Aldape KD, de Groot JF, Bekele BN, Yung WK. VEGF Trap induces antiglioma effect at different stages of disease. Neuro Oncol 2008;10: 940-5.
[43] Kunkel P, Ulbricht U, Bohlen P, Brockmann MA, Fillbrandt R, Stavrou D, Westphal M, Lamszus K. Inhibition of glioma angiogenesis and growth in vivo by systemic treatment with a monoclonal antibody against vascular endothelial growth factor receptor-2. Cancer Res 2001;61: 6624-8.
[44] Rubenstein JL, Kim J, Ozawa T, Zhang M, Westphal M, Deen DF, Shuman MA. Anti-VEGF antibody treatment of glioblastoma prolongs survival but results in increased vascular cooption. Neoplasia 2000;2: 306-14.
[45] Wachsberger PR, Burd R, Cardi C, Thakur M, Daskalakis C, Holash J, Yancopoulos GD, Dicker AP. VEGF trap in combination with radiotherapy improves tumor control in u87 glioblastoma. Int J Radiat Oncol Biol Phys 2007;67: 1526-37.

[46] Erber R, Thurnher A, Katsen AD, Groth G, Kerger H, Hammes HP, Menger MD, Ullrich A, Vajkoczy P. Combined inhibition of VEGF and PDGF signaling enforces tumor vessel regression by interfering with pericyte-mediated endothelial cell survival mechanisms. FASEB J 2004;18: 338-40.
[47] Drappatz J, Lee EQ, Hammond S, Grimm SA, Norden AD, Beroukhim R, Gerard M, Schiff D, Chi AS, Batchelor TT, Doherty LM, Ciampa AS, Lafrankie DC, Ruland S, Snodgrass SM, Raizer JJ, Wen PY. Phase I study of panobinostat in combination with bevacizumab for recurrent high-grade glioma. J Neurooncol 2012;107: 133-8.
[48] Vredenburgh JJ, Desjardins A, Reardon DA, Peters KB, Herndon JE, 2nd, Marcello J, Kirkpatrick JP, Sampson JH, Bailey L, Threatt S, Friedman AH, Bigner DD, Friedman HS. The addition of bevacizumab to standard radiation therapy and temozolomide followed by bevacizumab, temozolomide, and irinotecan for newly diagnosed glioblastoma. Clin Cancer Res 2011;17: 4119-24.
[49] Zhang W, Fulci G, Buhrman JS, Stemmer-Rachamimov AO, Chen JW, Wojtkiewicz GR, Weissleder R, Rabkin SD, Martuza RL. Bevacizumab with angiostatin-armed oHSV increases antiangiogenesis and decreases bevacizumab-induced invasion in U87 glioma. Mol Ther 2012;20: 37-45.

Chapter 3: **Multimodality Imaging**

3.1: Multimodality Imaging of Bone Metastatic Cancer

Included with permission from the editor of Translational Oncology:

Hoff BA, Chughtai K, Jeon YH, Kozloff K, Galbán S, Rehemtulla A, Ross BD, Galbán CJ. Multimodality imaging of tumor and bone response in a mouse model of bony metastasis. Transl Oncol. 2012 Dec;5(6):415-21.

3.1.1: Introduction

Bone metastases occur in more than 70% of advanced breast cancer patients with complications including bone fracture, pain, and spinal compression [1]. More than 250,000 patient deaths worldwide result from breast cancer, mainly attributed to metastatic disease [1]. Current treatments include systemic cytotoxic drugs, as well as bisphosphonates used for inhibition of bone loss, and are limited in their efficacy for combating bony metastasis [2, 3]. Much recent research has been focused on targeted agents that disrupt specific closely involved signaling pathways in cancer. Effects of these treatments can be highly complex, which present challenges for the characterization of treatment response owing to the numerous mechanisms involved [4]. For example, recent studies in skeletal metastases have revealed important interactions between the tumor and its microenvironment [5-9]. It is well known that bone tissue harbors a latent pool of transforming growth factor–β (TGF-β) that when released by bone resorption propagates cancer growth in skeletal regions [2, 10-12]. The discovery of this interdependency has spurred development of new targeted drugs to inhibit this cycle, resulting in a spectrum of agents targeting various stages of the cycle including TGF-β receptors in cancer cells, RANK in osteoclast precursors, cathepsin-K, and bisphosphonates for inhibiting osteoclast activity [11]. Conventional anatomic imaging and histologic techniques for quantifying response to therapy are insufficient for capturing the time-dependent interactions and targeted mechanisms of this complex system. Conventional approaches to monitoring cancer response to therapy are

limited, with the most prevalent being changes in tumor volume followed by quantitative measurements of tissue perfusion and diffusion. Because of the unconventional action these agents have on metastatic breast cancer to the bone, a more comprehensive assessment of tumor biology and response to intervention would provide investigators developing new targeted agents with improved insights into the complicated interrelationships of the signaling pathways and their role in tumor growth and cell death.

In this study, a multimodality approach to imaging treatment response was undertaken in an effort to more fully delineate the underlying biologic responses to bisphosphonate and taxane treatment using a mouse model of established breast cancer metastasis to the bone. Molecular resonance imaging (MRI) was used to monitor tumor soft tissue volumetric response and cellularity; micro-computed tomography (μCT) was used to monitor bone characteristics; bioluminescence imaging (BLI) was used to monitor apoptosis by measuring caspase-3–linked activation; and fluorescent probes targeting bone mineralization and cathepsin-K activity were used to provide information related to bone remodeling activity. Noninvasive imaging provided for longitudinal assessment of differential treatment effects on bone and tumor following administration with docetaxel and zoledronic acid (ZA). Imaging readouts were able to follow signatures unique to response of tumor and bone, revealing the capability of applying imaging modalities to "unmix" the complex biologic responses to individual therapies, thus providing opportunities for assessing more complex treatments targeting mixed osteoblastic and osteoclastic phenotypes. Overall, the application of multiple imaging approaches described herein provide a more comprehensive and robust process than any single-modality approach for new drug evaluation and efficacy screening through delineation of treatment effects on tumor and bone morphology as well as functional and signaling pathways.

3.1.2: Materials

Animal Tumor Model

Female severe combined immunodeficiency mice were subject to intratibial implantation of MDA-MB-231 breast cancer sub-line 1833 cells transfected with a luciferase reporter on caspase-3 (Figure 3.1.1, PPOP [13], Promega Corporation, Madison, WI) in the right leg with 10^5 cells in 5μl of serum-free medium suspension. Briefly, mice were anesthetized with an intraperitoneal injection of ketamine and then leg hair was removed using Nair. An empty 0.5-

cm^3 insulin syringe was used to bore a hole down into the tibial marrow space through the tibial plateau through which a Hamilton syringe was then used to insert the cell suspension. A sham injection of media alone was performed on the left leg as a surgical control.

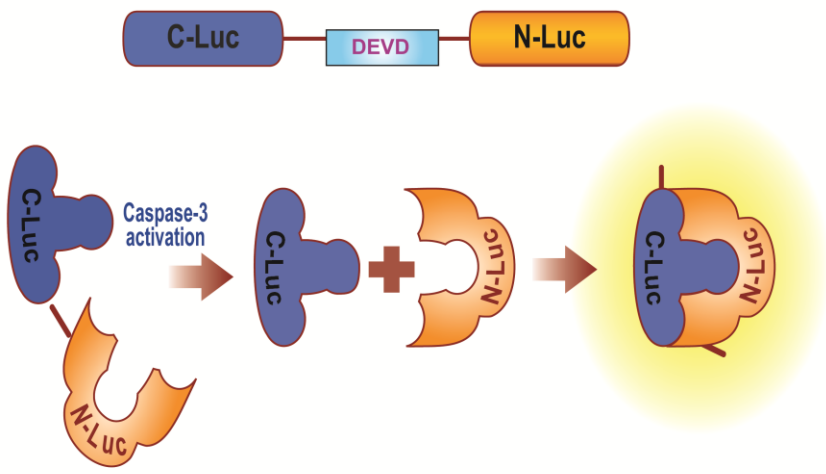

Figure 3.1.1: Diagram of the split luciferase construct used in this model. A split-luciferase complex is expressed in the cells with a DEVD sequence between the N- and C-Luc domains, keeping the enzyme inactive through steric hindrance. When caspase-3 is expressed in the cell, signaling the cell to begin apoptotic events, active caspase-3 cleaves the DEVD sequence from the rest of the enzyme. Active luciferase then metabolizes luciferin substrate and emits light.

Treatments

Once tumor size reached a volume of 10 to 20 mm^3 (as measured by MRI), mice were separated into treatment groups of ZA (n = 16), docetaxel (n = 7), or control (n = 17). ZA treatment was administered subcutaneously as 100µg in 100µl of phosphate-buffered saline (PBS, 5mg/kg) per mouse twice weekly for four treatments, docetaxel was administered intravenously at a dose of 20mg/kg weekly for three cycles, and control mice were administered PBS with the same schedule as ZA. Control animals treated with 10% ethanol were also considered but were found not to differ from PBS controls so are not shown.

Imaging and Analysis

Molecular Resonance Imaging

MRI was performed using a 7-T, 16-cm horizontal bore DirectDrive System (Agilent Technologies, Palo Alto, CA) with a quadrature mouse head coil (m2m Imaging Corp,

Cleveland, OH). Images of the tumor-bearing leg were acquired twice weekly starting from the day before treatment initiation. Diffusion-weighted images were acquired using a spin-echo sequence with navigator echo motion correction and gradient waveforms sensitive to isotropic diffusion [14] using the following parameters: repetition time/echo time = 4000/37 ms, field of view = 20 × 20 mm, matrix size = 128 × 64, slice thickness = 0.5mm, slice number = 25, and b-values (diffusion weighting) of 120 and 1200s/mm^2. Following image acquisition, data that included manually drawing volumes of interest on the high diffusion-weighted image to compute tumor volumes and diffusion values were stored for analysis. Tumor volumes and apparent diffusion coefficient (ADC) values were quantified over time to monitor tumor burden and cellularity, respectively.

Micro Computed Tomography

μCT imaging was performed weekly starting from the day before treatment initiation using a Siemens Inveon System with the following parameters: 80kVp, 500μA, 300-ms exposure, 501 projections over 360 degrees, and 49.2-mm field of view (56-μm voxel size). Volumes of interest were drawn over the tibia from the tibia-fibula junction to the tibial plateau, measuring mean bone volume and mineral density throughout the study to monitor bone resorption.

Bioluminescence Imaging

For imaging of the PPOP-transfected cells, mice were injected with 200 mg/kg luciferin (Promega), and up to five mice were imaged in a single BLI scan, acquiring a series of images to find the total photon peak flux over a whole-leg region of interest (ROI) for each animal. Images were acquired on the day of treatment initiation and days 7, 10, 14, 21, and 28 afterward. BLI data were quantified as total photon peak flux normalized by tumor volume as measured by MRI.

Fluorescence Imaging

Fluorescence images were acquired on an IVIS Spectrum System (PerkinElmer, Inc, Walther, MA) every other week using the two probes: Osteosense 800 and CatK 680-FAST (PerkinElmer, Inc). Fluorescent probes were injected intravenously 24 hours before imaging, and hair was removed from the hind legs the same day using Nair lotion. The following optical filter sets were used for each acquisition:

Excitation (nm)	Emission (nm)		
430	500	580	640
675	720	740	760
745	800	820	840

After acquisition, images were spectrally unmixed using Living Image software (Caliper Life Sciences) to separate the two probe signals from each other and autofluorescence. ROIs with the same area were placed over both the left and right legs and signal was measured as the ratio (right/left) of mean radiant efficiency to account for variation in fluorophore injection, physiology, and possible accumulation of fluorescent agent because of the high frequency of imaging.

Statistics

A Student's t test was used to compare means between groups at each time point. Results with $P < 0.05$ were considered statistically significant. All plots represent mean ± SEM.

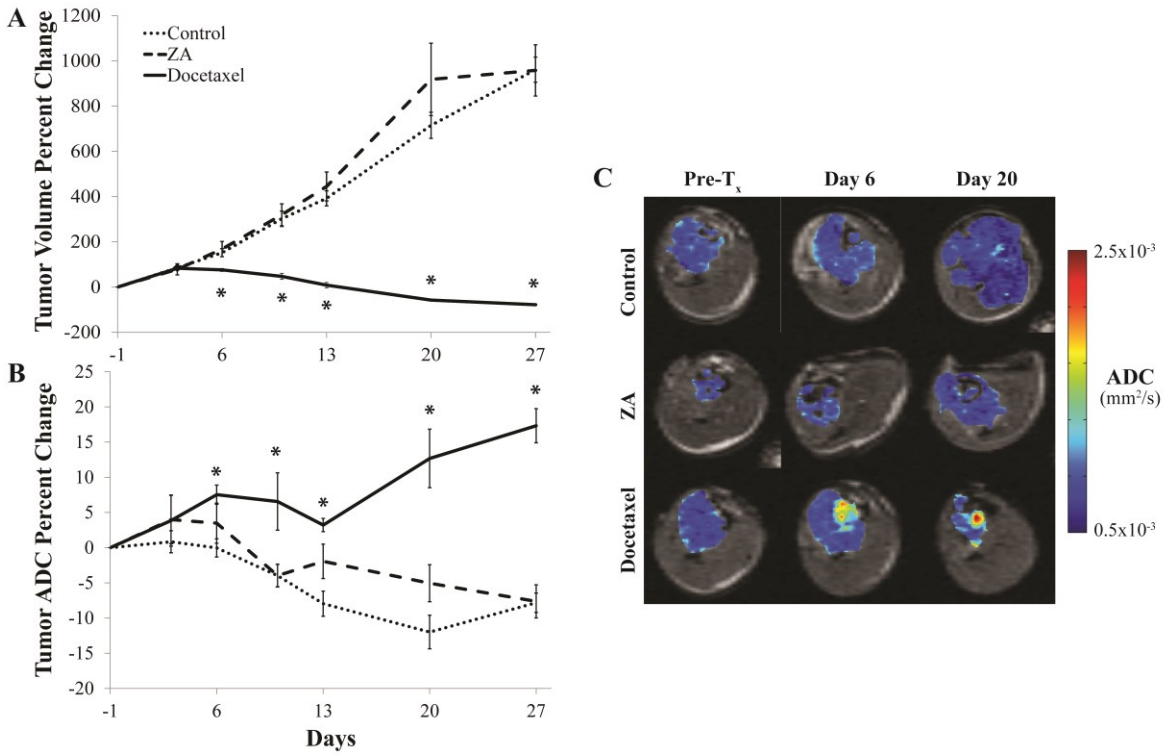

Figure 3.1.2: (A) Plots of percent change in tumor volume for each group show significant cell kill in the docetaxel group, but no significant effect in the ZA group. (B) Plots of percent change in tumor ADC show elevated values in the docetaxel group after day 6, but no significant change in the ZA group. (C) Representative ADC overlays show isolated areas of increased ADC in the docetaxel group (red) as well as a dramatic decrease in tumor volume seen at day 20. * indicates a significant difference from the control group ($p<0.05$).

3.1.3: Results

MRI was performed to monitor tumor volume and water diffusivity (ADC) twice weekly throughout the study (Figure 3.1.2). This modality was able to detect a significant retardation of tumor growth (Figure 3.1.2A) in the docetaxel-treated group by day 6 compared to the control and ZA-treated groups, which was followed by tumor shrinkage with no recovery within the study time frame. In addition, ADC values of the docetaxel-treated group were found to significantly increase by day 6 (Figure 3.1.2B), indicating that significant tumor cell death in the docetaxel group had occurred following treatment initiation. The ZA group, however, showed no significant difference from control tumor ADC values over the duration of the study although both trended downward, indicating that increasing density or packing of tumor cells occurred during the multifold volumetric increase in tumor size. Representative ADC map overlays for each of the animal groups (Figure 3.1.2C) revealed consistently low ADC values in the control and ZA groups, whereas localized regions in the docetaxel-treated tumors became elevated before and during tumor shrinkage.

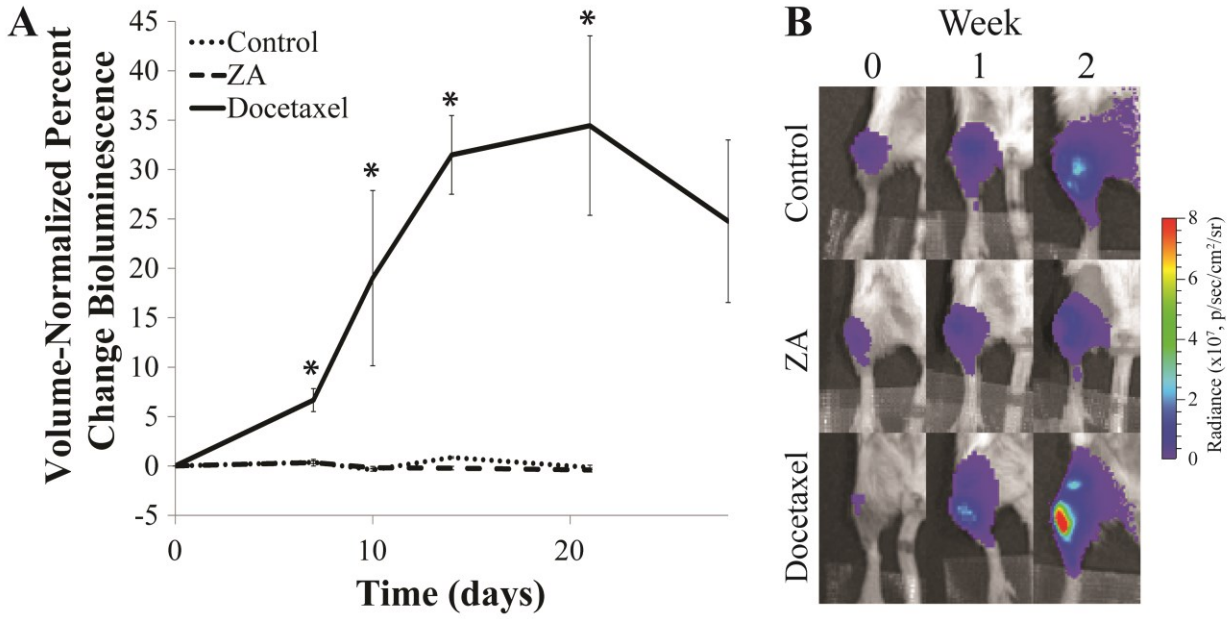

Figure 3.1.3: (A) Plots of overall luminescence of the tumor-bearing leg over time. Values are shown as the percent change of total photon flux (over a fixed-area ROI) normalized by tumor volume (as measured by MRI). (B) Representative radiance overlays show increased caspase-3 activity in the docetaxel group and minimal change in the control and ZA groups. * indicates a significant difference from the control group ($p<0.05$).

BLI of the PPOP reporter (Figure 3.1.3) revealed an increase in caspase-3 activity in the docetaxel group within 1 week of treatment, which remained elevated until the end of the study. Control and ZA groups both remained at baseline levels throughout the study, indicating that no significant apoptotic activation occurred. Representative bioluminescence images for each of the three groups (Figure 3.1.3B) showed that a stable low level of photons were emitted from the tumor sites in the control and ZA groups over time, whereas an increase in photon counts in the docetaxel group occurred (Figure 3.1.3B).

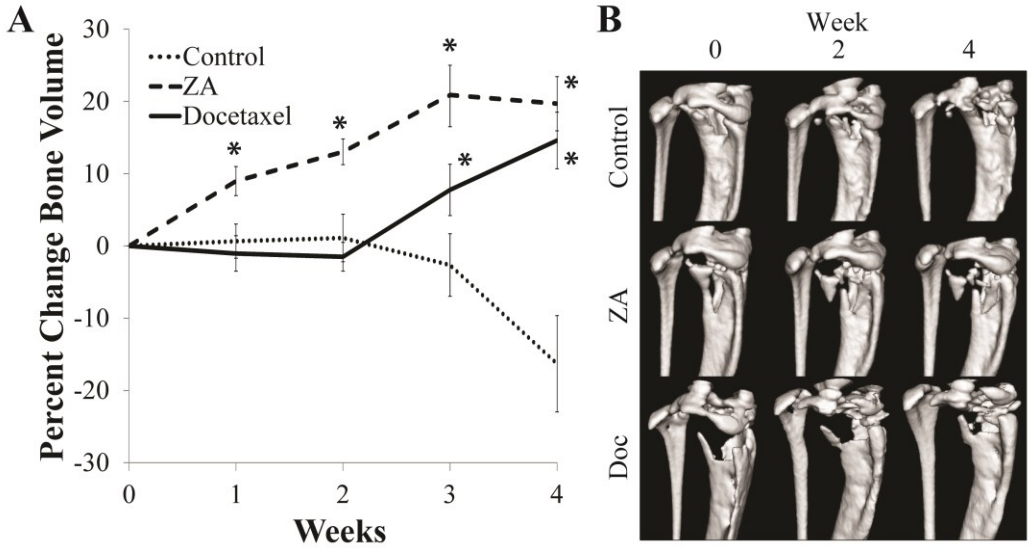

Figure 3.1.4: (A) Plots of tumor-bearing bone volume from μCT. The control group remained stable over the first two weeks followed by a sharp decline beginning at week 3. An increase in the ZA group was seen by the first week and remained elevated, while a significant increase was not seen in the docetaxel group until week 3 and almost reached the ZA group by week 4. (B) Representative image isosurfaces in the three groups. Controls presented successive bone degradation throughout the study. ZA-treated animals showed minimal changes in bone structure, with only fracturing caused by tumor growth. Docetaxel-treated animals showed some initial degradation through week 2 followed by recovery seen by week 4. * indicates a significant difference from the control group ($p<0.05$).

To monitor bone changes with therapy, μCT imaging was performed weekly and bone volume within the proximal tibia was quantified over the 4-week duration of the study (Figure 3.1.4A). Within 1 week of treatment with ZA, a significant increase in bone volume was detected, which remained elevated throughout the study. The docetaxel group showed a delayed bone response, with a significant increase in bone volume observed at week 3. Control mice were found to have a stable total bone volume until week 3 followed by significant bone

degradation. Representative images (Figure 3.1.4B) show progressive bone degradation in the control group throughout the study, whereas the ZA mouse's bone seemed to have stabilized even though growth of the soft tissue tumor appears to be fracturing the bone in certain weakened locations. Docetaxel-treated mice showed delayed bone response, with significant recovery by week 4.

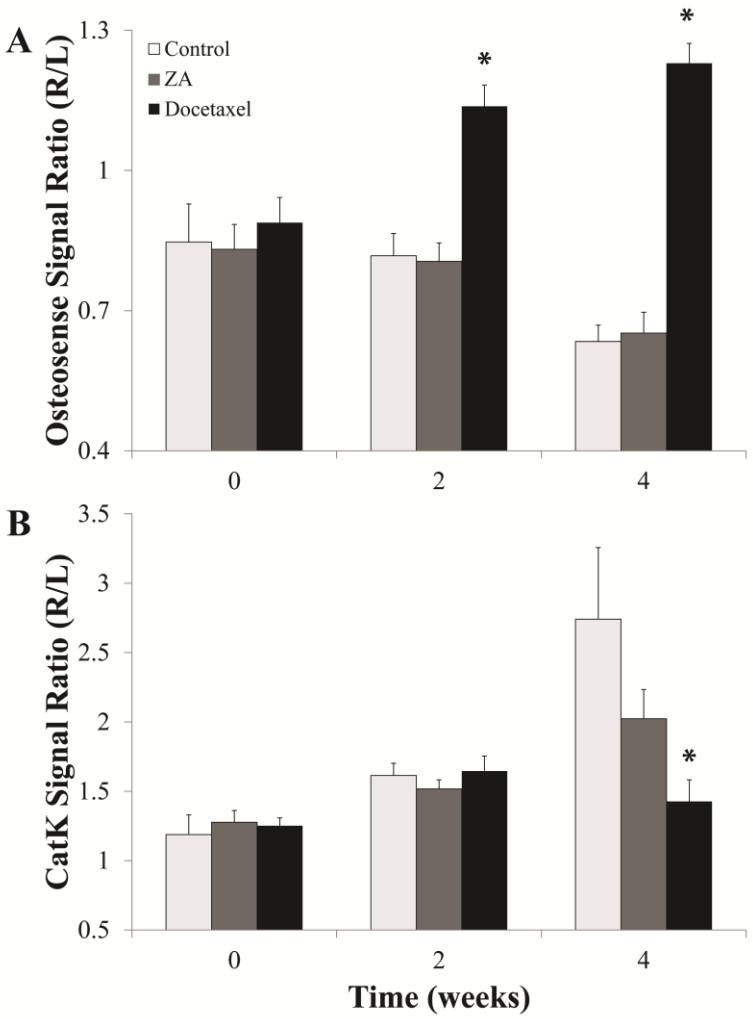

Figure 3.1.5: Bar plots of fluorescent signals in the tumor-bearing leg from (A) Osteosense 800 and (B) CatK 680-FAST are presented as values normalized by the non-tumor-bearing leg. The ZA group showed no significant difference from controls with either fluorescent probe, but the docetaxel group showed significant increases in Osteosense 800 uptake (A, black bar) on weeks 2 and 4 and a significant drop in CatK 680-FAST signal (B, black bar) on week 4. * indicates a significant difference from the control group ($p<0.05$).

Fluorescence imaging (FLI) was performed to obtain a more functional assessment of bone remodeling, with Osteosense 800 indicating the extent of bone reformation and activatable

CatK 680-FAST indicating the level of osteolytic activity. The plots in Figure 3.1.5 show that significant bone remodeling changes occurred at weeks 2 and 4 in the docetaxel-treated group, whereas there was no significant change detected in the ZA or control group. The progressive increase in relative Osteosense 800 signal for the docetaxel group indicated that there was a significant amount of bone reformation by week 2, earlier than the CT-evaluated bone response, which was maintained until the end of the study. CatK 680-FAST signal also showed a significant reduction compared to controls in the docetaxel group by week 4. The control group showed a progressive increase in CatK 680-FAST signal, indicating tumor growth and increased activation of osteoclasts. The ZA group did show attenuated CatK 680-FAST activation, which would be consistent with the reduction in bone loss seen by CT but was not found to be significant, compared to controls.

3.1.4: Discussion

The goal of this study was to investigate the use of multiple imaging biomarker readouts to interrogate interrelated biologic responses involved in the treatment of bony cancers in an effort to provide a more complete understanding of the overall biologic effects *in vivo*. Current preclinical studies rely heavily on histologic analysis, where a number of subjects must be sacrificed at each time point in the study to assess tissue responses. However, with the increasing variety of noninvasive imaging tools available, successful longitudinal studies may be strategically planned to reduce total subject numbers while maximizing the amount of information that can be extracted from each subject. This method will be increasingly useful for the evaluation of new therapies that may have multiple targets and require simultaneous monitoring of multiple processes. In the case of metastatic bone disease, assessments of treatments that affect both the soft tissue tumor and mineralized bone are important because of the known biologic interactions between the two as well as clinical implications in avoiding skeletal-related events, e.g., fracture. As newer treatments may not be directly involved in causing cell death or other conventionally quantifiable tissue responses, optical imaging techniques can be applied to assess treatment-related alterations in multiple cellular processes *in vivo* simultaneously and longitudinally over time. Optical readouts of treatment effects can be obtained from activatable and targeted FLI probes as well as genetically engineered tumor cells

whose molecular signaling events can be monitored noninvasively by BLI, which compliment more traditional imaging techniques such as MRI and CT.

The use of MRI and CT for evaluation of soft tissues and bone, respectively, has long been established. Quantification of tissue response to therapy using these imaging modalities has classically been through morphologic changes such as tumor or bone volume, with the more recent development of functional imaging techniques such as diffusion MRI [14-19] and perfusion measurements acquired by MRI or CT [20-23]. The recent trend in therapeutic research, however, is toward modification of specific cellular signaling pathways using targeted agents that may not have such drastic morphologic effects. With these new agents, conventional imaging approaches may not have enough sensitivity or specificity to determine treatment effects *in vivo*. In this study, we have presented a multimodality approach to evaluate treatment response using readouts obtained through pathway-specific optical imaging techniques backed by conventional μCT and MRI, which are clinically relevant modalities that provide more general information on morphology and gross tissue characteristics. We evaluated two treatments representing the extremes of either tumor-specific or bone-specific therapies to more easily illustrate the separate effects of these agents on the complex tumor-stromal interaction. Tumor ADC response has been tested on a broad range of cases and shown to correlate with cell death and often preclude any detectable change in tumor volume [14-19], however, ADC alone cannot determine the mechanism of cell death. The inclusion of caspase-3–coupled bioluminescence in this case provides the link between treatment and the specific mechanism. The significant increase in normalized BLI signal in the docetaxel group over the controls indicates that, through caspase-3 signaling, cells are undergoing apoptotic cell death. Tumor ADC values did not show a significant difference between docetaxel and control groups before tumor volume. This is attributed to MDA-MB-231 cell lines aggressiveness and high sensitivity to docetaxel.

FLI results using our two probes shed further light on the bone remodeling processes resulting from the tumor and treatments. Where μCT provides a high-resolution view of the current state of the bone, FLI is sensitive to the balance between processes of bone formation and erosion. The significant increase in the Osteosense 800 signal and dampening of the CatK 680-FAST signal for the docetaxel group indicates that induction of tumor cell kill and subsequent reduction in tumor burden has inhibited the tumor-stromal interaction, i.e., “vicious cycle” [2], and shifted the balance of osteoblastic and osteolytic activities toward recovery. Tumor

apoptosis, following effective treatment by docetaxel, led to a reduction in osteoclast recruitment and subsequently fewer cathepsin-K–expressing cells in that region, where even MDA-MB-231 cells have been shown to express cathepsin-K [24]. In addition, the disruption of the tumor-stromal interaction allowed for an up-regulation of osteoblastic activity as evidenced by an increase in Osteosense 800 signaling. As expected, treatment with ZA had no effect on tumor burden, suggesting that tumor signaling to the stroma was undisrupted during treatment. In contrast to what we observed using docetaxel, ZA did not significantly affect the Osteosense 800 signal ratio that would have been presumed based on the μCT results where an increase in bone volume was observed. Although not significant, the CatK 680-FAST signaling was slightly reduced in the ZA group when compared to controls. This may indicate that ZA protects the bone by reducing the extent of osteolytic activity, in essence shifting total bone turnover in the presence of a tumor from bone erosion to bone formation [14-23, 25-30].

When using a strategy for assessing the efficacy of a therapy using a multimodality imaging approach, it is important to take into account the limitations of the desired imaging modalities when planning a study. MRI and CT are both able to capture relatively high-resolution images, providing easily quantified volume and ADC measurements, as well as being translated to the clinic. These two modalities, however, do not provide any information about the signals or mechanics of the biologic system. In contrast, the optical techniques described here provide detailed information on biologic processes and signaling but are confined to preclinical use. BLI and FLI are known to present challenging hurdles for *in vivo* quantification, such as assumptions of light attenuation and scattering through tissues, limited spatial resolution, and error in the injected probe/substrate. In the presented work, the fluorescent signal in the tumor-bearing leg was normalized by the signal in the sham leg to account for variability of injection and heightened Osteosense 800 signal in the growth plates. The poor image resolution of FLI complicates matters further by having to contend with spillover signal from the growth plates. Nevertheless, with an established imaging protocol for acquiring data, care in image post-processing, and an appropriate model, these limitations can be overcome to provide a full picture of the effects of a therapeutic agent on a tumor-stromal microenvironment.

Overall, the experiments presented here demonstrate the use of multimodality imaging techniques for detection and quantification of multiple interrelated biologic processes affected by therapeutic intervention in a model of metastatic bone disease. Although the treatments were

selected on the basis of their current clinical relevance and their targeted effects on bone or tumor cells, this generalizable approach is anticipated to be useful in future studies identifying responses to experimental agents by obtaining a more complete understanding of the signaling pathways affected. These and other cancer cell lines have already been successfully engineered to express luciferase linked to cellular signals such as AKT, TGF-β, c-MET, epidermal growth factor receptor (EGFR), and others [25, 28, 30-32]. In addition, a wide variety of *in vivo* fluorescent agents (activatable and targeted) are already available, for imaging of many diseases. Selection of optical imaging agents, cell lines, and other imaging modalities, such as permeability MRI for measuring tumor vasculature, requires careful evaluation of which experimental readouts provide the most relevant information for assessing the efficacy of a novel agent as a single or combination therapy.

In summary, experimental therapeutic agents have traditionally relied on anatomic and functional imaging readouts of treatment response. With the emergence of optical imaging approaches including reporter cell–based constructs and activatable and targeted exogenously administered probes, the interdependence of treatment responses due to complex tumor-host interactions can be more fully delineated. BLI and FLI *in vivo* methods may be tailored to most diseases and treatment interventions and are complementary to MRI and CT imaging readouts. The use of a multimodality imaging strategy is anticipated to provide the pharmaceutical industry with cost-effective and efficient options for furthering overall drug development strategies.

3.1.5: References

[1] Coleman RE. Metastatic bone disease: clinical features, pathophysiology and treatment strategies. Cancer Treat Rev 2001;27: 165-76.

[2] Mundy GR. Metastasis to bone: causes, consequences and therapeutic opportunities. Nat Rev Cancer 2002;2: 584-93.

[3] Tkaczuk KH. Review of the contemporary cytotoxic and biologic combinations available for the treatment of metastatic breast cancer. Clin Ther 2009;31 Pt 2: 2273-89.

[4] Korpal M, Yan J, Lu X, Xu S, Lerit DA, Kang Y. Imaging transforming growth factor-beta signaling dynamics and therapeutic response in breast cancer bone metastasis. Nat Med 2009;15: 960-6.

[5] Casimiro S, Guise TA, Chirgwin J. The critical role of the bone microenvironment in cancer metastases. Mol Cell Endocrinol 2009;310: 71-81.

[6] Guise TA. The vicious cycle of bone metastases. J Musculoskelet Neuronal Interact 2002;2: 570-2.

[7] Joyce JA, Pollard JW. Microenvironmental regulation of metastasis. Nat Rev Cancer 2009;9: 239-52.
[8] Ooi LL, Zheng Y, Stalgis-Bilinski K, Dunstan CR. The bone remodeling environment is a factor in breast cancer bone metastasis. Bone 2011;48: 66-70.
[9] Zheng Y, Zhou H, Brennan K, Blair JM, Modzelewski JR, Seibel MJ, Dunstan CR. Inhibition of bone resorption, rather than direct cytotoxicity, mediates the anti-tumour actions of ibandronate and osteoprotegerin in a murine model of breast cancer bone metastasis. Bone 2007;40: 471-8.
[10] Dunn LK, Mohammad KS, Fournier PG, McKenna CR, Davis HW, Niewolna M, Peng XH, Chirgwin JM, Guise TA. Hypoxia and TGF-beta drive breast cancer bone metastases through parallel signaling pathways in tumor cells and the bone microenvironment. PLoS One 2009;4: e6896.
[11] Onishi T, Hayashi N, Theriault RL, Hortobagyi GN, Ueno NT. Future directions of bone-targeted therapy for metastatic breast cancer. Nat Rev Clin Oncol 2010;7: 641-51.
[12] Rose AA, Siegel PM. Emerging therapeutic targets in breast cancer bone metastasis. Future Oncol 2010;6: 55-74.
[13] Galbán S, Jeon YH, Sharkey LM, Hoff BA, Galbán CJ, Ross BD, Rehemtulla A. A genetically engineered mouse for imaging of apoptosis in a tissue specific manner. In: AACR. Chicago, IL; 2012.
[14] Moffat BA, Hall DE, Stojanovska J, McConville PJ, Moody JB, Chenevert TL, Rehemtulla A, Ross BD. Diffusion imaging for evaluation of tumor therapies in preclinical animal models. MAGMA 2004;17: 249-59.
[15] Chenevert TL, Stegman LD, Taylor JM, Robertson PL, Greenberg HS, Rehemtulla A, Ross BD. Diffusion magnetic resonance imaging: an early surrogate marker of therapeutic efficacy in brain tumors. J Natl Cancer Inst 2000;92: 2029-36.
[16] Galbán CJ, Bhojani MS, Lee KC, Meyer CR, Van Dort ME, Kuszpit KK, Koeppe RA, Ranga R, Moffat BA, Johnson TD, Chenevert TL, Rehemtulla A, Ross BD. Evaluation of treatment-associated inflammatory response on diffusion-weighted magnetic resonance imaging and 2-[18F]-fluoro-2-deoxy-D-glucose-positron emission tomography imaging biomarkers. Clin Cancer Res 2010;16: 1542-52.
[17] Hamstra DA, Rehemtulla A, Ross BD. Diffusion magnetic resonance imaging: a biomarker for treatment response in oncology. J Clin Oncol 2007;25: 4104-9.
[18] Hoff BA, Chenevert TL, Bhojani MS, Kwee TC, Rehemtulla A, Le Bihan D, Ross BD, Galban CJ. Assessment of multiexponential diffusion features as MRI cancer therapy response metrics. Magn Reson Med 2010;64: 1499-509.
[19] Ross BD, Moffat BA, Lawrence TS, Mukherji SK, Gebarski SS, Quint DJ, Johnson TD, Junck L, Robertson PL, Muraszko KM, Dong Q, Meyer CR, Bland PH, McConville P, Geng H, Rehemtulla A, Chenevert TL. Evaluation of cancer therapy using diffusion magnetic resonance imaging. Mol Cancer Ther 2003;2: 581-7.
[20] Bauerle T, Bartling S, Berger M, Schmitt-Graff A, Hilbig H, Kauczor HU, Delorme S, Kiessling F. Imaging anti-angiogenic treatment response with DCE-VCT, DCE-MRI and DWI in an animal model of breast cancer bone metastasis. Eur J Radiol 2010;73: 280-7.
[21] Hoff BA, Bhojani MS, Rudge J, Chenevert TL, Meyer CR, Galban S, Johnson TD, Leopold JS, Rehemtulla A, Ross BD, Galban CJ. DCE and DW-MRI monitoring of vascular disruption following VEGF-Trap treatment of a rat glioma model. NMR Biomed 2012;25: 935-42.

[22] Walker-Samuel S, Leach MO, Collins DJ. Evaluation of response to treatment using DCE-MRI: the relationship between initial area under the gadolinium curve (IAUGC) and quantitative pharmacokinetic analysis. Phys Med Biol 2006;51: 3593-602.
[23] Yankeelov TE, Lepage M, Chakravarthy A, Broome EE, Niermann KJ, Kelley MC, Meszoely I, Mayer IA, Herman CR, McManus K, Price RR, Gore JC. Integration of quantitative DCE-MRI and ADC mapping to monitor treatment response in human breast cancer: initial results. Magn Reson Imaging 2007;25: 1-13.
[24] Tomita A, Kasaoka T, Inui T, Toyoshima M, Nishiyama H, Saiki H, Iguchi H, Nakajima M. Human breast adenocarcinoma (MDA-231) and human lung squamous cell carcinoma (Hara) do not have the ability to cause bone resorption by themselves during the establishment of bone metastasis. Clin Exp Metastasis 2008;25: 437-44.
[25] Bhojani MS, Nyati MK, Zhao L, Normolle DP, Ross BD, Lawrence TS, Rehemtulla A. Molecular imaging of akt enables early prediction of response to molecular targeted therapy. Transl Oncol 2011;4: 122-5.
[26] Coppola JM, Ross BD, Rehemtulla A. Noninvasive imaging of apoptosis and its application in cancer therapeutics. Clin Cancer Res 2008;14: 2492-501.
[27] Galbán CJ, Galbán S, Van Dort ME, Luker GD, Bhojani MS, Rehemtulla A, Ross BD. Applications of molecular imaging. Prog Mol Biol Transl Sci 2010;95: 237-98.
[28] Nyati S, Schinske K, Ray D, Nyati MK, Ross BD, Rehemtulla A. Molecular imaging of TGFbeta-induced Smad2/3 phosphorylation reveals a role for receptor tyrosine kinases in modulating TGFbeta signaling. Clin Cancer Res 2011;17: 7424-39.
[29] Xie BW, Mol IM, Keereweer S, van Beek ER, Que I, Snoeks TJ, Chan A, Kaijzel EL, Lowik CW. Dual-wavelength imaging of tumor progression by activatable and targeting near-infrared fluorescent probes in a bioluminescent breast cancer model. PLoS One 2012;7: e31875.
[30] Zhang L, Virani S, Zhang Y, Bhojani MS, Burgess TL, Coxon A, Galban CJ, Ross BD, Rehemtulla A. Molecular imaging of c-Met tyrosine kinase activity. Anal Biochem 2011;412: 1-8.
[31] Khan AP, Contessa JN, Nyati MK, Ross BD, Rehemtulla A. Molecular imaging of epidermal growth factor receptor kinase activity. Anal Biochem 2011;417: 57-64.
[32] Zhang L, Lee KC, Bhojani MS, Khan AP, Shilman A, Holland EC, Ross BD, Rehemtulla A. Molecular imaging of Akt kinase activity. Nat Med 2007;13: 1114-9.

Chapter 4: **Parametric Response Map of CT Bone**

4.1: Detection of Bone Loss in a Rodent Model of Osteoporosis

Included with permission from Elsevier:

Hoff BA, Kozloff KM, Boes JL, Brisset JC, Galbán S, Van Poznak CH, Jacobson JA, Johnson TD, Meyer CR, Rehemtulla A, Ross BD, Galbán CJ. Parametric response mapping of CT images provides early detection of local bone loss in a rat model of osteoporosis. Bone. 2012 Jul;51(1):78-84.

4.1.1: Introduction

Osseous bone is a dynamic system naturally altering its microenvironment through osteolytic and osteoblastic processes throughout an individual's life. Factors that include lifestyle changes, pregnancy, hormonal status, disease and age can alter the homeostasis of bone resulting in increasing bone loss. This will lead to bone weakening and possibly orthopedic complications, such as fractures, that will have a direct effect on a patient's quality of life. Approximately 50% of women and 25% of men over age 50 will have osteoporosis-related fractures in their remaining lifetime [1] with 71% of patients over 90 years old showing signs of osteoporosis [2]. Osteoporosis is both a clinical as well as a financial burden with costs from osteoporosis-related fractures projected to reach 25.3 billion by 2025 [3]. Current clinical management of these patients is to continually evaluate bone mineral content in an effort to identify weakened limbs and avoid skeletal-related events (SRE).

Dual-energy X-ray absorptiometry (DXA), a planar imaging technique, is employed as a quantitative imaging tool for the diagnosis of bone mineral insufficiency [4-7]. This imaging method provides a highly accurate measure of bone mineral density with subjective spatial context. Quantitative measurements from DXA are typically obtained through summary statistics from a region of interest where inclusion of healthy bone with those showing weakening will attenuate the sensitivity at identifying early bone loss. Three-dimensional imaging techniques, such as computed tomography (CT), have led to the development of protocols to quantify local bone changes over time [8]. Although CT provides higher spatial detail over DXA, as of yet no

real clinical gains have been made as CT suffers from the same deficiencies when acquiring quantitative measurements of bone loss as DXA. With increasing therapeutic options for treating osteoporosis such as bisphosphonates and RANKL inhibitors, there is a clear unmet clinical need to identify early and locally weakened bones to circumvent the onset of SREs. With the correct tools, treatment decisions could be made quickly, based on imaging results, to individually optimize therapy and orthopedic correction surgeries.

Since its introduction in 2005, the parametric response map (PRM) when applied to quantitative imaging has been shown to improve the sensitivity at identifying early treatment response in cancer patients and is predictive of overall survival over what can be achieved using summary-statistical methods [9-15]. In brief, the PRM method involves spatially aligning serial pre- and mid-therapy quantitative images then individually classifying voxels based on the extent of change in the quantitative metric within the voxel. As such, the quantitative value within a tumor voxel may increase, decrease, or remained unchanged following treatment. Relative volumes of the three classifications are determined and used as outcome measures of response. At present, PRM has been demonstrated on different MRI-based quantitative imaging approaches, such as diffusion and perfusion MRI (in the case of diffusion MRI, PRM was referred to as the functional diffusion map) [10-18], as well as a variety of tumor types and locations [9-15, 17].

Although PRM analysis has been used exclusively for assessing therapeutic response in cancer, this technique may also offer a sensitive measure of bone tissue changes in patients suffering from bone loss, such as osteoporosis. To test its efficacy at identifying local changes in bone density resulting from an intervention (e.g. disease or treatment), we applied the PRM method to serially acquired CT data from a well-established rat model of osteoporosis [19, 20]. Animals were subject to ovariectomy (OVX) procedures, or sham for control, and legs were monitored weekly using CT imaging for four weeks following surgery. In the OVX model, it has been well documented that removal of the ovaries initiates bone degradation due to hormone deprivation that results in reproducible bone loss, characterized by site-dependent decreases in overall bone mass as well as diminished trabecular structure and cortical expansion [19, 20]. Volume fractions of increased Hounsfield unit (HU) value (PRM_{HU+}) or decreased HU value (PRM_{HU-}) as well as total bone volume (BV) and bone mineral density (BMD) were assessed temporally as clinically relevant measures of bone loss. After the fourth week of imaging,

animals were sacrificed and tibiae were harvested for μCT *ex vivo* imaging. We found that PRM_{HU-} was able to detect bone mineral changes in the OVX model as early as two weeks post-surgery while providing detailed spatial information on the extent and location of bone loss, while standard *in vivo* measurements of BMD changes based on statistical summary techniques were not detectable until 3 weeks post-surgery. Assessment of these clinically relevant measures of bone loss suggests that PRM may provide additional sensitivity as well as spatial information over standard approaches that can be used by clinicians for the early diagnosis of bone weakening and osteoporosis.

4.1.2: Methods

Animal model

Twelve female Sprague Dawley rats, 16 weeks old, were obtained from Charles River Labs and housed randomly in cages (2 per cage) fed with standard rat chow and tap water. Rats were randomly divided into ovariectomized (OVX, n=8) and sham-operated control (n=4) groups. When the rats were 17 weeks old, bilateral ovariectomy operation from a dorsal approach was performed on the OVX group, while surgery with no ovary removal was performed on the Sham animals. Ovariectomy was performed using standard protocols [21]. Briefly, animals were given 0.3 mg/kg buprenorphine pre-operatively and anesthesia was achieved using 5% isofluorane in 1 l/min oxygen until unconscious. The eyes were lubricated and all animals received a bolus dose of 5 ml warmed Lactated Ringers subcutaneously. Rats were then maintained on a warming table during surgery. The site of incision as shaved and then prepped using warm chlorhexidine and saline. Skin incisions were made from the second to fifth lumbar vertebrae on each side, about 2 cm in length, using a scalpel blade. The retroperitoneal incisions were made ventral to the rector spinae muscles just caudal to the last rib. The ovaries were exteriorized by gentle retraction, and then a 5–0 Vicryl suture was placed around the cranial portion of the uterus and uterine vessels followed by removal of the ovary, oviduct and a small portion of the uterus. Skin and peritoneum incisions were closed with 5–0 Vicryl sutures, and then rats were recovered under heat lamp until ambulatory. A second dose of buprenorphine was administered 8 h post-surgery and incisions were observed daily until fully healed. The animal experiments described in this study complied with all relevant federal and institutional policies.

μ Computed tomography (μCT)

In vivo imaging was performed on a Siemens Inveon system with the following acquisition parameters: 80 kVp, 500 μA, 300 ms exposure time, 501 projections over 360°, 49.2 mm field of view (FOV, 96.1 μm isotropic voxel size). Imaging was performed one day prior to surgery and days 6, 13, 20, and 27 post-surgery, capturing both tibiae as well as the distal femora of each rat. Right tibiae and femora were excised on day 28 post-surgery and stored in PBS-soaked gauze at −20 °C until *ex vivo* μCT imaging was performed.

Ex vivo μCT imaging was performed on a General Electric eXplore Locus SP system with the following parameters: 80 kVp, 80μA, 1600 ms exposure time, 400 projections, 0.5° per projection, 4 frames averaged per projection, 18 μm isotropic voxel size. For imaging, the sample was submerged in water, and X-rays were pre-filtered using 0.02" aluminum. Each image captured the proximal tibia, from the tibial head to about 20 mm distally.

In vivo image analysis

PRM analysis was performed using Matlab (Natick, MA) algorithms developed in-house. *In vivo* CT images were converted to Hounsfield units using a 0 HU phantom on each time point. All post-OVX image time points were registered to baseline images using mutual information as an objective function and simplex as an optimizer [22]. Registration was automatic and assumed rigid-body geometry, meaning rotation and translation only. Bone volumes of interest (VOI) were contoured on the baseline image using an automatic segmentation algorithm, selecting the tibia from the tibia/fibula junction to the proximal tibial head. Images were analyzed for bone volume fraction relative to total bone volume (BV/TV) and bone mineral density (BMD) using a threshold of 600 HU for selecting mineralized bone tissue. Parametric response maps of quantitative CT as expressed in Hounsfield units (PRM_{HU}) were generated over the same region by first calculating the difference between the Hounsfield units ($\Delta HU = HU_{post\text{-}surgery} - HU_{pre\text{-}surgery}$) for each voxel within the bone pre- and post-surgery. Individual voxels were classified based on the extent of change observed in ΔHU. Voxels yielding a ΔHU greater than a pre-determined threshold were designated red, decreased by more than the threshold were designated blue, and otherwise designated green (indicating no significant change from pre-surgery). Volume fractions of the total bone were calculated for the three classifications: PRM_{HU+} (red voxels denoting increased HU), PRM_{HU-} (blue voxels denoting decreased HU), and PRM_{HU0} (green voxels denoting unchanged HU). The threshold that designates a significant change in HU

within a voxel was empirically calculated from one random subject imaged twice on the same day, separated by an interval of one hour. Following registration and conversion to HU of the two images from the same animal, a linear least squares analysis was performed and the 95% confidence interval was determined for use as the PRM threshold, which was set as ± 391 HU.

Ex vivo image analysis

Ex vivo images were analyzed at week 4 post-surgery to verify that significant changes in bone microenvironment had occurred following ovariectomy in this well-established model of osteoporosis relative to sham animals. Images were analyzed using MicroView (GEHC). Trabecular VOI were drawn by hand and extrapolated between slices over a 3 mm-long region near the proximal tibia. Measures of mean trabecular thickness (Tb.Th), trabecular spacing (Tb.Sp), total bone volume (BV), bone volume fraction (BV/TV), mean bone mineral density (BMD), and structure model index (SMI) were analyzed. Cortical bone VOI were automatically delineated over the bottom four slices from the trabecular VOI. Measures of mean cortical thickness, cross-sectional area, and inner and outer perimeters were analyzed.

Data and statistical analysis

Data is presented as the mean ± the standard error of the mean (SEM). Differences in outcome measures between groups at each time point was determined by a two-tailed, unpaired Student's t-test with $p < 0.05$ denoting significance.

4.1.3: Results

Comparison of PRM_{HU} and standard whole-bone analyses

To assess the effectiveness of the PRM method at identifying bone loss we analyzed weekly μCT images using PRM compared to mean BV/TV and BMD between groups. Analysis was constrained to tibial bone from proximal tibial plateau distally to tibia/fibula junction segmented on the baseline image. The results in Figure 4.1.1 show that BV/TV and BMD were significantly different between groups by week 3. In the OVX group, BV/TV decreased by 3.1 ± 0.6% at the end of the study. BMD decreased by 4.2 ± 1.0% on week 3 but saw no further change the following week (week 4).

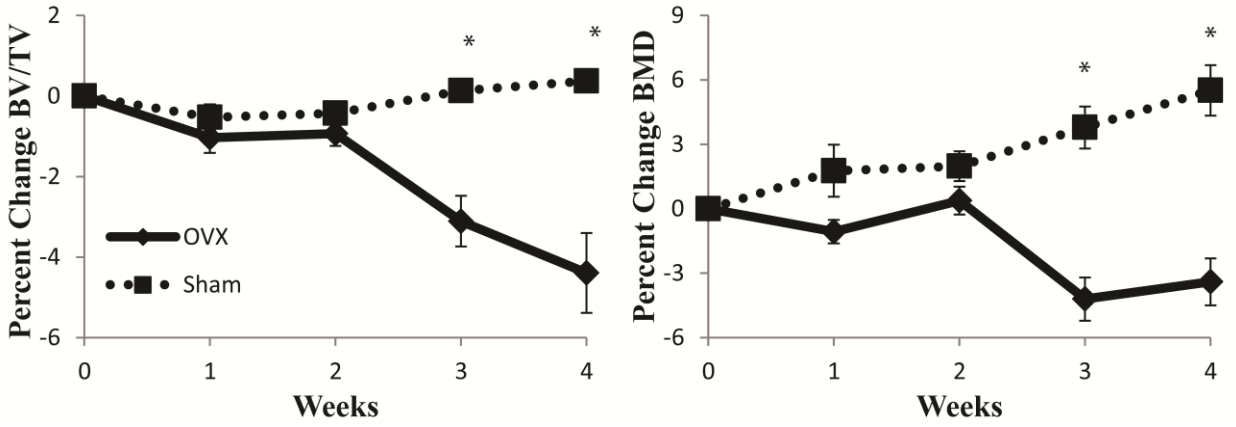

Figure 4.1.1: Plots of relative change in (A) bone volume fraction, BV/TV, and (B) bone mineral density, BMD, over the study time period. Quantitative values from registered images were determined from a volume-of-interest over the proximal tibial plateau distally to the tibia/fibula junction on baseline images. Differences between groups were not seen in either BV/TV or BMD until week 3 post-OVX, with decreases of 4.4±1.0% ($p=0.002$) and 3.4±1.1% ($p<0.001$), respectively, in the OVX group at the end of the study. Data is presented as group mean ± SEM. Significant difference between groups was assessed at $p<0.05$ and indicated by *.

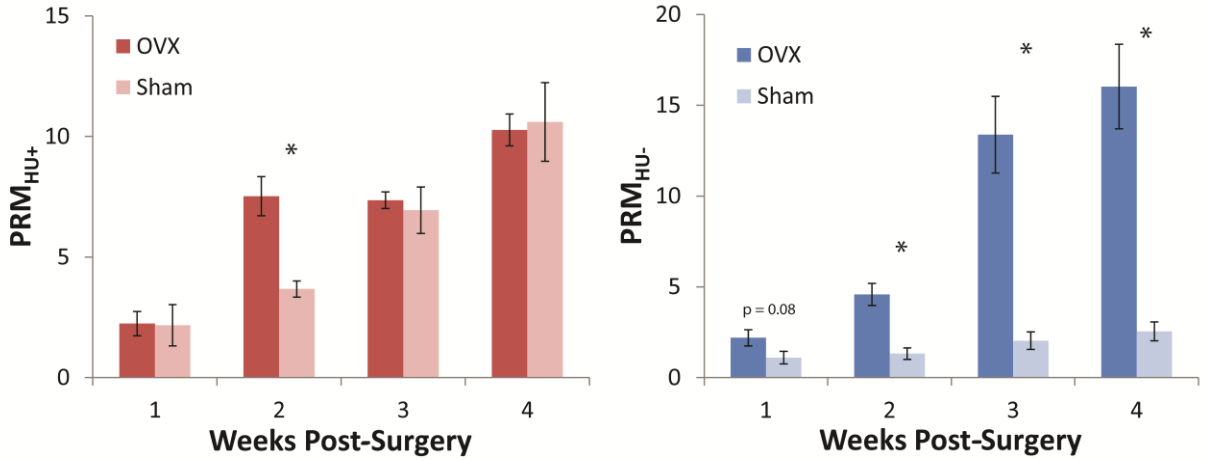

Figure 4.1.2: Bar plots showing the volume fraction of (A) increased HU, PRM_{HU+}, and (B) decreased HU, PRM_{HU-}. The OVX group showed a significant increase in PRM_{HU+} on week 2 which disappeared at later time points and a progressive increase in PRM_{HU-} until the end of the study. For week 1 PRM_{HU-}, group differences were nearly significant, with $p=0.08$. Data is presented as a group mean ± SEM. Significant difference between groups was assessed at $p<0.05$ and indicated by *.

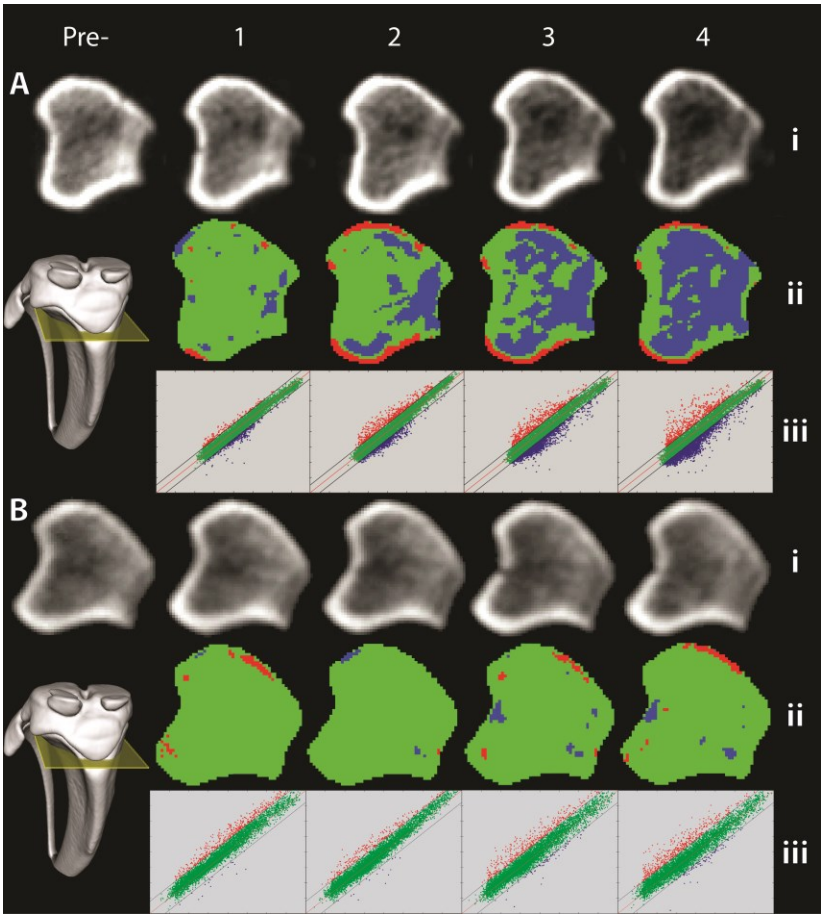

Figure 4.1.3: Representative PRM images from (A) an OVX animal and (B) a sham animal, displayed as an axial slice over time (from left to right: weeks 0 to 4, respectively). The position of the slice shown is indicated by the yellow box on the surface rendering to the left of the PRM results. For each representative animal, (i) grayscale images, (ii) PRM overlays, and (ii) PRM scatterplots of individual voxel changes show a decrease in cancellous bone mineral over time (blue in the PRM).

Ex vivo μCT measurements of tibial trabecular and cortical bone

The PRM method, with spatial sensitivity, revealed trabecular bone loss as well as cortical expansion in the OVX group. Figure 4.1.2 shows PRM analysis with a representative axial slice through the CT image (i–ii) and the scatter plot with pre-surgery HU on the x-axis and post-surgery HU at a specific time on the y-axis for the entire VOI (iii) over the study time period. The representative slice shown near the proximal tibial plateau was chosen to include changes in both trabecular and cortical bone. Trabecular degradation is apparent in the OVX animal, PRM_{HU-}, seen as blue in the PRM overlay and scatterplot. Also in the OVX group, PRM_{HU+} (red voxels) indicates a shift in the cortical bone outward, reflecting cortical expansion.

These two changes in bone structure are typical of this osteoporosis model [19]. In contrast to the OVX animal, the sham animal had very little change in PRM metrics. The few red and blue pixels observed were the result of natural bone growth and reflected modeling changes associated with skeletal growth.

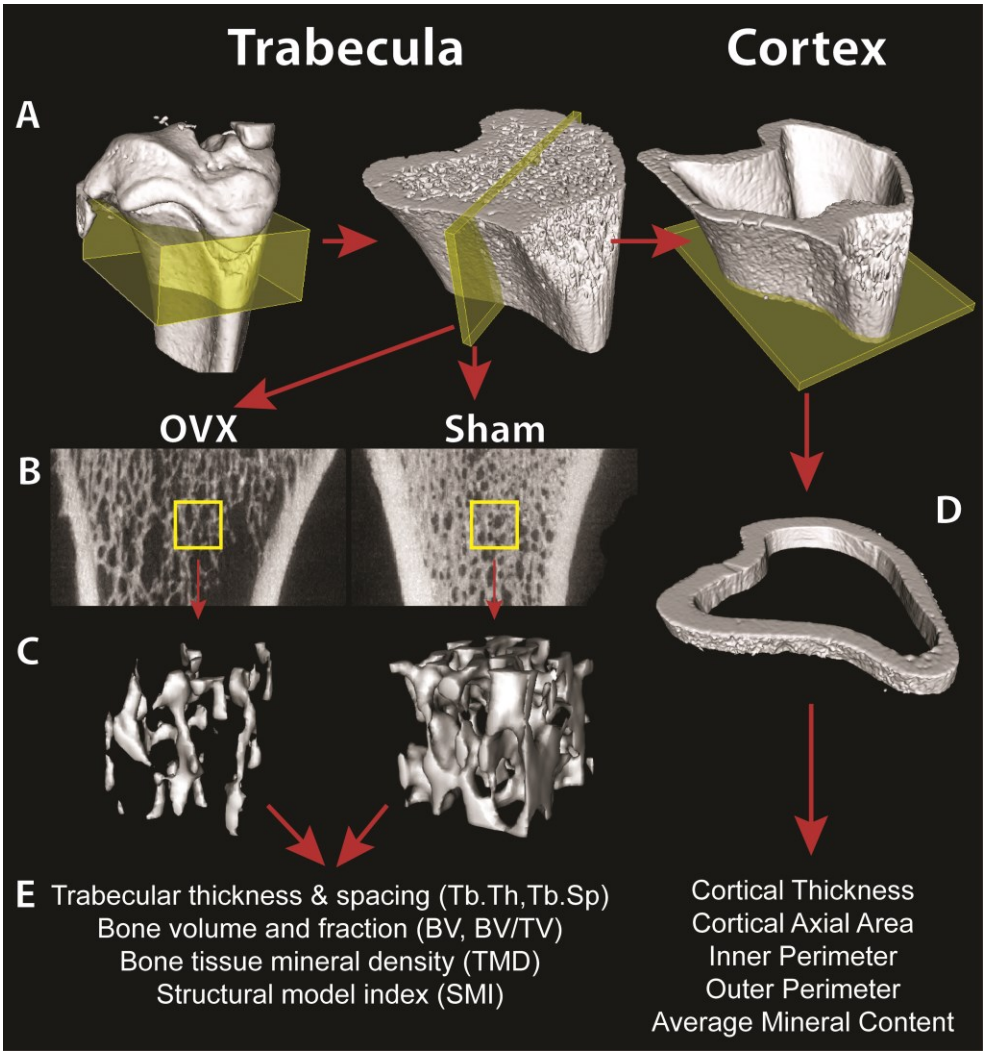

Figure 4.1.4: Representative images of *ex vivo* images of proximal tibiae four weeks post-surgery. (A) Surface renderings show regions used for *ex vivo* analysis (yellow boxes) of trabecula (left) and cortex (right). (B) Maximum intensity projections from a middle slab (200μm thick) show a clear difference between OVX and Sham animals. (C) Surface renderings of OVX (Left) and Sham (Right) trabecular bone (location indicated by yellow box in B) show a significant drop in trabecular structure following OVX surgery. (D) Surface rendering of region used for cortical analysis, excluding the trabecular region. (E) Parameters obtained from trabecular (left) and cortical (right) analyses.

Table 4.1.1: *ex vivo* Trabecular Bone Analysis.

Group	Tb.Th (μm)	Tb.Sp (μm)	Volume (mm^3)	BV/TV	BMD (mg/mm^3)	SMI
OVX	50.8 (1.94)	173 (16.5)	8.6 (0.62)	0.29 (0.021)	363 (16.7)	1.57 (0.14)
Sham	73 (4.03)	65.3 (10.87)	14.2 (0.88)	0.6 (0.045)	564 (25)	-2.16 (0.858)
p-value	**0.0058**	**0.0003**	**0.0019**	**0.0026**	**0.0007**	**0.021**

* Data are shown as means, with standard error in parentheses, for trabecular thickness and spacing (Tb.Th and Tb.Sp, respectively), bone volume (BV), bone volume ratio (BV/TV), bone mineral density (BMD), and structural model index (SMI).

Table 4.1.2: *ex vivo* Cortical Bone Analysis

Group	Thickness (mm)	Area (mm^2)	Mineral (mg)	Inner Perimeter (mm)	Outer Perimeter (mm)
OVX	0.45 (0.014)	4.51 (0.164)	0.1 (0.002)	11.1 (0.28)	17.2 (0.2)
Sham	0.53 (0.013)	4.86 (0.067)	0.102 (0.0026)	9.7 (0.34)	15.3 (0.51)
p-value	**0.0023**	0.0815	0.5329	**0.0166**	**0.0278**

* Data are shown as means, with standard error in parentheses.

The mean volume fractions, PRM_{HU+} and PRM_{HU-}, from both groups were monitored over the study time period (Figure 4.1.3). The PRM_{HU+} results showed a temporary increase on week 2 over control values. This significant difference was lost after week two indicating a transient remodeling effect on OVX animals. The PRM map shows that the majority of PRM_{HU+} is along the bone's outer edge, indicating that this increase is due mainly to cortical expansion. The subsequent loss of significance between groups is likely normal bone growth in the sham group catching up with the remodeling effect in the OVX group. The PRM_{HU-} plot (Figure 4.1.3B) reflects progressive bone loss which is characteristic of this animal model, with significantly higher PRM_{HU-} values observed in OVX than sham animals at all time-points after week 1 post-surgery. As shown in Figure 4.1.2, PRM_{HU-} voxels are primarily found in the cancellous bone space and indicate loss in trabecular bone mass. The increase is nearly significant even at the week 1 imaging time point ($p=0.083$). By the end of the study, at 4 weeks post-surgery, OVX and sham groups resulted in bone loss as measured by PRM_{HU-} of 16.0% (± 2.3) and 2.5% (± 0.8), respectively ($p < 0.001$).

To verify that OVX animals had undergone extensive bone loss following surgery relative to sham, we performed *ex vivo* μCT after 4 weeks on all animals in the study. Images were acquired with 18 μm resolution allowing quantification of trabecular structures. Figure

4.1.4 illustrates the process of analysis for both trabecula and cortex, with resulting measurements. Figure 4.1.4A indicates the location of the trabecular analysis slab (left), region for maximum intensity projection (MIP) in B (middle), and slab for cortical analysis (right) as a yellow box. Figure 4.1.4B shows representative MIP images for OVX and sham animals, with a clearly lower trabecular bone mass in the OVX animal. Figure 4.1.4C shows representative isosurfaces for the two groups, taken from the yellow region indicated in B. Figure 4.1.4D shows an isosurface of the cortical bone from a representative animal, which was used for cortical analysis. Resulting measurements are listed in Figure 4.1.4E, and group means are shown in Tables 4.1.1 and 4.1.2 for trabecular bone and cortical bone, respectively. Significant differences were seen between groups in all trabecular measurements, indicating degradation of trabecular structure. Structural model index (SMI) measurements quantify the extent of rod- or disk-like shaping of the trabecular lattice, with higher values indicating more rod-like and lower indicating more disk-like shaping. Cortical measurements of average thickness, inner, and outer perimeters also showed significant differences between groups. Larger perimeters and decreased cortical thickness in the OVX group indicate significant cortical expansion, which is consistent with this model. No significant change in cross-sectional area indicates that remodeling occurred without significant loss of total cortical bone.

4.1.4: Discussion

The goal of this study was to evaluate voxel-based PRM analysis of bone mineral changes using *in vivo* μCT and compare these results to those determined using conventional measures of bone mineral density and bone volume. Toward this end we used a well-documented model of osteoporosis in rats in which removal of the ovaries initiates bone degradation due to hormone deprivation. This animal model has been shown to result in highly-reproducible bone loss, characterized by site-dependent decreases in overall bone mass as well as diminished trabecular structure and cortical expansion [19, 20]. Clinical osteoporosis is characterized by decreases in either bone mineral density (BMD) or bone mineral content (BMC) of over 2.5 standard deviations below the young adult reference mean (−2.5 T-score), which leads to increased fragility and consequently a greater risk of SREs [19]. It is reported that the earliest time of statistically detectable cancellous bone loss is approximately 14 days post-OVX in this animal model [19, 23]. In this study, PRM showed a near-significant change in PRM_{HU-} by one

week post-surgery, which became significant 2 weeks post-OVX, well before any significant difference in BMD was detected. In addition to being an early biomarker of bone remodeling, PRM also provided locally-resolved spatial information revealing bone degradation and growth which was not attainable by BMD measurements.

Historically, the most utilized method of tracking bone mineral changes *in vivo* has been dual-energy X-ray absorptiometry (DXA). This method, although highly accurate in its measurements, is limited in its ability to provide spatial information. The attractiveness of DXA in most cases is its measurement accuracy as well as its minimal exposure to ionizing X-rays. Doses from quantitative CT imaging can be hundreds of times higher than DXA, but provide 3D voxel sizes able to resolve bone micro-structures. Despite the widespread usage of BMD, recent studies have indicated that measurement of BMD alone is insufficient for evaluation of bone strength [24-27]. Recent studies have explored the use of high resolution CT imaging to model bone mechanical characteristics in order to predict fracture risk through finite element analysis (FEA) [25, 28-30]. Until recently, mechanical properties of bone were tested *ex vivo*, requiring the use of a large number of animals to provide sufficient data points. Several recent studies have shown great accuracy in predicting fractures in femoral and vertebral cases using FEA [29, 31]. However very powerful computing hardware is necessary for this technique, especially when using nonlinear modeling strategies and the constraints and limitations in application are not yet fully understood. Using the spatially resolved bone changes obtained from PRM analysis, evaluation of increased fracture risk may be predictable without such rigorous computational modeling making this technique more clinically relevant. PRM has the capability of monitoring global bone mass changes as well as identification of focal bone loss which would otherwise be attenuated in global bone measurements that use summary statistical methods (e.g. mean value over a region of interest). For this reason PRM may provide a better foundation for determining correctional orthopedic strategies.

The tradeoff between resolution and imaging time (and therefore radiation dose) is well known. For the purposes of this study and its future clinical implications, image resolution was sacrificed in order to prioritize low radiation doses, below known tissue response limits [32, 33]. Due to the lower resolution of our *in vivo* measurements, quantification of such trabecular parameters as thickness, spacing, and SMI were not feasible. The voxel-wise comparison of HU in PRM, however, was able to detect loss in trabecular bone structure as a decrease in HU rather

than the loss in binary threshold bone volume that is typically monitored in higher resolution *ex vivo* images. PRM maps are also able to spatially resolve these changes in 3Dspace, allowing for focal changes in bone mineral density to be identified and quantified.

Previous studies have reported results from using a longitudinal voxel-wise comparison approach, similar to PRM, to subjectively show spatial changes in bone mass *in vivo* [34-36]. Even though these studies performed voxel-wise comparison, it was used only for qualitative presentation and not quantified statistically. Schulte et al. [8] used registered high resolution μCT to extrapolate measures of bone formation and resorption rates in the trabecula of mouse vertebrae. The study focused primarily on bone histomorphometry and the processes of bone adaptation, and would result in high doses of ionizing radiation (IR) to achieve the level of resolution necessary, therefore the approach was not designed for clinical application. Since PRM compares quantitative Hounsfield units and not binary bone images it is able to detect bone structural changes without requiring excessively small resolution (and thus high IR doses). The experiments presented here are the first to use PRM to quantify voxel-based changes in bone mass *in vivo*.

Although PRM was demonstrated here on a model of osteoporosis, PRM analysis may have wider clinical applications. Bisphosphonates, used clinically for several years, inhibit the resorption of bone by osteoclasts [37]. Interestingly, the degree of fracture risk reduction following bisphosphonate therapy is not well explained for by changes in bone mass alone. Following 1 year of Risedronate therapy in 2087 individuals, Watts et al. [38] found that fracture risk reduction was not dependent on change in BMD, indicating that other factors such as remodeling of bone geometry, etc. must play significant roles. PRM analysis may provide a sensitive biomarker of bone response to these therapies, leading to prediction of overall outcome by direct observation of local sites of anabolic or anti-catabolic effect. Another application of PRM is in the assessment of bone response to metastatic cancer [35] where diseases characterized by low bone mass and deterioration of microarchitecture often lead to bone fragility [5, 19, 39]. Skeletal metastases develop in approximately 70–80% of patients with breast or prostate primary cancer, with over 250,000 and 100,000 deaths worldwide each year from breast and prostate cancer, respectively [40]. Cancer that has metastasized to the bone may present osteolytic, osteoblastic, or a mix of these characteristics. Patients presenting with these diseases have a high risk of incurring fractures, resulting in patient pain and increased morbidity.

Local changes in bone mass due to metastatic disease can significantly impact the mechanical integrity of the skeleton, leading to focal sites of high fracture susceptibility [41]. PRM analysis may provide a unique and sensitive measure in differentiating the osteoblastic and osteolytic sites which would be highly valuable in strategizing corrective therapy based on local fragility. Recent studies have uncovered a close interaction between bone and cancer metastases through molecular signaling [42], in which growth of the cancer is highly dependent on the remodeling of the surrounding bone. PRM_{HU} analysis may also prove clinically useful in the identification of initial forming micro-metastases in the bone and in assessing treatment efficacy for targeted therapies that disrupt the molecular signaling between bone and cancer.

In conclusion, PRM proved highly sensitive in the detection and spatial localization of bone mass changes resulting from osteoporosis. Spatial identification of focal sites of bone loss over time will provide many new opportunities for clinical application. The voxel-wise analysis of registered serial data is a highly flexible tool, and can be applied to a variety of bone disease pathologies to provide for detection of spatially varying changes in CT skeletal images over time.

4.2: PRM Detection of Bone Metastasis Response

4.2.1: Introduction

Prostate cancer is a leading cause of death in men, with the highest overall incidence rate [43] and the majority of fatal cases resulting from metastatic disease. Approximately 90% of patients presenting with advanced prostate cancer develop bone lesions [44]. At present there are no approved methods for quantifying treatment response in boney metastases. Although quantification of systemic plasma levels of prostate-specific antigen (PSA) has shown promise as a surrogate biomarker of treatment response, it has not been validated in clinical trials as a reliable predictor of patient survival. The high prevalence of this disease and lack of quantitative readouts of treatment response highlight the need for new imaging and analysis strategies for the evaluation of metastatic bone disease.

Metastatic bone lesions may affect the surrounding bone by either breaking it down (osteolytic) or building/remodeling (osteoblastic), both of which may result in compromised bone structure and risk of skeletal-related events. The dependence of metastatic tumor growth on its local environment is well documented. Tumor-stroma interaction in the case of bone

metastases relies heavily on the release of bone-derived Transforming Growth Factor (TGF-) β through tumor-initiated bone erosion and remodeling [45]. This interaction has spurred interest in developing therapies that treat not only the tumor, but the bone as well. As understanding of the cellular mechanisms of this cancer growth, new treatment strategies are continually under development. It is also now apparent that assessment of treatment response may benefit greatly from evaluation of both soft-tissue tumor changes as well as changes in the tumor micro-environment. For bone metastases this would mean detecting bone density changes, for which x-ray CT imaging is well-equipped.

The PRM method has shown promise in detecting soft-tissue changes after chemotherapy in apparent diffusion coefficient (ADC) maps [9-11, 14-16, 46], and more recently in bone density changes, as changes in Hounsfield units (HU), in a well-established animal model of osteoporosis (Chapter 4.2.1, [47]). The OVX animal model produced predictable systemic bone mineral density decreases which were detected very early after ovariectomy by PRM_{HU}. One of the great strengths of PRM analysis, however, is its ability to detect localized changes. Most bone changes due to metastatic involvement occur at the border of the lesion. PRM analysis, applied to CT images of bone metastases, may provide an invaluable tool for assessing localized response to treatments targeting the tumor-stromal interaction.

In this study, PRM_{HU} was evaluated as a biomarker for assessing bone response to treatments targeting either the bone (zoledronic acid, ZA) or the tumor (docetaxel). Two prostate cancer cell lines, with distinctly different osteolytic/osteoblastic activity, were used to evaluate PRM at detecting early bone turnover following metastases and treatment by either ZA or docetaxel. The results showed that PRM_{HU} analysis provided early predictive value in assessing response to both of these treatments and in both tumor models. A clear distinction between the two cell lines was also present, which may provide useful insight into the behavior of an individual lesion. PRM results also correlated well with measurements of tumor volume and water diffusion changes in the tumor. In conclusion, PRM_{HU} analysis shows a high potential for evaluation of boney metastasis.

4.2.2: Methods

Tumor Models

The internal University Committee on Use and Care of Animals (UCUCA) approved the experimental protocols used for this study. Before implantation, cells were harvested by trypsinization, counted, and re-suspended in serum-free medium for injection. Male severe combined immune-deficient (SCID) mice were implanted with intra-tibial injections of or $5x10^5$ in 10µl at about 4-6 weeks of age as previously described (p.64). Animals were maintained according to the NIH standards established in the "Guidelines for the Care and Use of Laboratory Animals".

PC3: Osteolytic Prostate Cancer

Androgen independent (hormone refractory) human prostate cancer (PC3) cells were initiated from a bone metastasis of a grade IV prostatic adenocarcinoma from a 62-year-old male Caucasian. PC3 cells were transfected with a luciferase-encoding pLazarus retroviral construct using Fugene 6 (Roche Applied Science, Indianapolis, IN) per manufacturer's instructions.

LAPC-9: Osteoblastic Prostate Cancer

LAPC-9 xenografts were derived as previously described [48, 49]. The clinical material was propagated as sub-cutaneous xenografts in SCID mice until implantation [50].

Treatments

Zoledronic Acid

The effect of zoledronic acid (ZA, LKT Laboratories, St. Paul, MN) treatment was evaluated on an early-metastasis PC3 tumor model (n=9) and compared to controls (n=4, treated with a equivalent volume of PBS). For those mice implanted with PC3, treatment was administered subcutaneously in doses of 5mg/kg twice weekly for four treatments, starting three days post-implantation, immediately after imaging.

Docetaxel

The effect of docetaxel (Taxotere, Sanofi-Aventis, Bridgewater, NJ) was evaluated on the LAPC-9 established tumor model (treated: n=3; controls: n=6). Mice were administered a single intraperitoneal dose of 20mg/kg in 10% DMSO solution. Treatments were administered starting when tumor volumes, as measured by anatomical MRI, reached 7-15mm^3. For the purposes of this manuscript, the day of the first treatment administration will be referred to as day 0.

Imaging

μComputed Tomography

Imaging of the early-metastasis PC3 animals were imaged on days 0, 3, 7, and then weekly post-implant, and LAPC-9 animals were imaged weekly. μCT images were acquired using a Siemens Inveon system with the following parameters: 80 kVp, 500 μA, 300-ms exposure, 501 projections over 360 degrees, and 49.2-mm field of view (56-μm voxel size).

MRI

MRI was performed using a 9.4-T, 12-cm horizontal bore DirectDrive System (Agilent Technologies, Palo Alto, CA) with a quadrature mouse head coil (m2m Imaging Corp, Cleveland, OH). Images of the tumor-bearing leg were acquired twice weekly starting from the day before treatment initiation. Diffusion-weighted images were acquired using a spin-echo sequence with navigator echo motion correction and gradient waveforms sensitive to isotropic diffusion [51] using the following parameters: repetition time/echo time = 4000/37 ms, field of view = 20 × 20 mm, matrix size = 128 × 64, slice thickness = 0.5mm, slice number = 25, and b-values (diffusion weighting) of 120 and 1200s/mm^2. Following image acquisition, data that included manually drawing volumes of interest on the high diffusion-weighted image to compute tumor volumes and diffusion values were stored for analysis. Tumor volumes and apparent diffusion coefficient (ADC) values were quantified over time to monitor tumor burden and cellularity, respectively.

Image Analysis

Volumes-of-interest (VOI) were generated using image thresholding to encompass the bone volume (including marrow/trabecular space) surrounding the tumor location, specifically the tibia from tibial plateau to tibia/fibular junction.

Parametric response maps (PRM) were generated by first co-registering post-treatment images to corresponding pre-treatment images, and then each image voxel was categorized into one of three groups: increase (PRM_{HU+}, red), decrease (PRM_{HU-}, blue), or no significant change (PRM_{HU0}, green). Image co-registration was performed using an automated iterative image warping algorithm with a cost function of mutual information (MIAMI Fuse™, University of Michigan). A voxel value change was considered significant (red or blue category) if |ΔHU| was

greater than 391 HU. This cutoff was pre-determined as the 95% confidence interval for these models.

Statistics

Significant difference between groups was assessed using an unpaired Student's t-test with $p < 0.05$, and designated with an asterisk on plots. All data on plots are presented as mean ± standard error of the mean (SEM).

4.2.3: Results

Treatment with zoledronic acid administered early in the establishment of PC3 intra-tibial tumors resulted in bone protection from the tumor's osteolytic activity and resulting retardation of tumor growth (Figure 4.2.1A), with significantly smaller tumors than ZA treatment animals at 3 weeks post-implantation ($p=0.005$). Control tumors were un-inhibited in their bone erosion, as seen in Figure 4.2.1 B-top and D as progressive increase in PRM_{HU-} (blue). In contrast, animals treated with ZA showed a marked increase in bone density as indicated by PRM_{HU+} (red) (Figure 4.2.1B-bottom and C) with no significant increase in PRM_{HU-} (Figure 4.2.1D). Surface renderings of the tibiae from control animals (Figure 4.2.1B) show the progressive deterioration of the bone leading to nearly complete bone destruction in the vicinity of the implant site. Three weeks post-implantation, water diffusivity in the tumor, as quantified as ADC, was significantly lower in the ZA group than controls ($p=0.036$), however due to the very small size of the lesions and limitations in image resolution this may simply be a partial-volume effect. Although not significant at 3 days post-treatment initiation, animals treated with ZA were found to have substantially higher bone density than controls as determined by PRM_{HU+} ($p=0.06$). A significant difference between groups was reached at one week post-treatment initiation. An increase in bone density was also observed in the non-tumor-bearing tibiae, with a significant difference between groups at two weeks post-treatment ($p=0.013$, not shown).

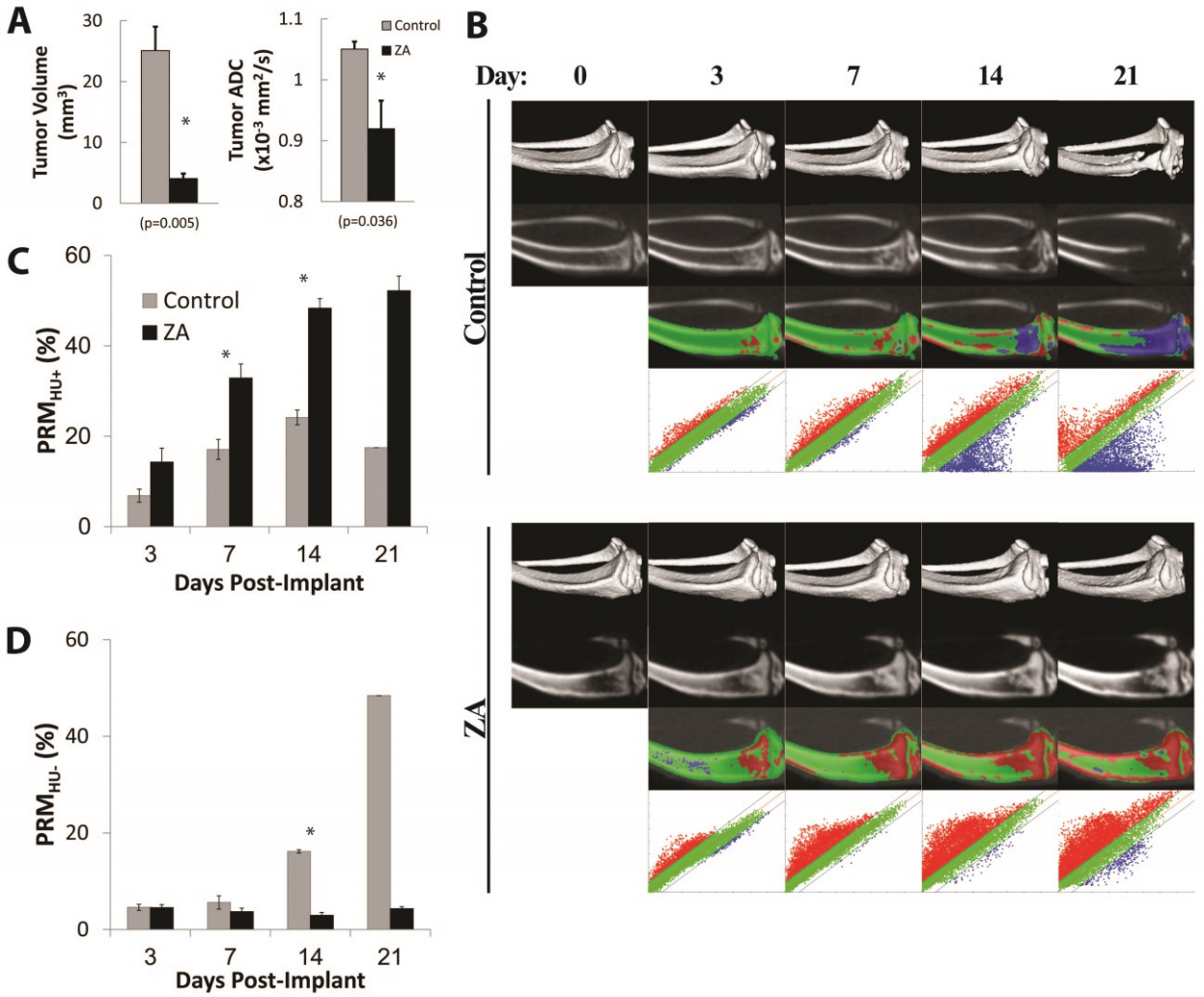

Figure 4.2.1: PC3 implantations treated with zoledronic acid show a bone-protective effect. (A) MRI tumor volume and ADC determined at day 21 post-treatment-initialization shows a retardation of tumor growth and significantly lower ADC in the zoledronic acid treated animals. (B) Representative images for a control (top) and ZA-treated (bottom) mouse showing (from top to bottom) an isosurface, CT slice, PRM overlay, and PRM scatterplot from pre-treatment to 21 days post-treatment. (C) PRM_{HU+} bar plot shows significantly higher volume of bone that increased in density after treatment compared to controls. (D) PRM_{HU-} bar plot shows minimal loss of bone in the ZA-treated group, compared to progressively increasing bone loss in the controls.

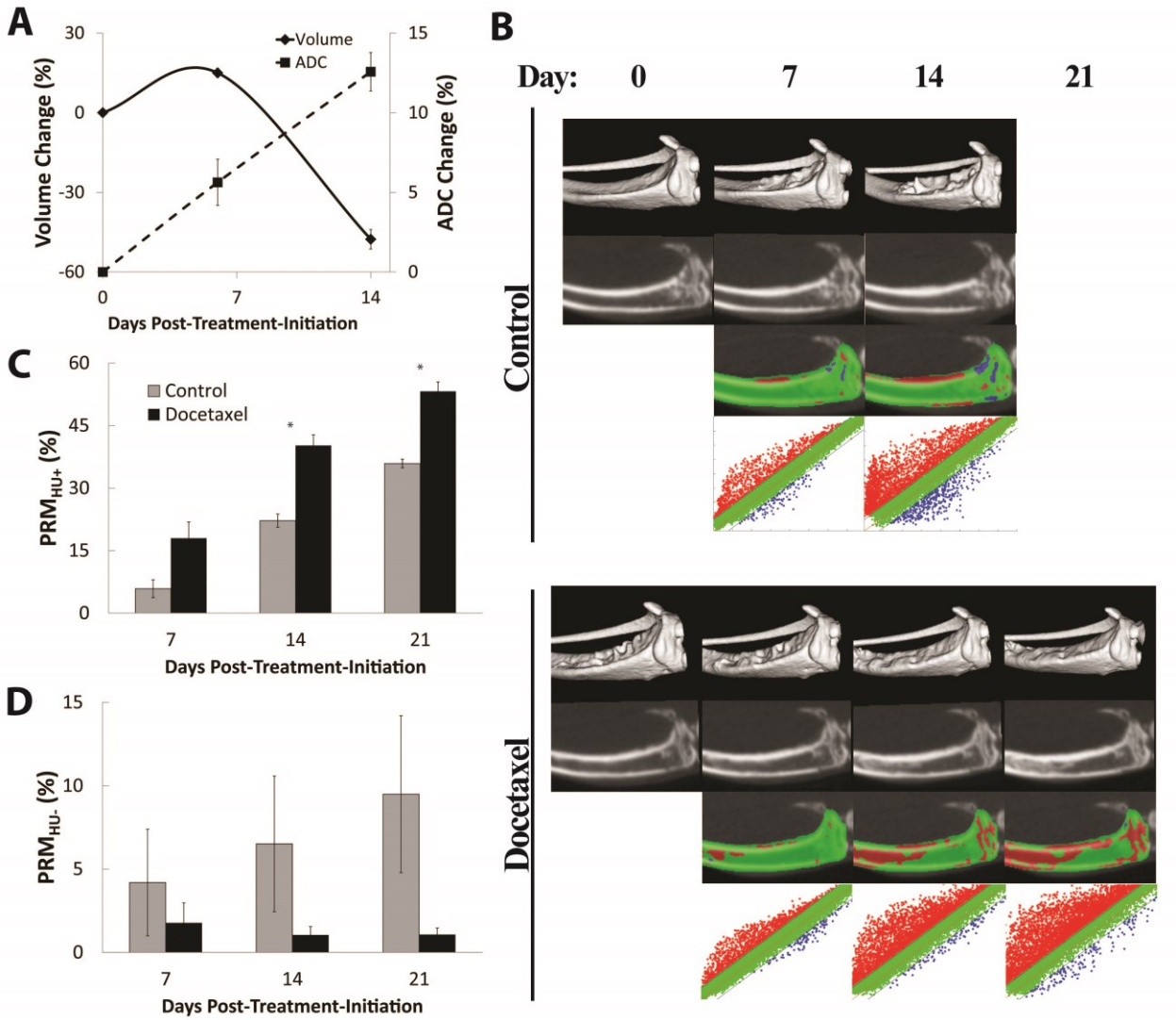

Figure 4.2.2: LAPC-9 tumors showed a slower mixed $PRM_{HU+/-}$ response with docetaxel treatment compared to PC3. (A) Time plots of tumor volume (solid line) and ADC (dashed line) show successful response to treatment as volume shrinkage and ADC increase. (B) Representative images for a control (top) and docetaxel-treated (bottom) mouse showing (from top to bottom) an isosurface, CT slice, PRM overlay, and PRM scatterplot from pre-treatment to 21 days post-treatment. (C) PRM_{HU+} bar plot over time shows more bone density increase in the docetaxel-treated group compared to controls, significant on days 14 and 21. (D) PRM_{HU-} bar plot over time shows very little bone loss in the treated group compared to elevated bone mineral loss in the controls (though not significant in this study).

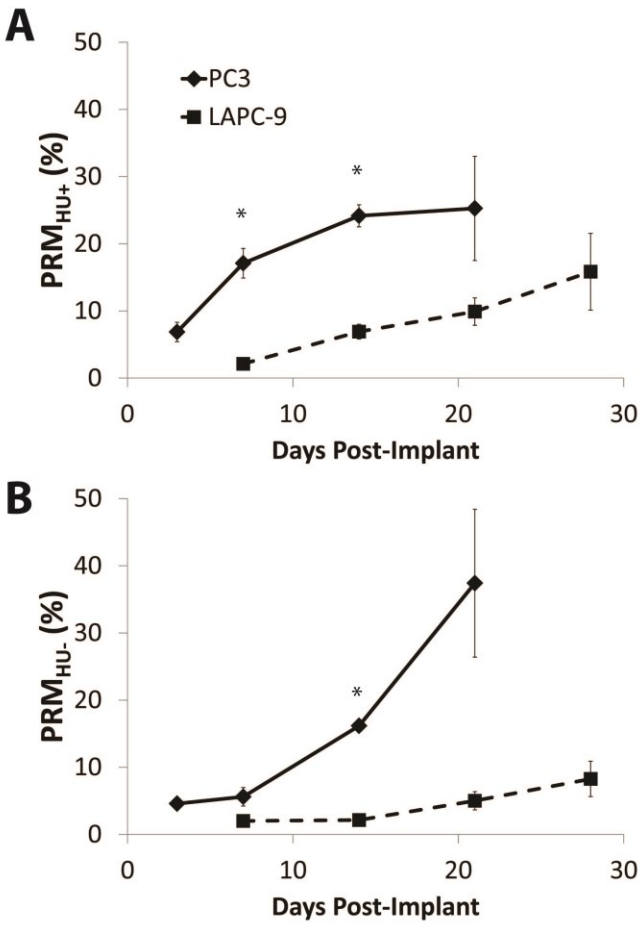

Figure 4.2.3: PRM_{HU} plots over time compare un-treated bone changes in PC3 (diamonds, solid line) to LAPC-9 (squares, dashed line) intra-tibial tumors as quantified by (A) PRM_{HU+} and (B) PRM_{HU-}. Significant difference between groups is denoted by an asterix, *.

Chemotherapy of the established LAPC-9 tumor model resulted in bone normalization following tumor therapeutic response (Figure 4.2.2). Tumors were observed to show a substantial drop in volume (48 ± 3.7% by week two) and increase in ADC (13 ± 1.2% by week two) characteristic of an effective treatment (Figure 4.2.2A). PRM_{HU} analysis (Figure 4.2.2B-D) revealed mixed bone remodeling due to the tumor's known osteolytic and osteoblastic activity, with progressive increases in both PRM_{HU+} and PRM_{HU-} in the control group. Chemotherapeutic intervention in this model resulted in higher values in PRM_{HU+}, significant at week 2 ($p=0.007$), and a general decline in PRM_{HU-}. Surface rendering of the tibiae (Figure 4.2.2B) shows progressive deformation of the bone in the control group as the tumor grows. In contrast, tibiae

from treated animals were found to have re-normalization of the bone structure. No significant differences in PRM_{HU-} were found between groups due to the wide variance in the controls.

PRM results from control (i.e. untreated) animals were also compared between PC3 (osteolytic) and LAPC-9 (mixed osteolytic/-blastic) tumor models to contrast the different phenotypes (Figure 4.2.3). The PC3 tumor model elicited an approximately exponential increase in PRM_{HU-} as a result of substantial bone loss, mirroring the expected growth of the tumor (time-course volume data not obtained). Both PRM readouts for the PC3 model were significantly higher than the LAPC-9 model (PRM_{HU+}: $p=0.003$ at 1 week and $p=0.001$ at 2 weeks; PRM_{HU-}: $p<0.001$ at 2 weeks).

4.2.4: Discussion and Conclusions

The purpose of this study was to evaluate the PRM method on CT images of boney metastasis. Two tumor models were evaluated: one highly osteolytic model highlighting early establishment of metastases (PC3) with bisphosphonate intervention, and the other a mixed-phenotype model (LAPC-9) with chemotherapeutic intervention of well-established tumors. Both are prostate cancer cell lines, but have greatly differing characteristics. The breast cancer cell line previously reported in this manuscript was also considered for comparative analysis; however initial analyses were problematic due to the rapid tumor growth fragmenting the bone instead of eroding. For this reason, the 1833 model was considered sub-optimal for the purposes of this study and was not included.

The PC3 cell line is well-documented and known to exhibit highly osteolytic behavior. Bone erosion, measured by PRM_{HU-}, in untreated lesions exhibited an exponential trend, assumed to follow the growth of the tumor. PRM_{HU+} also showed a significant increase in the controls, which may be attributed to a combination of (1) bone healing from the initial cell implantation, (2) bone remodeling away from the lesion due to the loss of structural integrity around the lesion, (3) the elevated levels of mineral available in the bone environment due to the erosion around the lesion, (4) natural bone growth due to the young age of the mice and (5) a combination of the above processes. This effect may be mitigated by selecting bone regions only in the immediate vicinity of the tumor instead of a fixed length of bone. Treatment with ZA, however, had a drastic effect on the bone, increasing bone density throughout the tibia and resulting in significantly elevated levels of PRM_{HU+} over controls and very little PRM_{HU-}.

Although this bone-targeted therapy was not able to completely stop tumor growth in this model, it did greatly inhibit tumor growth, resulting in smaller lesions after three weeks. Although ADC values were significantly diminished in the treated tumors, this difference may have simply been a result of partial-volume effects due to the small size of the lesions. PRM analysis was nearly able to capture these effects three days post-treatment (PRM_{HU+}, significant at one week). The corresponding PRM overlay was also useful in localizing bone changes, with a large region of blue apparent (PRM_{HU-}) in the tumor region of control animals compared to the red region in the ZA group (PRM_{HU+}) corresponding to healing from the implantation burr hole.

LAPC-9 tumors are also well-established, but are known to grow much slower than PC3 tumors and exhibit both osteolytic and osteoblastic behaviors, resulting in more bone remodeling than bone loss. This can be seen in the PRM results for the control group (Figure 4.2.2C-D), with progressively increasing fractions of both PRM_{HU+} and PRM_{HU-}. A chemotherapeutic response is observed as a decrease in tumor volume and an increase in ADC in the treatment group. In addition, an apparent shift in bone remodeling toward PRM_{HU+} and almost zero PRM_{HU-} is also suggestive of a treatment induced response. The high percentage of PRM_{HU+} and low PRM_{HU-} is indicative of a progression from the disorganized state of the bone that resulted from tumor involvement back toward the natural stromal structure. The observed elevated values of PRM_{HU+} in the treated group persisted throughout the time course of the study as consequence of the already significantly remodeled bone (significant tumor volumes) at baseline that is required for MRI analysis.

In comparing LAPC-9 to PC3 PRM_{HU} results, only data that was acquired without any treatment was used (data from treatment groups were included until the first post-treatment time point) and day 0 refers to the day of cell implantation. The slower growth of LAPC-9 tumors is apparent in the slow and steady increases in both PRM_{HU+} and PRM_{HU-} compared to PC3. Future results may be clarified by the use of older mice whose bones are not still growing and possibly a less-damaging tumor implantation method to avoid the natural growth and healing effects present in the current study.

In conclusion, this study presents clear evidence of the utility of PRM analysis for detecting bone changes due to varying phenotypes of boney metastasis and their treatment strategies. Spatially delineated characterization of bone changes using PRM is able to show localized treatment response in order to better understand the mechanisms and side-effects of its

actions. PRM methodology may be applied to bone analysis in both clinical patients and pre-clinical studies to enhance the quantitative readouts of bone change.

4.3: References

[1] Fast Facts. National Osteoporosis Foundation. August 29 2011. http://www.nof.org/node/40.

[2] Krestan CR, Nemec U, Nemec S. Imaging of insufficiency fractures. Semin Musculoskelet Radiol 2011;15: 198-207.

[3] Burge R, Dawson-Hughes B, Solomon DH, Wong JB, King A, Tosteson A. Incidence and economic burden of osteoporosis-related fractures in the United States, 2005-2025. J Bone Miner Res 2007;22: 465-75.

[4] Ammann P, Rizzoli R, Slosman D, Bonjour JP. Sequential and precise in vivo measurement of bone mineral density in rats using dual-energy x-ray absorptiometry. J Bone Miner Res 1992;7: 311-6.

[5] Honig S. Osteoporosis - new treatments and updates. Bull NYU Hosp Jt Dis 2010;68: 166-70.

[6] Jacobson JA, Jamadar DA, Hayes CW. Dual X-ray absorptiometry: recognizing image artifacts and pathology. AJR Am J Roentgenol 2000;174: 1699-705.

[7] Lorente-Ramos R, Azpeitia-Arman J, Munoz-Hernandez A, Garcia-Gomez JM, Diez-Martinez P, Grande-Barez M. Dual-energy x-ray absorptiometry in the diagnosis of osteoporosis: a practical guide. AJR Am J Roentgenol 2011;196: 897-904.

[8] Schulte FA, Lambers FM, Kuhn G, Muller R. In vivo micro-computed tomography allows direct three-dimensional quantification of both bone formation and bone resorption parameters using time-lapsed imaging. Bone 2011;48: 433-42.

[9] Galbán CJ, Chenevert TL, Meyer CR, Tsien C, Lawrence TS, Hamstra DA, Junck L, Sundgren PC, Johnson TD, Galbán S, Sebolt-Leopold JS, Rehemtulla A, Ross BD. Prospective analysis of parametric response map-derived MRI biomarkers: identification of early and distinct glioma response patterns not predicted by standard radiographic assessment. Clin Cancer Res 2011;17: 4751-60.

[10] Galbán CJ, Chenevert TL, Meyer CR, Tsien C, Lawrence TS, Hamstra DA, Junck L, Sundgren PC, Johnson TD, Ross DJ, Rehemtulla A, Ross BD. The parametric response map is an imaging biomarker for early cancer treatment outcome. Nat Med 2009;15: 572-6.

[11] Galban CJ, Mukherji SK, Chenevert TL, Meyer CR, Hamstra DA, Bland PH, Johnson TD, Moffat BA, Rehemtulla A, Eisbruch A, Ross BD. A feasibility study of parametric response map analysis of diffusion-weighted magnetic resonance imaging scans of head and neck cancer patients for providing early detection of therapeutic efficacy. Transl Oncol 2009;2: 184-90.

[12] Hamstra DA, Galban CJ, Meyer CR, Johnson TD, Sundgren PC, Tsien C, Lawrence TS, Junck L, Ross DJ, Rehemtulla A, Ross BD, Chenevert TL. Functional diffusion map as an early imaging biomarker for high-grade glioma: correlation with conventional radiologic response and overall survival. J Clin Oncol 2008;26: 3387-94.

[13] Lee KC, Bradley DA, Hussain M, Meyer CR, Chenevert TL, Jacobson JA, Johnson TD, Galban CJ, Rehemtulla A, Pienta KJ, Ross BD. A feasibility study evaluating the functional diffusion map as a predictive imaging biomarker for detection of treatment

response in a patient with metastatic prostate cancer to the bone. Neoplasia 2007;9: 1003-11.
[14] Lee KC, Sud S, Meyer CR, Moffat BA, Chenevert TL, Rehemtulla A, Pienta KJ, Ross BD. An imaging biomarker of early treatment response in prostate cancer that has metastasized to the bone. Cancer Res 2007;67: 3524-8.
[15] Moffat BA, Chenevert TL, Lawrence TS, Meyer CR, Johnson TD, Dong Q, Tsien C, Mukherji S, Quint DJ, Gebarski SS, Robertson PL, Junck LR, Rehemtulla A, Ross BD. Functional diffusion map: a noninvasive MRI biomarker for early stratification of clinical brain tumor response. Proc Natl Acad Sci U S A 2005;102: 5524-9.
[16] Moffat BA, Chenevert TL, Meyer CR, McKeever PE, Hall DE, Hoff BA, Johnson TD, Rehemtulla A, Ross BD. The functional diffusion map: an imaging biomarker for the early prediction of cancer treatment outcome. Neoplasia 2006;8: 259-67.
[17] Reischauer C, Froehlich JM, Koh DM, Graf N, Padevit C, John H, Binkert CA, Boesiger P, Gutzeit A. Bone metastases from prostate cancer: assessing treatment response by using diffusion-weighted imaging and functional diffusion maps--initial observations. Radiology 2010;257: 523-31.
[18] Tsien C, Galban CJ, Chenevert TL, Johnson TD, Hamstra DA, Sundgren PC, Junck L, Meyer CR, Rehemtulla A, Lawrence T, Ross BD. Parametric response map as an imaging biomarker to distinguish progression from pseudoprogression in high-grade glioma. J Clin Oncol 2010;28: 2293-9.
[19] Jee WS, Yao W. Overview: animal models of osteopenia and osteoporosis. J Musculoskelet Neuronal Interact 2001;1: 193-207.
[20] Turner RT, Wakley GK, Hannon KS. Differential effects of androgens on cortical bone histomorphometry in gonadectomized male and female rats. J Orthop Res 1990;8: 612-7.
[21] Olson ME, Bruce J. Ovariectomy, ovariohysterectomy and orchidectomy in rodents and rabbits. Can Vet J 1986;27: 523-7.
[22] Meyer CR, Boes JL, Kim B, Bland PH, Zasadny KR, Kison PV, Koral K, Frey KA, Wahl RL. Demonstration of accuracy and clinical versatility of mutual information for automatic multimodality image fusion using affine and thin-plate spline warped geometric deformations. Med Image Anal 1997;1: 195-206.
[23] Wronski TJ, Cintron M, Dann LM. Temporal relationship between bone loss and increased bone turnover in ovariectomized rats. Calcif Tissue Int 1988;43: 179-83.
[24] Cummings SR, Karpf DB, Harris F, Genant HK, Ensrud K, LaCroix AZ, Black DM. Improvement in spine bone density and reduction in risk of vertebral fractures during treatment with antiresorptive drugs. Am J Med 2002;112: 281-9.
[25] Griffith JF, Engelke K, Genant HK. Looking beyond bone mineral density : Imaging assessment of bone quality. Ann N Y Acad Sci 2010;1192: 45-56.
[26] Schuit SC, van der Klift M, Weel AE, de Laet CE, Burger H, Seeman E, Hofman A, Uitterlinden AG, van Leeuwen JP, Pols HA. Fracture incidence and association with bone mineral density in elderly men and women: the Rotterdam Study. Bone 2004;34: 195-202.
[27] Sornay-Rendu E, Munoz F, Duboeuf F, Delmas PD. Rate of forearm bone loss is associated with an increased risk of fracture independently of bone mass in postmenopausal women: the OFELY study. J Bone Miner Res 2005;20: 1929-35.
[28] Genant HK, Engelke K, Prevrhal S. Advanced CT bone imaging in osteoporosis. Rheumatology (Oxford) 2008;47 Suppl 4: iv9-16.

[29] Imai K. Vertebral fracture risk and alendronate effects on osteoporosis assessed by a computed tomography-based nonlinear finite element method. J Bone Miner Metab 2011;29: 645-51.
[30] Kalpakcioglu BB, Engelke K, Genant HK. Advanced imaging assessment of bone fragility in glucocorticoid-induced osteoporosis. Bone 2011;48: 1221-31.
[31] Keaveny TM. Biomechanical computed tomography-noninvasive bone strength analysis using clinical computed tomography scans. Ann N Y Acad Sci 2010;1192: 57-65.
[32] Brouwers JE, van Rietbergen B, Huiskes R. No effects of in vivo micro-CT radiation on structural parameters and bone marrow cells in proximal tibia of wistar rats detected after eight weekly scans. J Orthop Res 2007;25: 1325-32.
[33] Laperre K, Depypere M, van Gastel N, Torrekens S, Moermans K, Bogaerts R, Maes F, Carmeliet G. Development of micro-CT protocols for in vivo follow-up of mouse bone architecture without major radiation side effects. Bone 2011;49: 613-22.
[34] Brouwers JE, van Rietbergen B, Huiskes R, Ito K. Effects of PTH treatment on tibial bone of ovariectomized rats assessed by in vivo micro-CT. Osteoporos Int 2009;20: 1823-35.
[35] Johnson LC, Johnson RW, Munoz SA, Mundy GR, Peterson TE, Sterling JA. Longitudinal live animal micro-CT allows for quantitative analysis of tumor-induced bone destruction. Bone 2011;48: 141-51.
[36] Waarsing JH, Day JS, van der Linden JC, Ederveen AG, Spanjers C, De Clerck N, Sasov A, Verhaar JA, Weinans H. Detecting and tracking local changes in the tibiae of individual rats: a novel method to analyse longitudinal in vivo micro-CT data. Bone 2004;34: 163-9.
[37] Green JR, Guenther A. The backbone of progress--preclinical studies and innovations with zoledronic acid. Crit Rev Oncol Hematol 2011;77 Suppl 1: S3-S12.
[38] Watts NB, Geusens P, Barton IP, Felsenberg D. Relationship between changes in BMD and nonvertebral fracture incidence associated with risedronate: reduction in risk of nonvertebral fracture is not related to change in BMD. J Bone Miner Res 2005;20: 2097-104.
[39] Krug R, Burghardt AJ, Majumdar S, Link TM. High-resolution imaging techniques for the assessment of osteoporosis. Radiol Clin North Am 2010;48: 601-21.
[40] Coleman RE. Metastatic bone disease: clinical features, pathophysiology and treatment strategies. Cancer Treat Rev 2001;27: 165-76.
[41] Coleman RE, Rubens RD. The clinical course of bone metastases from breast cancer. Br J Cancer 1987;55: 61-6.
[42] Onishi T, Hayashi N, Theriault RL, Hortobagyi GN, Ueno NT. Future directions of bone-targeted therapy for metastatic breast cancer. Nat Rev Clin Oncol 2010;7: 641-51.
[43] Jemal A, Simard EP, Dorell C, Noone AM, Markowitz LE, Kohler B, Eheman C, Saraiya M, Bandi P, Saslow D, Cronin KA, Watson M, Schiffman M, Henley SJ, Schymura MJ, Anderson RN, Yankey D, Edwards BK. Annual Report to the Nation on the Status of Cancer, 1975-2009, featuring the burden and trends in human papillomavirus(HPV)-associated cancers and HPV vaccination coverage levels. J Natl Cancer Inst 2013;105: 175-201.
[44] Bubendorf L, Schopfer A, Wagner U, Sauter G, Moch H, Willi N, Gasser TC, Mihatsch MJ. Metastatic patterns of prostate cancer: an autopsy study of 1,589 patients. Hum Pathol 2000;31: 578-83.
[45] Guise TA. The vicious cycle of bone metastases. J Musculoskelet Neuronal Interact 2002;2: 570-2.

[46] Ellingson BM, Malkin MG, Rand SD, Connelly JM, Quinsey C, LaViolette PS, Bedekar DP, Schmainda KM. Validation of functional diffusion maps (fDMs) as a biomarker for human glioma cellularity. J Magn Reson Imaging 2010;31: 538-48.
[47] Hoff BA, Kozloff KM, Boes JL, Brisset JC, Galban S, Van Poznak CH, Jacobson JA, Johnson TD, Meyer CR, Rehemtulla A, Ross BD, Galban CJ. Parametric response mapping of CT images provides early detection of local bone loss in a rat model of osteoporosis. Bone 2012;51: 78-84.
[48] Craft N, Chhor C, Tran C, Belldegrun A, DeKernion J, Witte ON, Said J, Reiter RE, Sawyers CL. Evidence for clonal outgrowth of androgen-independent prostate cancer cells from androgen-dependent tumors through a two-step process. Cancer Res 1999;59: 5030-6.
[49] Klein KA, Reiter RE, Redula J, Moradi H, Zhu XL, Brothman AR, Lamb DJ, Marcelli M, Belldegrun A, Witte ON, Sawyers CL. Progression of metastatic human prostate cancer to androgen independence in immunodeficient SCID mice. Nat Med 1997;3: 402-8.
[50] Nickerson T, Chang F, Lorimer D, Smeekens SP, Sawyers CL, Pollak M. In vivo progression of LAPC-9 and LNCaP prostate cancer models to androgen independence is associated with increased expression of insulin-like growth factor I (IGF-I) and IGF-I receptor (IGF-IR). Cancer Res 2001;61: 6276-80.
[51] Moffat BA, Hall DE, Stojanovska J, McConville PJ, Moody JB, Chenevert TL, Rehemtulla A, Ross BD. Diffusion imaging for evaluation of tumor therapies in preclinical animal models. MAGMA 2004;17: 249-59.

Chapter 5: **Conclusions**

Accuracy in the diagnostic interpretation of radiological images is dependent upon many variables and resulting image quality. Conventional image characteristics such as voxel size and gray scale bit depth are important factors, but significant improvements in diagnosis will likely rely on post-processing methods aimed toward facilitating the delineation of radiological findings, improving both the confidence and accuracy of the interpreter. The overarching goal of this research effort was to advance the development of non-invasive imaging biomarkers through appropriate and optimized techniques. This research effort explored the improvement of quantitative readout sensitivity for assessment of treatment efficacy through complementary multimodal imaging platforms. While region-specific histogram analysis was used, this research effort also explored the value of voxel-by-voxel analysis of changes in imaging readouts over time as a more sensitive and accurate approach for delineation of disease-related and treatment-associated changes in the tissue of interest. Thus the proper selection of image modalities and post-processing techniques is most likely to significantly advance radiological practice and improve overall patient care.

In my search for novel imaging biomarkers of therapeutic efficacy, I investigated the value in DW-MRI acquisition of extended b-values and non-linear parametric models for improved sensitivity and interpretation. For assessment of cancer chemotherapeutic response in this study, high b-value diffusion models did in fact provide a better fit to the attenuation curve observed in living tissue. However, my results also showed that these higher-order models did not necessarily provide additional information, and in fact were much less stable and required significantly greater imaging and post-processing time. The main, or "fast", diffusion parameters all had similar sensitivity to response, but the standard mono-exponential model was found to be much less sensitive to noise. Thus, after careful evaluation of the possible acquisition variables involved with the generation of DW-MR images, it was found that due to the simplicity of its

analytical calculation and faster acquisition time, use of a limited number of lower b-values are overall more appropriate for routine clinical use.

An additional aspect of my research effort was to investigate the use of combined imaging metrics from multi-modal readouts. In this regard, assessment of targeted anti-vascular response was undertaken utilizing DW- along with DCE-MRI. My results revealed the role of each modality and their relative contributions in predicting cancer response to this class of agents. Although there was a clear and strong response in vascular-sensitive imaging readouts (DCE-MRI), there was no increase in tumor ADC values which would be expected if a drop in tumor cellularity occurred. In fact, I observed a significant drop in ADC which was attributed to a decrease in tumor edema, secondary to the drug-induced decrease in neovascular leakiness. Thus the use of multi-modal approaches for assessment of anti-vascular treatment effects was shown to more fully characterize the responses of the tumor in which transient growth control occurred but without appreciable mortality of tumor cells.

Imaging not only allows observations to be made on the tumor itself, but also on the host tissue which is important, as tumor-host interactions are well known to occur in cancer biology. The interactions between metastatic lesions and their micro-environment are a complex phenomenon which can progress to tumor propagation and infiltration into the local stroma. Current therapy research is aimed at disrupting this interaction, resulting in re-normalization of the microenvironment as well as tumor cell kill. In this context, a multi-modality imaging approach was explored for characterization of tumor-stromal response to standard therapies in a mouse model of boney metastasis. Image analysis allowed for exploration of the overall balance and dynamics between osteolytic and osteoblastic activity during tumor growth and therapeutic interventions. It was found that the complementary use of clinically-applicable and pre-clinical optical imaging readouts was able to provide a more comprehensive understanding of tumor-local response to both bone-protective and tumor-targeted therapies. These findings present opportunities for improvement in clinical evaluation of therapeutic response as well as our understanding of the interconnected signaling pathways associated with tumor-stromal interactions using non-invasive imaging.

Additionally, the development of improved image post-processing algorithms was undertaken through evaluation of a novel voxel-based analytical method termed the parametric response map (PRM). When applied to CT imaging, this method was shown to be sensitive in the

detection and quantification of spatially-varying alterations in mineral density using preclinical models of osteoporosis and bone metastasis. More detailed studies were also undertaken to evaluate the capabilities of this imaging approach for distinguishing osteolytic from osteoblastic phenotypes of bone metastasis in an effort to identify unique biomarker signatures for each. These studies demonstrated that PRM provided the capability for non-invasive detection of important tumor characteristics as well local bone response to interventions designed to reduce the process of bone erosion. These research findings are an important contribution toward providing new image-based diagnostic capabilities which can provide additional information to assist with clinical decision-making for patients with high risk of incurring skeletal related events.

In conclusion, there is a strong need for optimization of imaging protocols in order to provide for improved diagnostic medicine as well as treatment response sensitivity. This research effort identified several key areas for optimizing radiological contributions towards improved patient management:

- Optimized acquisition of images
- Improvements in image post-processing
- Multimodal image combinations to enhance diagnosis
- Voxel-by-voxel, PRM-based analysis of images

Overall, quantitative imaging is linked to physiological mechanisms through simplified mathematical models. Care must be taken in model selection to ensure accuracy and robustness of quantitative readouts as well as sensitivity to a physiological change. Also, multi-modal imaging is critical for forming a comprehensive understanding of tumor treatment response that can be used to inform pharmaceutical development as well as clinical care. Cancer is a highly complex disease, changing its micro-environment in order to thrive. Assessment of tumor and stromal treatment effects is critical for improved understanding of the underlying biological processes involved, which are needed to make progress in the treatment of this disease. The work presented here signifies a push toward the development and clinical implementation of new non-invasive biomarkers for assessment of cancer therapeutic efficacy.

Appendix A: Calculation of Local Model Sensitivity

Model sensitivity to individual input parameters was calculated as the partial derivative of the signal-intensity equation with respect to each parameter. Sensitivity was assessed at static values of all input parameters and a fixed range of b-values or times (for diffusion or permeability models, respectively). Analytical derivative solutions are shown below:

Diffusion:

Mono-Exponential

- $\frac{\delta S}{\delta ADC} = -S_0 b e^{-b \cdot ADC} \rightarrow SC = -bADC$

Stretched-Exponential

- $\frac{\delta S}{\delta DDC} = -S_0 \alpha e^{-(b \cdot DDC)^\alpha} \cdot \left(\frac{(b \cdot DDC)^\alpha}{DDC}\right) \rightarrow SC = -\alpha \cdot (b \cdot DDC)^\alpha$
- $\frac{\delta S}{\delta \alpha} = -S_0 (b \cdot DDC)^\alpha e^{-(b \cdot DDC)^\alpha} \cdot ln(b \cdot DDC) \rightarrow SC = -\alpha \cdot ln(b \cdot DDC) \cdot (b \cdot DDC)^\alpha$

Bi-Exponential

- $\frac{\delta S}{\delta D_f} = -S_0 b (1 - f_s) e^{-b \cdot D_f} \rightarrow SC = \frac{-b}{1 + \frac{f_s}{(1-f_s)} e^{-b\left(D_s - D_f\right)}}$
- $\frac{\delta S}{\delta D_s} = -S_0 b f_s e^{-b \cdot D_s} \rightarrow SC = \frac{-b}{1 + \frac{(1-f_s)}{f_s} e^{-b\left(D_f - D_s\right)}}$
- $\frac{\delta S}{\delta f_s} = S_0 \left(e^{-b \cdot D_s} - e^{-b \cdot D_f}\right) \rightarrow SC = \frac{1 - e^{-b\left(D_f - D_s\right)}}{1 + \frac{(1-f_s)}{f_s} e^{-b\left(D_f - D_s\right)}}$

Permeability:

i. * denotes the convolution operator

ii. Using the chain rule, $\frac{\delta S}{\delta x_i} = \frac{\delta S}{\delta R_1} \cdot \frac{\delta R_1}{\delta C_t} \cdot \frac{\delta C_t}{\delta x_i}$

iii. $R_1 = R_{10} + r_1 C_t \quad \underset{D}{\Leftrightarrow} \quad \frac{\delta R_1}{\delta C_t} = r_1$

iv. Gradient-echo signal intensity:

$$S = S_0 \frac{\sin\alpha \cdot \left(1 - e^{-TR \cdot R_1}\right)}{1 - \cos\alpha \cdot e^{-TR \cdot R_1}} \quad \underset{D}{\Leftrightarrow} \quad \frac{\delta S}{\delta R_1} = \frac{S_0 \cdot TR \cdot \sin\alpha \cdot e^{-TR \cdot R_1} (1 - \cos\alpha)}{\left(1 - \cos\alpha \cdot e^{-TR \cdot R_1}\right)^2}$$

Tofts-Kermode

- $\frac{\delta C}{\delta K^{Trans}} = \left(C_p * e^{-K^{Trans}t/v_e}\right)\left(1 - \frac{K^{Trans}t}{v_e}\right)$
- $\frac{\delta C}{\delta v_e} = t\left(\frac{K^{Trans}}{v_e}\right)^2\left(C_p * e^{-K^{Trans}t/v_e}\right)$

Efflux-Corrected (Patlak)

- $\frac{\delta C}{\delta K^{Trans}} = \left(C_p * e^{-K^{Trans}t/v_e}\right)\left(1 - \frac{K^{Trans}t}{v_e}\right)$
- $\frac{\delta C}{\delta v_e} = t\left(\frac{K^{Trans}}{v_e}\right)^2\left(C_p * e^{-K^{Trans}t/v_e}\right)$
- $\frac{\delta C}{\delta v_p} = C_p$

Shutter-Speed

i. $S = S_{ss}\frac{\left(1-\cos\alpha\cdot e^{-TR\cdot R_{ss}}\right)}{\left(1-e^{-TR\cdot R_{ss}}\right)}\cdot\frac{\left(1-e^{-TR\cdot R_1}\right)}{\left(1-\cos\alpha\cdot e^{-TR\cdot R_1}\right)}$

ii. $S' = S_{ss}\left[\frac{a'(R_{ss})\cdot b(R_{ss}) - b'(R_{ss})\cdot a(R_{ss})}{b(R_{ss})^2}\cdot\frac{b(R_1)}{a(R_1)}R'_{ss} + \frac{b'(R_1)\cdot a(R_1) - a'(R_1)\cdot b(R_1)}{a(R_1)^2}\cdot\frac{a(R_{ss})}{b(R_{ss})}R'_1\right]$

a. Apostrophe, ‘, indicates the derivative of the function
b. $a(x) = 1 - \cos\alpha\cdot e^{-TR\cdot x} \rightarrow a'(x) = TR\cdot\cos\alpha\cdot e^{-TR\cdot x}$
c. $b(x) = 1 - e^{-TR\cdot x} \rightarrow b'(x) = TR\cdot e^{-TR\cdot x}$
d. $R_{ss} = R_1(0)$
e. $S_{ss} = S(0)$

iii. $\gamma = \frac{R_{10} - R_{1i} + {}^1/_{\tau_i}}{p_0}$

iv. $C_0 = L\left(C_p * e^{-Lt}\right)$

- $\frac{\delta R_1}{\delta L} = \frac{r_1 C_0(1-Lt)}{2L}\left[1 - \frac{\frac{2}{\tau} - r_1C_0 - \gamma}{\sqrt{\left(\frac{2}{\tau_i} - r_1C_0 - \gamma\right)^2 + \frac{4(1-p_0)}{{\tau_i}^2 p_0}}}\right]$
- $\frac{\delta R_1}{\delta p_0} = \frac{1}{2p_0}\left[\frac{\frac{2}{{\tau_i}^2 p_0} - \gamma\left(\frac{2}{\tau_i} - r_1C_0 - \gamma\right)}{\sqrt{\left(\frac{2}{\tau_i} - r_1C_0 - \gamma\right)^2 + \frac{4(1-p_0)}{{\tau_i}^2 p_0}}} - \gamma\right]$
- $\frac{\delta R_1}{\delta \tau} = \frac{1}{2{\tau_i}^2}\left[\frac{\left(\frac{2}{\tau_i} - r_1C_0 - \gamma\right)\left(2 - \frac{1}{p_0}\right) - \frac{8(1-p_0)}{\tau_i \cdot p_0}}{\sqrt{\left(\frac{2}{\tau_i} - r_1C_0 - \gamma\right)^2 + \frac{4(1-p_0)}{{\tau_i}^2 p_0}}} - \frac{1}{p_0}\right]$